

**NANOSHELL PLATFORMS FOR TARGETED GENE REGULATION
AND LIGHT-TRIGGERED CANCER THERAPY**

by

Rachel S. Riley

A dissertation submitted to the Faculty of the University of Delaware in partial
fulfillment of the requirements for the degree of Doctor of Philosophy
in Biomedical Engineering

Summer 2018

© 2018 Rachel S. Riley
All Rights Reserved

**NANOSHELL PLATFORMS FOR TARGETED GENE REGULATION
AND LIGHT-TRIGGERED CANCER THERAPY**

by

Rachel S. Riley

Approved: _____
Dawn Elliott, Ph.D,
Chair of the Department of Biomedical Engineering

Approved: _____
Babatunde A. Ogunnaike, Ph.D.
Dean of the College of Engineering

Approved: _____
Ann L. Ardis, Ph.D.
Senior Vice Provost for Graduate and Professional Education

I certify that I have read this dissertation and that in my opinion it meets the academic and professional standard required by the University as a dissertation for the degree of Doctor of Philosophy.

Signed:

Emily S. Day, Ph.D.
Professor in charge of dissertation

I certify that I have read this dissertation and that in my opinion it meets the academic and professional standard required by the University as a dissertation for the degree of Doctor of Philosophy.

Signed:

Jason Gleghorn, Ph.D.
Member of dissertation committee

I certify that I have read this dissertation and that in my opinion it meets the academic and professional standard required by the University as a dissertation for the degree of Doctor of Philosophy.

Signed:

Millicent Sullivan, Ph.D.
Member of dissertation committee

I certify that I have read this dissertation and that in my opinion it meets the academic and professional standard required by the University as a dissertation for the degree of Doctor of Philosophy.

Signed:

Kenneth Van Golen, Ph.D.
Member of dissertation committee

ACKNOWLEDGMENTS

First, I would like to thank my advisor, Dr. Emily Day, for her continued support, scientific guidance, and mentorship over the past 5 years. Thank you for pushing me over the years to become a knowledgeable cancer nanotechnologist today. You are an incredible mentor, and I fully appreciate both your scientific and personal guidance over the past 5 years. Further thanks to my committee members, Dr. Jason Gleghorn, Dr. Millicent Sullivan, and Dr. Kenneth Van Golen, for several helpful discussions and suggestions throughout my PhD studies.

Thank you to the entire Day lab for making my PhD experience so enjoyable and productive. This lab began as just two of us, and it has been rewarding to watch it grow over the years: Jilian Melamed, Danielle Valcourt, Jenna Harris, Megan Dang, Benjamin Luo, Chintan Kapadia, Jianxin Wang, and Ritu Goyal. Special thanks to the remarkable undergraduate students who have worked with me and taught me how to grow as a mentor, especially Maggie Billingsley and Rachel O'Sullivan. I would also like to thank Andrea Potocny for her extensive chemistry knowledge and for the opportunity to collaborate during graduate school. It has truly been a great experience working with all of you.

I would like to acknowledge several individuals for help with equipment and experimental advice during my PhD. First, thank you to the Bioimaging Center at the Delaware Biotechnology Institute, and to Michael Moore in particular, for sharing with me your extensive experience and knowledge about microscopy. I am also grateful to Dr. Gwen Talham, Travis Cossette, and the rest of the critical staff at the

animal facility for your invaluable advice and assistance over the past few years.

Thank you to Dr. Christopher Price and Michael David for protocols and advice for *in vivo* experiments and the subsequent histology.

Next, I would like to thank my family and friends for your endless support throughout this journey. To my dear husband David – thank you for being patient, helpful, and so supportive during my PhD. Thank you also to my parents for the endless encouragement and for always wanting to know about my research. Thank you to Alyssa, Danielle, and Sofia for always keeping me grounded and for being my best friends. Lastly, thank you to our dear friends Keely and Philipp Keller, who have travelled this journey with us from the beginning. Thank you for all of the laughter, scientific and non-scientific discussions, and your terrific company over the years. Please know how much I have appreciated you all during my PhD and will continue to do so in the years to come.

Finally, I am truly thankful to the American Association of University Women for providing me the opportunity and funding to be an American Dissertation Fellow and to be a part of a truly remarkable organization. It is, and will continue to be, a passion of mine to advance the inclusion of women in science and engineering.

Dedication

This dissertation is dedicated to my husband, David, and to my family.

Without your support, this would not have been possible.

TABLE OF CONTENTS

LIST OF TABLES.....	xii
LIST OF FIGURES	xiii
ABSTRACT.....	xvi

Chapter

1	INTRODUCTION TO NANOPARTICLE-BASED CANCER THERAPY	1
1.1	A Brief Introduction to the Hallmarks of Cancer	2
1.1.1	Current Clinical Strategies to Treat Cancer	5
1.1.2	Need for Novel Therapies for Triple-Negative Breast Cancer	7
1.1.3	Wnt Signaling as a Target for TNBC	9
1.2	An Introduction to Cancer Nanomedicine	10
1.2.1	Passive and Active Targeting of Nanoparticles	11
1.2.2	Current Clinical Status of Nanoparticle-Based Cancer Therapies.....	12
1.3	Gold-Based Nanoparticles in Oncology Research.....	14
1.3.1	Photoresponsive Nanoparticles for High Precision Cancer Therapy	15
1.3.2	Gold Nanoparticle Carriers for Gene Regulation <i>via</i> RNA interference	19
1.3.3	Antibody-Gold Nanoparticle Conjugates for Signal Cascade Interference	21
1.4	An Introduction to Silica Core/Gold Shell Nanoshells.....	22
1.4.1	Engineering the Size and Structure of Nanoshells for Cancer Imaging and Therapy	23
1.4.2	Opportunities for Nanoshells in Cancer Therapy	24
2	MATERIALS AND METHODS FOR NANOSHELL SYNTHESIS, FUNCTIONALIZATION, AND CHARACTERIZATION.....	26

2.1	Synthesis of Silica Core/Gold Shell Nanoshells	26
2.2	Nanoshell Functionalization with methoxy-poly(ethylene) glycol (mPEG), Antibodies, and siRNA.....	28
2.2.1	Methoxy poly(ethylene) glycol (mPEG-SH) Attachment to Nanoshells.....	28
2.2.2	Antibody Conjugation to Nanoshells.....	28
2.2.3	Conjugation of siRNA to Nanoshells	29
2.3	Characterization Methods	30
2.3.1	Scanning Electron Microscopy (SEM)	31
2.3.2	Ultraviolet-Visible Spectrophotometry (UV-vis), Dynamic light scattering (DLS), and Zeta Potential Measurements	31
2.3.3	Quantification of Surface-Conjugated Antibodies.....	32
2.3.4	Quantification of Surface-Conjugated siRNA	32
3	DUAL PHOTOTHERMAL AND PHOTODYNAMIC THERAPY AS A COMBINATORIAL STRATEGY TO TREAT TRIPLE-NEGATIVE BREAST CANCER.....	34
3.1	Introduction to Chapter 3	34
3.1.1	Photodynamic Therapy by a Novel Photosensitizer	35
3.1.2	Nanoshell-Mediated Photothermal Therapy and the Importance of Inducing Apoptosis as the Mechanism of Cell Death.....	37
3.1.3	Combining Photothermal and Photodynamic Therapies for Multimodal Cancer Treatment.....	39
3.2	Materials and Methods.....	41
3.2.1	Nanoshell Functionalization and Characterization	41
3.2.2	Synthesis and Characterization of PS	42
3.2.3	Photodegradation of Pd[DMBil1]-PEG ₇₅₀	43
3.2.4	Singlet Oxygen Production from Pd[DMBil]-PEG ₇₅₀	43
3.2.5	Temperature and ¹ O ₂ Production During PDT and PTT.....	45
3.2.6	Cell Culture.....	45
3.2.7	Cellular Uptake of Pd[DMBil1]-PEG ₇₅₀ and Nanoshells	46
3.2.8	Analysis of the Mechanisms of Cell Death Induced by PTT and/or PDT.....	47
3.2.9	Assessment of Cells' Metabolic Activity Following PDT and/or PTT	47

3.3	Results.....	49
3.3.1	Characterization and Singlet Oxygen Production of Pd[DMBil1]-PEG ₇₅₀	49
3.3.2	PEG-NS and Pd[DMBil1]-PEG ₇₅₀ are Stable in Cell Culture Media	50
3.3.3	PEG-NS and Pd[DMBil1]-PEG ₇₅₀ Produce Heat and ¹ O ₂ when Combined.....	51
3.3.4	Pd[DMBil1]-PEG ₇₅₀ and PEG-NS are Taken Up by TNBC Cells	53
3.3.5	Pd[DMBil1]-PEG ₇₅₀ is Minimally Toxic to TNBC Cells in the Dark.....	54
3.3.6	The Phototoxicity Index of Pd[DMBil1]-PEG ₇₅₀ is Substantially Higher than Commercial Photosensitizers	55
3.3.7	PDT Triggers Primarily Apoptotic Cell Death	58
3.3.8	Dual PDT/PTT is a Potent Strategy to Treat TNBC.....	60
3.4	Discussion.....	62
3.5	Conclusions.....	64
3.6	Future Work.....	65
4	AN EVALUATION OF THE MECHANISMS OF LIGHT-TRIGGERED SIRNA RELEASE FROM NANOSHELLS FOR ON-DEMAND GENE REGULATION.....	67
4.1	Introduction to Chapter 4.....	67
4.1.1	Small Interfering RNA (siRNA) As A Tool for Gene Regulation.....	68
4.1.2	Nanoparticle Platforms for On-Demand Gene Regulation for Cancer Therapy	69
4.1.3	Continuous Wave versus Pulsed Laser Irradiation for Triggering Release of Molecules from Nanoparticles	71
4.2	Materials and Methods.....	73
4.2.1	Characterization of Temperature and siRNA Release Upon Laser Irradiation.....	74
4.2.2	U373.eGFP Cell Culture.....	75
4.2.3	Transfection with Released GFP siRNA	75
4.2.4	Light-Triggered GFP Silencing in U373.eGFP Cells with siRNA-NS	77
4.3	Results.....	78

4.3.1	Continuous Wave Laser Irradiation Causes Substantial Temperature Increases Compared to Pulsed Irradiation	78
4.4	NS Irradiated with Continuous Wave Light Experience Structural Changes.....	79
4.4.1	Pulsed Laser Irradiation Triggers the Release of siRNA from NS with Higher Efficiency than CW Laser Irradiation	82
4.4.2	Pulsed Irradiation Primarily Releases More siRNA Duplexes than CW Irradiation	84
4.4.3	Released siRNA Retains its Gene Silencing Functionality	86
4.4.4	siRNA-NS Conjugates Enter Cells to Mediate On-Demand Gene Regulation.....	86
4.5	Discussion.....	88
4.6	Future Work.....	91
4.7	Conclusions.....	92
5	MOLECULARLY-TARGETED NANOSHELLS FOR MULTIVALENT BINDING AND WNT SIGNALING INHIBITION IN TRIPLE-NEGATIVE BREAST CANCER.....	93
5.1	Introduction to Chapter 5	93
5.1.1	Antibodies as Therapeutic Agents for Cancer Management	94
5.1.2	Wnt Signaling Drives TNBC Progression and Lung Metastasis	95
5.1.3	Antibody-Nanoparticle Conjugates for Active Tumor Targeting.....	97
5.1.4	Nanoparticle Multivalency Enhances Binding Avidity and Signal Cascade Interference.....	99
5.2	Materials and Methods.....	99
5.2.1	Cell Culture.....	100
5.2.2	Immunohistochemical Staining of FZD7.....	100
5.2.3	Specific Binding of FZD7-NS to TNBC Cells	101
5.2.4	Binding Avidity of FZD7-NS and Free FZD7 Antibodies	101
5.2.5	Immunofluorescence Staining for β -catenin Expression	102
5.2.6	Western Blot Analysis for β -catenin or Frizzled7 Expression ..	103
5.2.7	qRT-PCR Analysis for Axin2 mRNA Expression.....	104
5.2.8	Analysis of Cellular Metabolic Activity	105
5.2.9	Formation of TNBC Lung Metastases and Nanoparticle Injections in Mice	106
5.2.10	Hematoxylin and Eosin (H&E) Staining	106

5.2.11	Inductively Coupled Plasma-Mass Spectrometry (ICP-MS) for Analysis of Gold Content in Tissues	107
5.3	Results.....	108
5.3.1	Nanoshell Characterization.....	108
5.3.2	TNBC Cells Overexpress FZD7 Receptors	109
5.3.3	FZD7-NS Bind TNBC Cells with Higher Avidity than Free FZD7 Antibodies	110
5.3.4	FZD7-NS Suppress Wnt Signaling in TNBC Cells More Effectively than Free FZD7 Antibodies.....	112
5.3.5	FZD7-NS Suppress Metabolic Activity of TNBC Cells.....	116
5.3.6	A Pilot Study Indicates that FZD7-NS can Enter TNBC Lung Metastases to Slow Tumor Growth.....	117
5.3.7	H&E Staining of Lung Sections and Biodistribution of FZD7-NS	118
5.4	Discussion.....	120
5.5	Future Work.....	124
5.6	Conclusions.....	126
6	CONCLUSIONS	128
6.1	Nanoshells as Comprehensive Platforms for Cancer Therapy	128
6.2	Opportunities and Challenges for Gold Nanoparticles for Cancer Therapy	131
6.3	Concluding Remarks.....	132
	REFERENCES	134
Appendix		
	A - IACUC APPROVAL.....	150
	B - PERMISSIONS TO USE SELF-AUTHORED PAPERS	151

LIST OF TABLES

Table 4.1: siGFP, siSCR, and Cy5 siSCR siRNA sequences used in this work.....	73
---	----

LIST OF FIGURES

Figure 1.1: The main characteristics and hallmarks of cancer that are acquired by cells and their microenvironment	3
Figure 1.2: Risk of disease recurrence in distant organs	8
Figure 1.3: Functionalities of gold NPs	10
Figure 1.4: Passive and active targeting of NPs.	12
Figure 1.5: Number of targeted NP publications.....	14
Figure 1.6: The steps of photothermal therapy	15
Figure 1.7: Types of gold NPs for phototherapy	17
Figure 1.8: Light absorbance by tissue.	31
Figure 1.9: Mechanism of RNA interference using siRNA.....	20
Figure 1.10: Multivalent binding of antibody-NP conjugates	22
Figure 1.11: Absorbance properties of NSs.....	24
Figure 1.12: NS conjugates used in this dissertation	25
Figure 2.1 NS synthesis	27
Figure 2.2: Schematic of antibody conjugation to NSs	29
Figure 2.3: Schematic showing siRNA conjugation to NSs.....	30
Figure 3.1: Schematics of photodynamic therapy.....	37
Figure 3.2: Schematic of PEG-NS and the mechanisms of cell death.....	39
Figure 3.3: Dual photodynamic/photothermal therapy.....	40
Figure 3.4: Absorbance spectrum of the photosensitizers	50

Figure 3.5: Characterization of solutions of PEG-NS and photosensitizer	51
Figure 3.6: Temperature and singlet oxygen measurements	52
Figure 3.7: Cell uptake of PEG-NS and photosensitizer	54
Figure 3.8: Photosensitizer toxicity	55
Figure 3.9: Cell viability following PDT	57
Figure 3.10: Cell viability following PDT with commercial photosensitizers	71
Figure 3.11: Mechanism of cell death from PDT	59
Figure 3.12: Cell viability following dual PDT/PTT	61
Figure 3.13: Mechanism of cell death following PDT/PTT	62
Figure 4.1: Schematic showing the process of on-demand gene regulation with siRNA-NS conjugates.....	72
Figure 4.2: Schematic of Cy5-siSCR-NS	73
Figure 4.3: Laser irradiation setup	79
Figure 4.4: Bulk solution temperature measurements	79
Figure 4.5: NS characterization after laser treatment	81
Figure 4.6: Flow cytometry analysis of NS structure	82
Figure 4.7: Percent siRNA release following irradiation.....	83
Figure 4.8: Gel electrophoresis of siRNA released from NSs	85
Figure 4.9: GFP knockdown in transfected cells	87
Figure 4.10: Cell uptake of Cy5-siSCR-NS.....	87
Figure 4.11: Analysis of GFP silencing upon pulsed laser irradiation	89
Figure 5.1: Schematic of the Wnt signaling pathway	96
Figure 5.2: Wnt signaling inhibition by FZD7-NS.....	98
Figure 5.3: Characterization of FZD7-NS	109

Figure 5.4: FZD7 expression in TNBC cells	110
Figure 5.5: Two-photon microscopy showing binding capacity of FZD7-NS	111
Figure 5.6: Effective dissociation constant of FZD7-NS.....	112
Figure 5.7: FZD7-NS mediated inhibition of β -catenin	114
Figure 5.8: Axin2 expression following treatment	116
Figure 5.9: Cell viability analysis	117
Figure 5.10: Timeline of the pilot in vivo study	119
Figure 5.11: Analysis of tumor growth.....	119
Figure 5.12: Lung tumors in murine model of metastatic TNBC.....	120
Figure 5.13: NS biodistribution in lung tumors.....	121

ABSTRACT

Nanoparticles (NPs) are promising tools to improve upon conventional cancer treatment strategies that are limited by significant off-target effects and unsatisfactory patient outcomes. In this dissertation, we demonstrate that NPs called nanoshells (NSs) comprised of silica cores and thin gold shells are versatile platforms to mediate phototherapy and/or or gene regulation of cancer by exploiting their unique optical and bioconjugation properties. For phototherapies, NSs either generate heat to damage the surrounding cancer cells, or they can be triggered to release any surface-bound molecules using continuous wave or pulsed laser irradiation, respectively. In gene regulation applications, the gold NS surfaces are decorated with therapeutic antibodies or small interfering RNA (siRNA) molecules using gold-thiol chemistry. By exploiting these unique features, our overarching goal was to establish NSs as multifunctional and versatile tools that offer high precision cancer therapy.

Our first objective in this thesis was to evaluate a combinatorial phototherapy approach using both PTT and photodynamic therapy (PDT) to induce irreversible cancer cell death. PTT damages cancer cells by activating NSs embedded in tumors to produce heat in response to near infrared light, while PDT uses photosensitizers that are activated by lower wavelengths of light to produce toxic singlet oxygen. We hypothesized that dual therapy would be more effective for tumor ablation than either therapy alone by overcoming the limitations of each option. In Chapter 3, we evaluate a novel and potent photosensitizer to mediate PDT, and we show that dual PTT/PDT mediated by NSs and this photosensitizer, respectively, work synergistically to induce

apoptotic cell death more efficiently than each strategy alone.

Our second objective was to demonstrate that NSs can enable high precision gene regulation through light-triggered release of siRNA. The use of NPs for siRNA delivery is promising to overcome the instability and poor cellular uptake of free siRNA. However, to avoid widespread gene regulation, it is ideal that siRNA-NP conjugates release their cargo on-demand only in tumor cells. We hypothesized that siRNA-NS conjugates would remain inactive until the siRNA was released from NSs upon excitation with pulsed laser light. In Chapter 4, we show that pulsed laser excitation releases duplexes of siRNA, and we provide a mechanistic understanding of how these plasmonic NPs operate to enable on-demand gene regulation.

The third goal was to establish antibody-NS conjugates as platforms for oncogenic cell signaling interference. We hypothesized that antibody-NS conjugates could actively target cancer cells to hinder oncogenic signaling more effectively than freely delivered antibodies due to their higher binding affinities. We found that antibody-NS conjugates bind cancer cells with more strength than free antibodies, resulting in improved signal cascade interference. Further, these conjugates retain their targeting abilities *in vivo*, as antibody-NS conjugates accumulate in small lung metastases in a murine model of metastatic breast cancer, which slows tumor growth. These results indicate that antibody-NS conjugates may permit lower antibody dosages to be administered for cancer management.

In total, this dissertation evaluates how the unique properties of NSs can be exploited to enable high precision cancer therapy by three powerful but distinct treatment mechanisms. Due to their high specificity and potency, these multifunctional NPs are promising alternatives to current cancer therapies.

Chapter 1

INTRODUCTION TO NANOPARTICLE-BASED CANCER THERAPY

The overarching goal of this dissertation was to develop and study novel nanoparticle-based platforms for cancer therapy. Throughout this dissertation, we used nanoshells (NSs) composed of silica cores and thin gold shells as the core material due to their unique light properties and simple bioconjugation chemistry that makes them ideal for light-based therapies and gene regulation, respectively. A main theme throughout this work is to prove how nanoparticles can improve upon therapeutics for cancer treatment and to reduce adverse effects to healthy tissues compared to the same therapies delivered without their nanoparticle carriers. Thus, each Chapter represents a novel way in which NSs can be exploited for phototherapies, on-demand gene regulation, and active targeting for signal cascade interference of diseased cells and tissues. In Chapter 1, we introduce concepts that provide the basis for the later chapters, and we discuss common themes that will be presented throughout this dissertation. Sections in this Chapter have been adapted from my co-authored articles:

- (1) Riley RS, Day ES. Gold Nanoparticle-Mediated Photothermal Therapy: Applications and Opportunities for Multimodal Cancer Treatment. *WIREs Nanomed Nanobiotechnol* 2016, e1449.
- (2) Valcourt DM, Harris J, Riley RS, Dang M, Wang J, Day ES. Advances in Targeted Nanotherapeutics: From Bioconjugation to Biomimicry. *Nano Research* 2018, 3, 1-18.

1.1 A Brief Introduction to the Hallmarks of Cancer

Although cancer research has experienced tremendous advances over the past few decades, the disease remains a significant challenge today. A main difficulty that limits the success of cancer treatments is that most cancers are highly heterogeneous. Therefore, it is critical to understand the underpinnings of cancer biology and the formation of tumors to ultimately design new therapeutic strategies to treat this disease. Towards this goal, Hanahan and Weinberg proposed the hallmarks and enabling characteristics of cancer cells and their microenvironment that are required for disease development (Figure 1.1).¹ These hallmarks and characteristics encompass the necessary capabilities that cells acquire in order to become malignant, and most treatment options for cancer target one or more of these features. The therapeutics developed in this dissertation aim to disrupt several of these hallmarks of cancer including genomic instability, resisted cell death, sustained proliferative signaling, and activated invasion and metastasis. Below, we briefly explain the implications of these specific hallmarks towards cancer progression and we discuss their importance to the scope of this dissertation.

A broad and overarching feature of cancer progression is genomic instability and mutations. As cells become cancerous, they acquire mutations to their genomes that in turn cause several of the other hallmark capabilities.¹ In cancer, these mutations are often associated with chromosomal instability and rearrangements that lead to changes in gene expression, aberrant oncogenic cell signaling, and ultimately increased tumorigenesis.² One oncogenic cell signaling pathway that is implicated in genomic instability and cancer progression is the Wnt signaling pathway. Aberrant

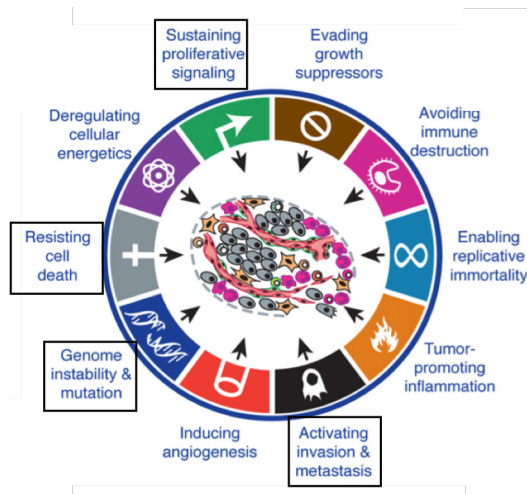


Figure 1.1: The main characteristics and hallmarks of cancer that are acquired by cells and their microenvironment. The boxed hallmarks are directly investigated in this dissertation. Image adapted from *Hanahan and Weinberg, Cell, 2011*.

Wnt signaling is linked to many types of cancer including breast cancer, colon cancer, and lung cancer, and it causes chromosomal instability due to mutations in several Wnt genes.²⁻⁴ Such genomic instability is critical to Chapters 4 and 5 in this dissertation. On a broad scale, Chapter 4 presents a novel means of downregulating aberrant cell signaling that is applicable to a wide range of target genes, and Chapter 5 directly investigates how controlling Wnt signaling influences cancer progression. Interestingly, genomic instability is a key feature responsible for other hallmarks of cancer as described below.¹

Two more hallmarks of cancer that work cohesively are cell's abilities to resist cell death and to sustain proliferation.¹ The ability for cancer cells to resist cell death is critical to prolonged survival and growth. Normally, cells undergo programmed cell death in response to physiological or intracellular signals.⁵ Alternatively, tumor cells adapt to avoid or ignore these apoptotic signals due to overactive cell signaling and

loss of tumor suppressor functions, among others.⁶ Chapter 3 in this dissertation studies how phototherapies can induce apoptosis in cancer cells to overcome this hallmark. The ability of cells to avoid apoptosis is exacerbated by uncontrollable proliferation leading to rapid tumor formation.⁷ The proliferation of healthy cells is a highly controlled process to maintain homeostasis, but cancer cells acquire means of deregulating their proliferation to endlessly divide. This uncontrolled proliferation is due to several factors including elevated levels of growth factors and their subsequent cell signaling cascades.⁷ Resistance to apoptosis and sustained proliferation are both examined in the gene regulatory sections of this dissertation (Chapters 4 and 5), as these chapters aim to inhibit overactive signaling that support disease progression.

The final hallmark of cancer progression introduced here is the ability for cancer cells to invade and metastasize to previously healthy tissues to form secondary tumors.¹ Although the cellular mechanisms underlying metastasis are still under investigation, several critical steps must occur. Briefly, cancer cells in the primary tumor proceed to induce local invasion close to the site of the primary tumor, followed by entry into the lymphatic system. Once in circulation, the cancer cells can extravasate into distant tissues to form secondary tumors.⁸ The rates of metastasis are dependent on several specific features of cancer cells, including cell adhesion and epithelial-mesenchymal transition (EMT),¹ but here we were primarily interested in using gene regulation to inhibit the formation of metastasis by inhibiting overactive oncogenic signaling, as this usually influences other metastatic behaviors.⁹ In fact, Wnt signaling has been strongly correlated with EMT and high rates of metastasis, so inhibiting this hallmark capability is a key focus in this research.^{9,10}

Importantly, many clinical strategies currently used to treat cancer focus on destroying rapidly expanding cancer cells by targeting their hallmark capabilities. Below, we describe the mechanisms of action of current treatment strategies and discuss the pitfalls that this dissertation aims to overcome.

1.1.1 Current Clinical Strategies to Treat Cancer

The standard-of-care strategies to treat cancer, including chemotherapy, radiation, and surgery, have remained relatively unchanged over the past several decades. Although they can be highly effective for some cancers depending on the stage of disease, their success is unpredictable due to the heterogeneity of each cancer. To increase the likelihood of successful treatment, patients are often given a combination of therapies. Below, we provide a brief overview of each of these therapies and the common limitations that hinder their success.

Surgery involves the removal of the primary tumor mass, and any substantial secondary lesions, directly from the host organ. This bulk removal of the tumor and adjacent tissue that has the potential of hosting local recurrence can be highly effective for early-stage disease clearance.¹¹ However, surgery is highly invasive, it is impossible to ensure that all of the diseased tissue is collected, and it does not harm circulating cancer cells or any early metastatic lesions in distant organs.¹² Additionally, the stress associated with surgery has been linked to increased rates of metastasis.^{13,14} For these reasons, surgery is often used in combination with chemotherapy and/or radiation.

Chemotherapies comprise a broad class of drugs that interfere with cancer progression. Some chemotherapy drugs cause cell cycle arrest to inhibit the high rates of proliferation that are characteristic of cancer cells to slow both primary and

secondary tumor growth.^{15,16} In addition, some chemotherapies induce apoptosis by triggering cell death pathways in cells to cause tumor regression.¹⁶ Since chemotherapeutics typically impact all cells that are rapidly dividing and growing, patients usually experience significant adverse side effects. Some minor side effects from chemotherapy include nausea, fatigue, and hair loss, but the use of chemotherapy is also associated with serious health concerns such as urinary, kidney, and heart problems that affect patients throughout their lives.^{17,18}

The final standard-of-care therapy is radiation, which is either ingested through the mouth (i.e. radioactive iodine in a pill) or applied through a radioactive beam outside the body. Put simply, the applied high energy radiation damages the DNA inside cells, which in turn causes cell death.¹⁹ Like chemotherapy, however, radiation also impacts healthy cells that are in the area of irradiation, leading to substantial adverse effects to adjacent healthy tissue. Further, a very important consideration for radiotherapy is that it can promote the formation of metastatic lesions in distant organs due to changes to the surrounding tumor microenvironment and the release of tumor cells into the bloodstream.²⁰ Together, these risks often limit the dose of radiation administered to cancer patients.

More recently, targeted therapies have been developed to specifically halt cellular pathways that are involved in disease progression. Importantly, targeted therapies have fewer side effects than the conventional strategies described above because they target cell surface receptors that are overexpressed on cancer cells relative to healthy cells.²¹ The most common forms of targeted therapies utilize monoclonal antibodies or small molecules that are specific to oncogenic cell signaling receptors.^{22,23} These therapies are currently used in a variety of cancers including

breast cancer (trastuzumab), chronic lymphocytic leukemia (alemtuzumab), and Hodgkins lymphoma (brentuximab vedotin), among others.²⁴ Targeted therapies have vastly improved the outcomes for patients with certain cancers, but many cancer subtypes are not susceptible to currently available targeted therapies. Therefore, a significant research focus is on developing targeted therapies for cancers characterized by overactive oncogenic cell signaling pathways that can benefit from highly specific therapy rather than the non-targeted strategies described above.

As previously mentioned, the three standard-of-care practices for cancer treatment are generally successful for early stage cancers, but become less successful with more advanced cancers due to their heterogeneity and higher metastatic rates. Further, all of these strategies are non-targeted, so they affect cancer cells in addition to healthy cells, leading to substantial off target effects that can be life-threatening. For these reasons, targeted therapies are deemed as promising alternatives, or they can be combined with surgery, chemotherapy, and radiation for a more cohesive approach to cancer treatment. However, targeted therapies still have dose-limiting toxicities, and their use is halted by vast tumor heterogeneity so that not all diseased cells are affected. Recently, nanoparticles (NPs) have emerged as tools to overcome many of the limitations of the therapies described above. The benefits afforded by NP systems over conventional therapies are described in Sections 1.2 and 1.3, and three unique applications of NPs are thoroughly investigated throughout this dissertation as alternative strategies to treat triple-negative breast cancer (TNBC).

1.1.2 Need for Novel Therapies for Triple-Negative Breast Cancer

TNBC accounts for 15-20% of diagnosed breast cancer cases and is associated with earlier relapse, higher mortality rates, and significantly decreased progression-

free survival compared to other subtypes of breast cancer. Interestingly, TNBC patients are more receptive to traditional chemotherapy drugs compared to non-TNBC patients, but they are significantly more likely to develop recurrent disease (64.93% vs. 45.49%, respectively) that could be lethal.²⁵⁻²⁷ Importantly, disease recurrence most commonly occurs locally, although there are high rates of both brain and lung metastases within the first 3 years after diagnosis (Figure 1.2).²⁸ For this reason, in Chapter 5 we conducted a pilot *in vivo* study investigating the use of our NP platform in a murine model of lung metastatic TNBC. Unlike other breast cancer subtypes, the cells in TNBC tumors lack expression of the estrogen, progesterone, and human epidermal growth factor 2 receptors, rendering the disease unsusceptible to clinical available targeted or hormonal therapies.^{25,29} Without any effective targeted or hormonal therapies, TNBC patients are treated with surgeries and aggressive chemotherapies that often cause toxic side effects and leads to the high rates of recurrence. Thus, novel therapies for this disease should aim to harness the metastatic potential of this disease, which is driven by overactive Wnt signaling.

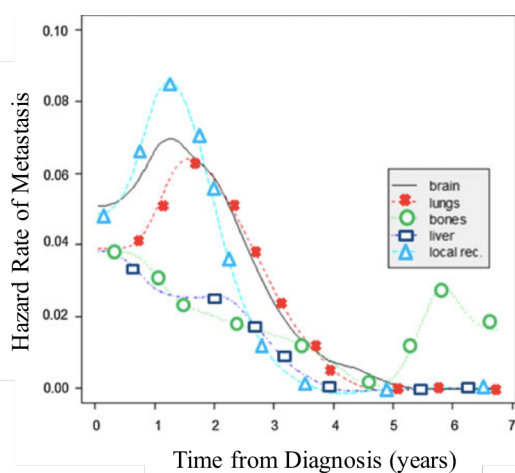


Figure 1.2: Risk of disease recurrence in distant organs following primary TNBC diagnosis. Image from *Pogoda et al., Med Oncol, 2013*.

1.1.3 Wnt Signaling as a Target for TNBC

Here, we provide an introduction to the importance of Wnt signaling in driving TNBC progression and metastasis, and further details regarding the molecular mechanisms behind Wnt signaling are described in Chapter 5. Briefly, Wnt signaling is activated in TNBC cells when extracellular Wnt3a proteins bind Frizzled7 (FZD7) receptors overexpressed on TNBC cells.³⁰ This causes intracellular β -catenin molecules to enter the nucleus and transcribe genes such as Axin2, which is considered the definitive marker of Wnt signaling activity. In this manner, aberrant Wnt signaling drives the proliferative, survival, and invasive potential of TNBC cells. Accordingly, overactive Wnt signaling has been directly linked to both primary tumor formation and to increased risk of lung metastasis.¹⁰

Due to its' role in disease progression in TNBC and other cancers, Wnt signaling inhibitors are currently being investigated in clinical trials for several types of cancer. For example, Oncomed Pharmaceuticals, Inc. has developed two antibodies that antagonize Wnt signaling through the FZD receptors. Results from these clinical trials have shown good safety and tolerability, and they are currently being investigated in combination with chemotherapy.³¹⁻³³ Importantly, Wnt signaling inhibition is correlated with adverse side effects including fragility fractures and muscle spasms, so it is critical to thoroughly evaluate the safety of Wnt inhibitors and to minimize the required dosages. Due to its' potential in TNBC, and the success of Wnt inhibitors to treat cancer, Chapter 5 in this thesis focuses on targeting Wnt signaling with antibody-coated NPs to evaluate this pathway as a therapeutic target for TNBC.

1.2 An Introduction to Cancer Nanomedicine

Nanotechnology offers many benefits over conventional treatment strategies used to treat cancer. The main underlying goals for cancer nanotechnology is to increase therapeutic efficacy and to decrease adverse side effects that often limit the success of free agents. With these efforts in mind, NP platforms can be engineered to provide several functionalities for maximal therapeutic results (Figure 1.3). First, NPs can act as delivery systems for chemotherapeutic drugs or molecular therapies either encapsulated within or conjugated to their surfaces.³⁴ In this manner, NPs can increase the stability and circulation half-life of the conjugated molecules compared to these agents alone. Second, inherently functional NPs can be engineered to mediate direct therapeutic impacts (such as heat-based therapy) and can enable enhanced imaging contrast due to their unique optical properties as described in Section 1.3.1. Third, the surface of NPs can be coated with targeting or gene regulation moieties to enhance cancer-cell specific uptake while reducing nonspecific uptake. Together, these benefits afforded to NP platforms make them ideal for difficult-to-treat cancers that require several treatment modalities within a single therapeutic platform.

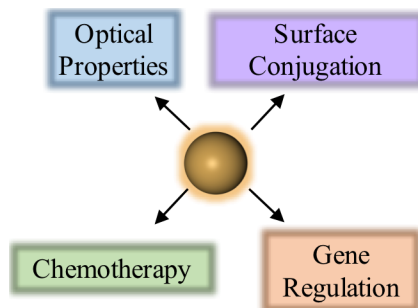


Figure 1.3: Functionalities of gold NPs. These NPs can be used for phototherapies as well as act as carriers for therapeutic agents for multifaceted approaches to cancer therapy. Image adapted from *Riley and Day, WIREs, 2017*.

1.2.1 Passive and Active Targeting of Nanoparticles

NP delivery to solid tumors and specifically to cancer cells occurs by both passive and active targeting mechanisms. In passive targeting, NPs accumulate within tumors *via* the enhanced permeability and retention (EPR) effect, which exploits the leaky vasculature and the poorly organized lymphatic system within tumors to achieve high intratumoral NP concentrations (Figure 1.4).^{35,36} These NP systems are typically coated with stealth agents, such as poly(ethylene) glycol (PEG), to increase circulation time and stability compared to completely uncoated NPs. Passive targeting is exploited in Chapter 3 of this dissertation, which utilizes NPs for heat-based therapy of cancer cells.

While passive targeting by the EPR effect is sufficient for NP accumulation within tumors, it does not enable cell-specific interactions between the NPs and the cancer cells. Further, NPs that rely on passive targeting alone are not retained within the tumor space for extended periods of time, as the EPR effect also facilitates their escape back into circulation.³⁷ To increase tumor retention and specific binding to cells, NPs can be coated with targeting ligands, such as antibodies, peptides, or aptamers, to enable active targeting. In this case, NPs accumulate within the tumor space by the EPR effect. Once within the tumor space, the exposed targeting ligands on the surface of NPs specifically bind their targeted proteins on the cancer cells (Figure 1.4). Thus, active targeting has been shown to enhance tumor retention of the NPs, which is beneficial for several reasons. First, tumor retention of NPs loaded or coated with therapeutic agents is necessary to increase the amount of those agents delivered to the tumor cells, thus decreasing off-target effects. Further, specific binding of NPs to their targeted cell surface receptor may interfere with the oncogenic cell signaling pathway downstream of the targeted receptor. In Chapter 5, we explore

how actively targeted NPs can be used to both specifically bind TNBC cells and to interfere with oncogenic cell signaling.

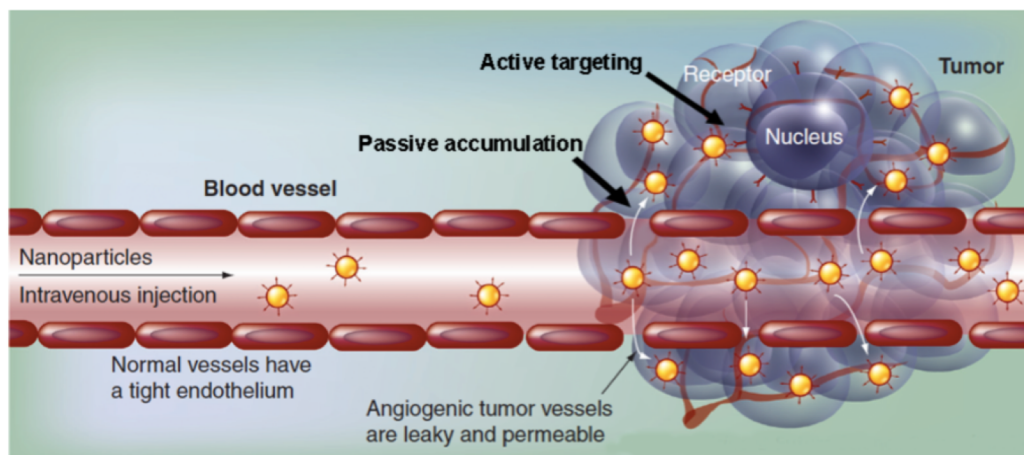


Figure 1.4: Passive and active targeting of NPs. Following intravenous injection, NPs accumulate within solid tumors due to their increased permeability and leaky vasculature. Upon entry into the tumor space, ligand-functionalized NPs specifically bind their targeted receptor on the cancer cells for improved retention and delivery. Image from *Dong and Mumper, Nanomed, 2010*.

1.2.2 Current Clinical Status of Nanoparticle-Based Cancer Therapies

Several NP systems have gained approval from the Food and Drug Administration (FDA) for cancer treatment. The most widely used NP platform is Doxil, which consists of a PEGylated liposomal formulation of the chemotherapy drug doxorubicin.³⁸ Several other liposomal formulations of chemotherapy drugs have since been approved including DaunoXome (daunorubicine) and Marquibo (vincristine).³⁹ Additionally, there are other polymeric and micelle formulations of chemotherapy drugs under investigation in clinical trials.³⁹ Although these formulations have gained attention for improving the half-life and stability of the drugs, it is important to note that these technologies are not targeted to diseased tissues, so they still cause

significant toxicity to healthy tissue.⁴⁰ Therefore, more recently targeted NPs have been introduced into the clinic.

Targeted NP systems in particular are expected to become widely apparent in the coming years. As such, the number of publications that studied targeted NP systems have exponentially increased since the year 2000 (Figure 1.5).³⁷ Although they are yet to be approved by the FDA, there are several targeted NPs currently in Phase I and II clinical trials for a variety of solid tumor cancers, several of which are showing great promise.³⁹ The common goal of these targeted systems is to improve upon tumor-specific delivery of the loaded cargo by exploiting overexpressed cell surface receptors on cancer cells.^{41,42} Sonna, *et al.* and Anselmo, *et al.* presented thorough reviews of targeted NP systems currently under investigation in clinical trials.^{39,42} The majority of these targeted NPs are either liposomal or polymeric because these materials are biocompatible and porous, thus enabling passive diffusion of the loaded cargo following delivery to the tumor site. Harder materials, such as gold, have not been as extensively investigated in clinical trials, but we anticipate their growth in the coming years.

Although there are no gold-based NP systems that are currently approved by the FDA, there are a few ongoing and completed clinical trials that utilize gold NPs specifically for phototherapies.⁴³⁻⁴⁷ Among the various types of gold NPs, NSs coated with PEG (also known as AuroShells, which are being commercialized by Nanospectra Biosciences, Inc.) are the furthest along in development and are currently the only gold NPs being evaluated in clinical trials for photothermal therapy (PTT), which is described below and was extensively studied in Chapter 3 of this dissertation. These trials are examining the safety and efficacy of NS-mediated PTT against lung,

head and neck, and prostate cancers,^{45–47} and the first publication regarding these human trials indicates that PEG-coated NSs have an excellent clinical safety profile.⁴⁸ Although there are several clinical trials ongoing, efficacy data from these trials has not yet been published.³⁴ Due to their extensive investigation and publication records, as well as their therapeutic properties described in Section 1.4, we used NSs as the base platform throughout this thesis.

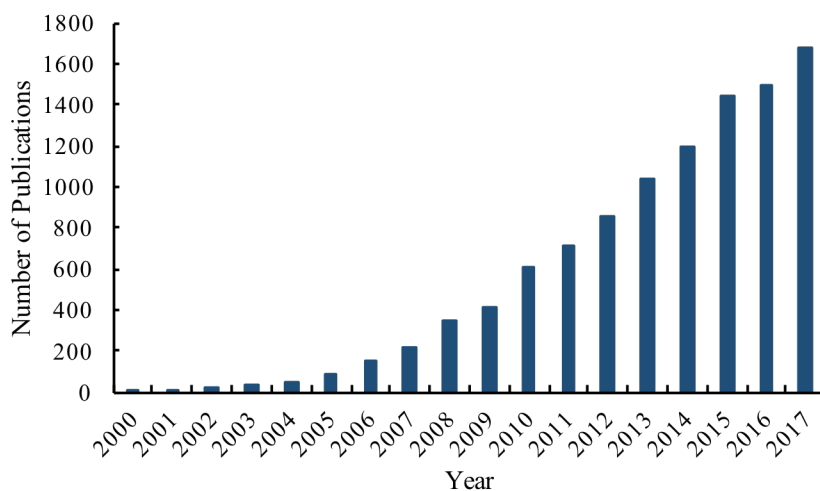


Figure 1.5: Number of targeted NP publications. The number of annual publications found in PubMed using the search terms “targeted nanoparticle” since the year 2000. Figures from *Valcourt, et al., Nano Research, 2018*.

1.3 Gold-Based Nanoparticles in Oncology Research

Several types of NPs have been developed for cancer therapy including polymers, lipids, and metals, which each have unique benefits and important limitations.^{49–51} For example, soft materials such as polymers and lipids are porous, and therefore are ideal for loading molecules into their cores. Further, certain soft materials are biodegradable, so they can be used to release their loaded cargo at the diseased site in response to external stimuli, changes in pH, or other triggers.⁵²

Alternatively, gold-based NPs, which can be either solid or hollow,⁵³ provide several benefits for oncology research over their softer counterparts. For example, gold NPs enable simple gold-thiol bioconjugation chemistry for surface functionalization with therapeutic molecules, targeting ligands, or passivating agents (such as PEG) for enhanced targeting and biocompatibility.³⁴ Additionally, the optical properties of gold NPs can be tuned by controlling their structural dimensions, which is a critical feature for phototherapies that utilize specific wavelengths of light. These benefits, along with other benefits afforded by NSs specific to the work presented in this thesis, are further explained in the subsections below.

1.3.1 Photoresponsive Nanoparticles for High Precision Cancer Therapy

Nanoparticle-mediated PTT has rapidly advanced as a standalone therapy for cancer because it enables selective hyperthermia of tumor tissue while avoiding damage to healthy tissue not in the area of irradiation. In PTT, plasmonic NPs are delivered into tumors and irradiated with laser light, which causes the NPs' conduction band electrons to undergo synchronized oscillations that result in either the absorption or scattering of the applied light.⁴³ The absorbed light is converted into heat, which irreversibly damages the surrounding diseased tissue (Figure 1.6).

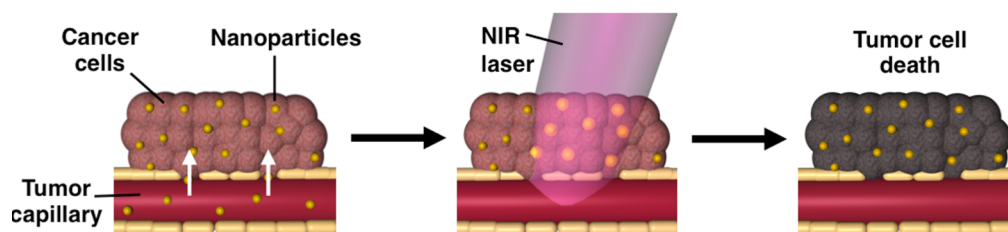


Figure 1.6: The steps of photothermal therapy. In PTT, systemically delivered nanoparticles accumulate within solid tumors *via* the enhanced permeability and retention effect, which exploits the leaky tumor vasculature. Once within the tumor, near infrared light is applied to cause the nanoparticles to generate heat to kill the surrounding tumor tissue. Image from *Riley and Day, WIREs, 2017*.

NPs used in photothermal applications must meet several design criteria such as having plasmon resonance tunability, high photothermal conversion efficiency,^{54,55} and simple surface functionalization or encapsulation chemistry. Based on these design criteria, NSs, nanorods (NR), nanocages (NC), and nanostars have emerged as the most common gold-based photothermal transducers (Figure 1.7).^{43,56} These NP platforms have been specifically designed to maximally absorb near infrared (NIR) light. It is ideal that any phototherapy is designed to be responsive to light within the first (650-850 nm) or second (950-1350 nm) NIR windows because these wavelengths of light can safely and deeply penetrate healthy tissue to reach NPs embedded within tumors.³⁴ To demonstrate this concept, Figure 1.8 shows that native tissue components, such as water and hemoglobin, minimally absorb light in the first NIR window. An important feature of gold NPs is that their structural dimensions can be tuned to yield maximal absorption within one of these two regions of light. The majority of gold NPs have been designed to have maximal light absorbance within the first NIR window, which can safely penetrate 2-3 cm of tissue. For example, the NR length can be shortened or elongated to achieve peak longitudinal surface plasmon resonance in the NIR region.⁵⁷⁻⁵⁹ Similarly, NSs can be engineered to maximally absorb specific wavelengths of NIR light as described in detail in Section 1.4 below.

In addition to NP structure, the mode of light irradiation is also critical to the success of phototherapies. For example, traditional PTT discussed above uses continuous wave (CW) laser light tuned to the NPs peak plasmon resonance wavelength to activate the NPs embedded within tumors, which subsequently produce heat to directly kill nearby cancer cells. Thus, heat produced by CW-mediated PTT is a result of collective activation of the bulk amount of NPs.⁶⁰ Alternatively, pulsed

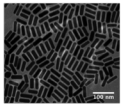
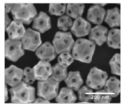
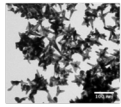
	Nanoshells	Nanorods	Nanocages	Nanostars
Schematic				
SEM				
Size for PTT	~150 nm diameter	~10 nm x 40 nm	~40-60 nm length	~45-120 nm
Stage of Development	Clinical trials: lung, head, neck cancer	Preclinical	Preclinical	Preclinical
Unique Features	Large surface area, stable structure	Two absorption peaks	Drug loading capabilities	Large surface area for bioconjugation

Figure 1.7: Types of gold NPs for phototherapy. Four of the most commonly employed gold NPs for photothermal applications include silica core/gold shell nanoshells, gold nanorods, hollow gold nanocages, and nanostars. Image from *Riley and Day, WIREs, 2017*.

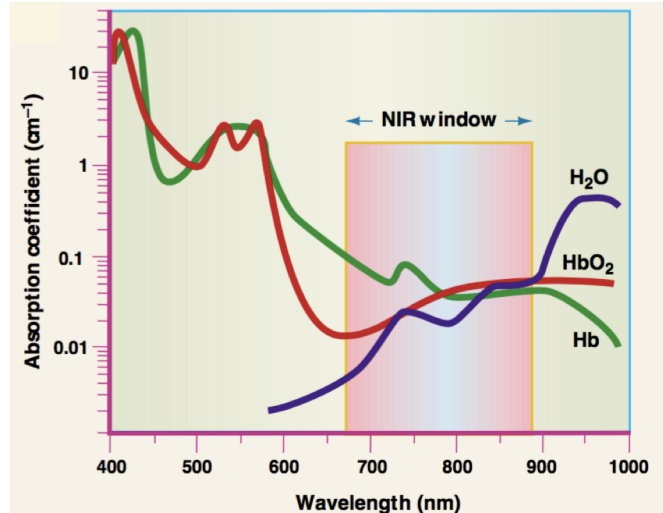


Figure 1.8: Light absorbance by tissue. Light in the NIR region is ideal for phototherapies because these wavelengths are minimally absorbed by native tissue components such as hemoglobin and water. Image from *Weissleder, Nature Biotech, 2001*.

laser irradiation, in which high energy, ultrafast pulses of laser light are used to activate NPs, are useful for other types of phototherapy. Pulsed light causes individual NPs to generate localized energy within the immediate vicinity of the NPs. This is believed to occur *via* a hot electron transfer effect, and the energy produced can release any molecules conjugated to the NP surfaces.⁶¹ This feature in particular is ideal for spatial and temporal control over gene regulation as discussed in Section 1.3.2 and as explored in Chapter 4. Since both CW and pulsed laser irradiations cause significantly different responses, it is critical to specifically design NP systems based on the desired therapeutic outcome. Therefore, a main theme in this thesis is to demonstrate the ability for NSs to mediate either heat-based PTT (Chapter 3) or to act as carriers for siRNA to enable on-demand gene regulation (Chapter 4), thus making NSs a robust platform for a variety of cancer therapeutic strategies.

The main challenge of phototherapies is that they are mainly used to treat primary tumors, as they do not affect metastatic lesions or tumor cells outside the area of irradiation. To enhance overall treatment outcomes by also influencing metastasis, gold NPs can be used for delivering additional therapeutic agents in combination treatment strategies. In this manner, the gold NPs can be used as molecular carriers, can enable optical imaging and high precision phototherapies due to their unique light properties, and can enable overall more successful therapy compared to individual treatment options by also inhibiting the growth of secondary tumors. In the sections below, we provide background information on the use of gold NPs for mediating or supplementing additional therapeutic strategies as investigated throughout this thesis.

1.3.2 Gold Nanoparticle Carriers for Gene Regulation *via* RNA interference

Gene regulation is a technique that aims to treat cancer by using nucleic acids to inhibit the expression of genes that drive tumor progression, and it is particularly promising for targets that are considered “undruggable” by small molecules due to lack of an effective binding site. The main type of nucleic acid used for gene regulation is small interfering RNA (siRNA), which suppresses gene expression by triggering degradation of targeted messenger RNA molecules inside the cell cytoplasm *via* RNA interference.^{34,62–64} In RNAi, exogenously delivered siRNA molecules are loaded into the RNA-induced silencing complex (RISC) in the cell cytoplasm (Figure 1.9).⁶⁵ Once loaded into RISC, the double stranded siRNA molecules unwind and the two strands separate. The antisense siRNA strand remains bound to RISC, which guides it to its’ complementary messenger RNA (mRNA) strand. This results in the cleavage and reduction of the target mRNA, halting the transcription of the encoded protein.⁶³ While siRNA-mediated RNAi is a promising therapeutic technique to silence the expression of proteins crucial for disease progression, several challenges have hindered the translation of gene regulation from the laboratory to the clinic. First, siRNA molecules are rapidly cleared from the bloodstream and are quickly degraded by nucleases. Second, siRNA is negatively charged, so they cannot passively cross negatively charged cell membranes. Thus, intracellular delivery requires cationic transfection reagents that may be toxic to cells, thereby precluding their use *in vivo*. Further, many siRNA delivery strategies are not cell-specific, and therefore may lead to uptake and gene silencing in all cell types. To overcome these limitations, researchers have recently demonstrated that conjugating siRNA to the surface of gold NPs can increase siRNA stability and intracellular delivery without the need for transfection reagents.^{66–68}

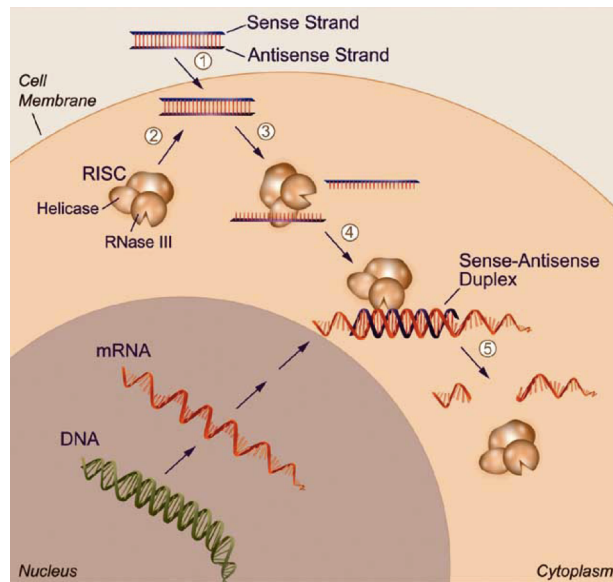


Figure 1.9: Mechanism of RNA interference using siRNA. Upon cellular entry, siRNAs are loaded into RISC, which separates the sense and antisense strands. The antisense strand then cleaves complimentary mRNA to halt the transcription of the encoded protein. Image from *Crooke, Annu. Rev. Med., 2004*.

Gold NPs have been exploited as tools for gene regulation because they offer simple bioconjugation chemistry, enabling them to carry siRNAs or other nucleic acids for enhanced stability, intracellular delivery, and gene regulation both *in vitro* and *in vivo*.^{66,68,69} The most common gold NP carrier for gene regulation are ultrasmall solid gold NPs (~13 nm in diameter). The benefit of these siRNA carriers is that their spherical structure changes the manner in which they are presented to cells so that they are taken up more efficiently than free siRNA.⁷⁰⁻⁷² However, there are challenges to achieving sufficient gene regulation with gold NP carriers. First, they often become trapped within intracellular compartments upon endocytosis, rendering them ineffective.⁷³ To account for this, researchers have coated NPs with cell penetrating peptides and polymers to enhance endosomal escape.^{73,74} However, these systems are not tumor cell-specific and therefore cause widespread gene regulation in healthy as

well as diseased tissues, and the added molecules can be inherently toxic. By engineering the core material to be responsive to external stimuli, we hypothesized that siRNA-NS conjugates could enable spatial and temporal control over gene regulation. To meet this need, Chapter 4 in this thesis presents a novel NP platform that serves as an siRNA carrier system as well as enables on-demand gene regulation in response to light by exploiting the optical properties of NSs.

1.3.3 Antibody-Gold Nanoparticle Conjugates for Signal Cascade Interference

Many targeted therapies that are highly successful for treating cancer utilize antibodies that antagonize the function of their targeted receptor on cells by blocking overactive cell signaling.⁷⁵ In this manner, antibodies provide an indirect means of regulating cell signaling and the expression of genes involved in cancer progression. However, their use is limited by high production costs and adverse side effects that limit the administered dosages.^{76,77} More recently, it was discovered that antibodies coated onto NPs yield increased binding affinity compared to unbound antibodies due to the inherent multivalency afforded by the NP carrier itself.^{78,79} In this phenomenon, antibodies conjugated to the surface of NPs can bind several targeted antigens to increase the binding avidity between the ligands and the targeted cell surface receptors (Figure 1.10). Therefore, ligand-functionalized NPs are recognized as a promising means to improve upon therapeutic molecules with defined biological properties.⁸⁰ While the ability to enable cell-specific binding of NPs coated with antibodies has been thoroughly investigated, the impact that this increased binding avidity has on the signaling pathway specific to the targeted receptor remains unknown. By increasing the binding avidity between antibody and receptor, we anticipated that multivalent binding could decrease the amount of antibodies necessary

to halt oncogenic cell signaling. In Chapter 5, we further explain how multivalency is a key benefit of NPs in cancer therapy, and we investigate the use of antibody-targeted NSs to inhibit Wnt signaling in TNBC.

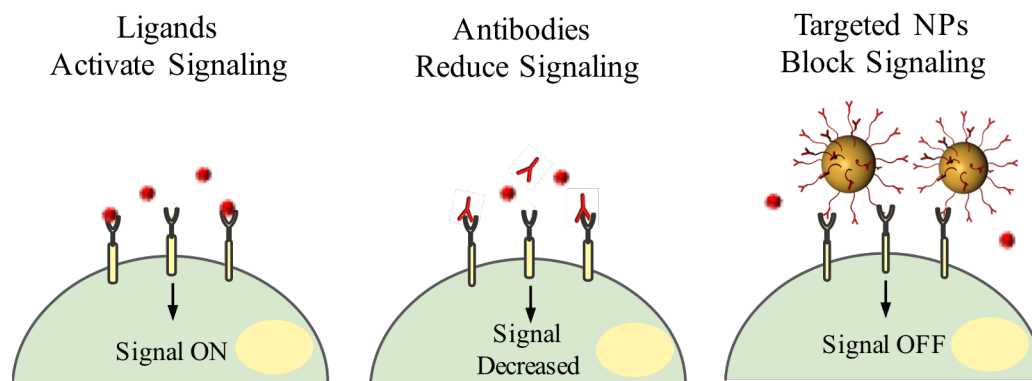


Figure 1.10: Multivalent binding of antibody-NP conjugates. Simplified schematic showing multivalent binding of antibody-NP conjugates for downstream signaling cascade interference.

1.4 An Introduction to Silica Core/Gold Shell Nanoshells

In this thesis, we used NSs comprised of silica cores and gold shells as the base material for three unique platforms for cancer therapy for several reasons. First, bare NSs are ~150 nm in diameter and thus they are small enough to enable tumor penetration by passive targeting while providing a large surface area for functionalization with biomolecules to be used for active targeting and gene regulation. Second, the gold surface of NSs enables simple bioconjugation of antibodies, siRNA, and PEG to their surfaces using gold-thiol bonding. Third, the unique core:shell structure of NSs makes them excellent photothermal transducers for both traditional heat-based PTT as well as for pulsed laser-induced release of conjugated molecules. Likewise, the precise structure of NSs can be engineered to maximally absorb NIR light as described in detail in Section 1.4.2. These optical properties also enable NS visualization by two photon microscopy and other imaging

modalities that are utilized throughout this dissertation. Finally, NSs are the furthest along in clinical development compared to other types of gold NPs, and they have proven safety in clinical trials.^{45,46,48} Due to their current clinical status, we anticipate that NSs are poised to reach clinical translation in the near future, and the platforms described in this thesis demonstrate how NSs can be adapted for multifunctional and robust strategies for cancer therapy.

1.4.1 Engineering the Size and Structure of Nanoshells for Cancer Imaging and Therapy

The specific design and structure of NSs used in this thesis was carefully chosen based on the optical properties. This behavior can be described by Mie scattering, which explains the light scattering properties of concentric spheres in solution.^{54,81,82} Using Mie theory, Oldenburg *et al.* showed how the light absorbance properties of NSs can be adjusted based on the gold shell thickness (Figure 1.11A).⁸² NSs with 120 nm diameter cores and 15 nm thick shells are typically used for phototherapies because they maximally absorb ~800 nm light and enable optical imaging and phototherapies as described below (Figure 1.11B).

Due to the high scattering profile of NSs, they can be visualized under several imaging modalities at both the tissue and cellular level. For example, NSs provide reflective signal beyond the native tissue itself in optical coherence tomography (OCT), so tumors harvesting NSs display enhanced OCT signal compared to tissue without NSs.⁸³ In addition to tissue imaging, NSs can also be visualized under darkfield microscopy and two-photon microscopy (TPM) for *in vitro* experiments. Darkfield imaging captures any light scattered from the illuminated specimen, so NSs appear as bright spots on relatively dark specimens due to their high scattering profile

(this feature of NSs can be seen in Chapter 4). Alternatively, in TPM, NSs emit light in response to a pulsed NIR laser tuned to their peak plasmon resonance wavelength. Using TPM, targeted NPs can be visualized bound to cancer cells to assess specific binding and uptake, and this capability is demonstrated in Chapter 5.^{34,81,84}

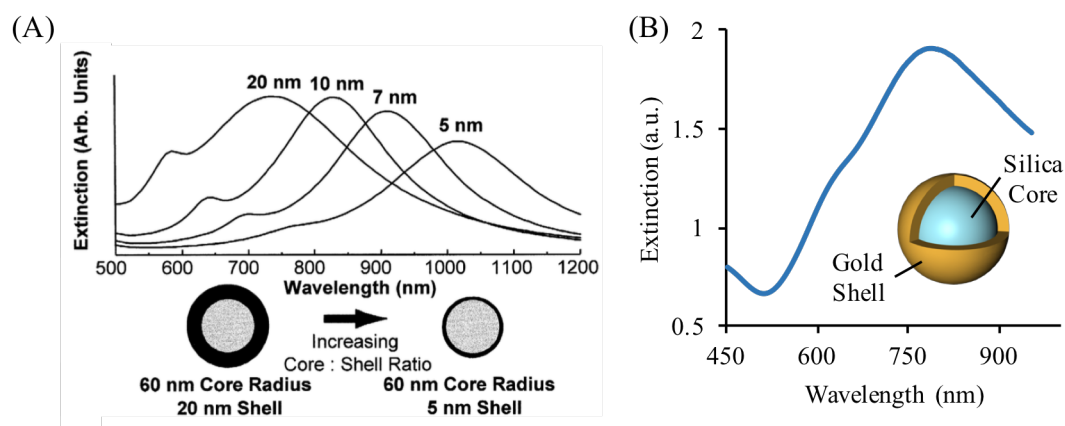


Figure 1.11: Absorbance properties of NSs. (A) The theoretical light absorbance properties of NS dependent on the core:shell thickness ratio based on Mie theory. Image from *Oldenburg et al, Chem Phys Letters, 1998*. (B) Characteristic absorbance spectrum of silica core/gold shell NS with 120 nm silica cores and ~15 nm thick gold shells, as used throughout this thesis.

1.4.2 Opportunities for Nanoshells in Cancer Therapy

NSs were used as the core material throughout this thesis work because of their inherent benefits described above, and each chapter in this thesis exploits several of these unique characteristics (Figure 1.12). To begin, Chapter 2 explains the synthesis procedures used to make NSs and to functionalize them with PEG, antibodies, and siRNA, as at least one of these platforms is used in each chapter this dissertation. In Chapter 3, we explored a treatment strategy for TNBC that combines NS-mediated PTT with photodynamic therapy (PDT) using a novel photosensitizer synthesized by our collaborators, with the expectation that dual PTT/PDT would be more effective to induce apoptotic cancer cell death than either therapy alone. Chapter 4 evaluates the

ability for NSs to be used as the platform for on-demand gene regulation. To do this, we investigated how the dielectric properties of NSs can cause surface-bound siRNA to release from the NS surface in response to pulsed laser irradiation to ultimately induce triggered gene knockdown. In Chapter 5, antibody-coated NSs are used to demonstrate how multivalent NP binding can influence oncogenic cell signaling both *in vitro* and in a pilot *in vivo* study of murine lung metastatic TNBC. Finally, Chapter 6 summarizes the importance of the results presented in this dissertation in a broad context and discusses the potential opportunities and challenges faced by nanotechnology for cancer therapy in the future. Importantly, the tools developed here are adaptable to treat a wide variety of cancers, and this is a critical feature afforded by nanomedicine for cancer treatment.

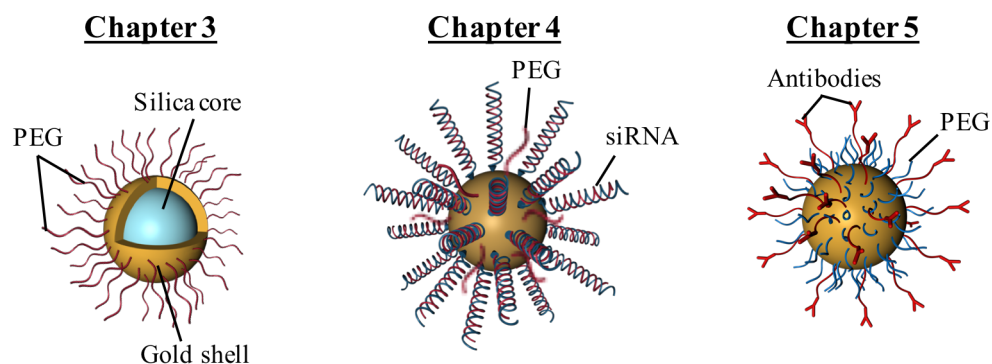


Figure 1.12: NS conjugates used in this dissertation including PEG-NS (left), siRNA-NS (middle), and antibody-coated NS (right). Surface coatings not to scale.

Chapter 2

MATERIALS AND METHODS FOR NANOSHELL SYNTHESIS, FUNCTIONALIZATION, AND CHARACTERIZATION

This chapter presents the overarching materials and methods used throughout this dissertation for nanoparticle synthesis, functionalization, and characterization. Additional materials and methods specific to each chapter are presented later in this dissertation.

2.1 Synthesis of Silica Core/Gold Shell Nanoshells

Nanoshells with 120 nm diameter spherical silica cores and ~15 nm thick gold shells were synthesized according to Oldenberg *et al* (Figure 2.1).⁸² First, colloidal gold was prepared as described by Duff *et al.*⁸⁵. To do this, 33 mL of ultrapure water was combined with 400 μ L tetrakis(hydroxymethyl)phosphonium chloride (THPC, Sigma) to prepare a THPC stock solution. In a separate beaker, 180 mL of ultrapure water heated to 37°C was mixed with 1.2 mL 1 M sodium hydroxide (NaOH, Fisher) and mixed for 2 min. Then, 4 mL of the THPC stock solution was added to the NaOH solution and was stirred for 5 min. Lastly, 6.75 mL of 29.7 gold(III) chloride trihydrate (HAuCl_4 , Sigma) was added to the solution while rapidly mixing, and the beaker was removed from the stir plate once the solution turned light brown (~1 sec). The colloid solution was aged for 3-5 days until the particles reached the correct size as determined by UV-vis spectrophotometry.

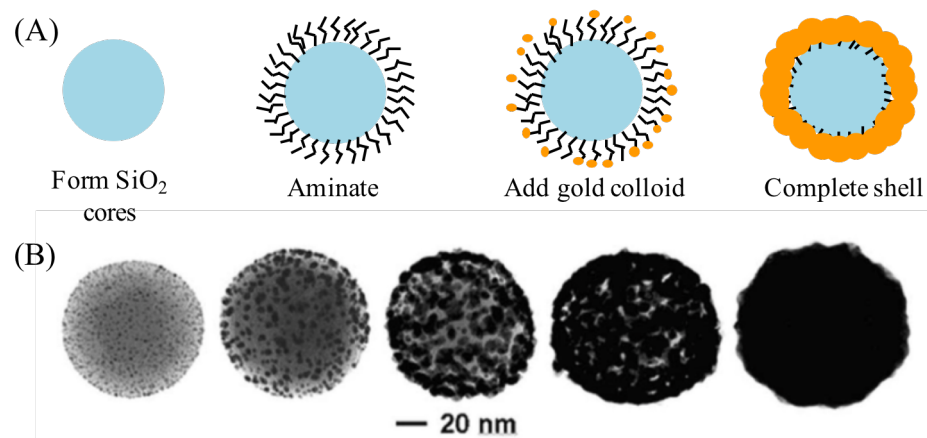


Figure 2.1 NS synthesis. (A) Cross-section schematic of NS synthesis and (B) TEM images showing development of the gold shell on silica cores. Adapted from *Oldenburg et al, Chem Phys Letters, 1998*.

Silica cores (120 nm) were purchased (Nanocomposix) pre-functionalized with (3-aminopropyl) triethoxysilane (APTES) and were diluted to 40 mg/mL in ethanol. Once aged, 40 mL of the colloid solution was combined with 4 mL 1M sodium chloride (NaCl) and 300 μ L silica cores, and this solution was rocked at room temperature for 3-7 days, during which the gold colloid attached to the silica cores to produce evenly dispersed gold nucleation sites to form the “seed” solution. After aging, of the seed solution was determined by performing a sweep of seed diluted to an optical density (OD) of 0.1, and then the proper amount of seed to make NSs was determined. Briefly, different amounts of seed ranging from 100 μ L to 500 μ L were mixed with 1 mL potassium carbonate-gold (KCarb-gold) solution and 10 μ L of 37% formaldehyde. In this procedure, the KCarb-gold provides excess gold to complete the gold shell using formaldehyde as the catalyst. The correct volume of seed used to make NSs was determined by analyzing the optical properties of the resultant NSs using the characterization methods described in Section 2.3. The NS batches were then scaled up according to the optimal concentration of seed determined by this assay.

Lastly, NSs were purified twice by centrifugation with re-suspension in water and were stored at 4° C until use.

2.2 Nanoshell Functionalization with methoxy-poly(ethylene) glycol (mPEG), Antibodies, and siRNA

Throughout this dissertation, all NSs used were coated with antibodies, siRNA, and/or a PEG backfill. In these platforms, the antibodies and siRNA serve as the biological moieties that mediate gene regulation, and the PEG backfill increases NS stability, decreases nonspecific protein adsorption, and enhances circulation time in *in vivo* settings. All NS conjugations described below utilize a thiol (SH) on one end of the PEG linker or backfill that is utilized for bioconjugation to the gold surfaces of NSs.

2.2.1 Methoxy poly(ethylene) glycol (mPEG-SH) Attachment to Nanoshells

NSs coated with only mPEG-SH (PEG-NS) were used as controls in most experiments described in this dissertation. To coat NSs with mPEG-SH, NS solutions diluted to 4.1×10^9 NS/mL in ultrapure water were combined with 5 kDa mPEG-SH to a final PEG concentration of 2.5 μ M and reacted overnight at 4°C. Then, PEG-NS were centrifuged to remove unbound mPEG-SH molecules, and concentrated PEG-NS were stored at 4°C in ultrapure water until use.

2.2.2 Antibody Conjugation to Nanoshells

Antibodies were first linked to 2 kDa orthopyridyl disulfide-PEG-succinimidyl valerate (OPSS-PEG-SVA, Laysan Bio) in sodium bicarbonate. Nine parts OPSS-PEG-SVA were reacted with 1 part antibody at a 2:1 PEG-to-antibody molar ratio overnight at 4°C to form PEGylated antibodies (Figure 2.2, A). Then, the PEGylated

antibodies were purified by dialysis using microdialysis devices (Spectrum Labs). Finally, antibodies were added to solutions of NSs in ultrapure water at 1250 antibodies/NS and were reacted for 4 h at 4°C. Then, 5 kDa mPEG-SH was added to the NS solutions to a final concentration of 2.5 μM and reacted overnight at 4°C (Figure 2.2, B). NSs were purified *via* centrifugation (1500 xg, 10 min) to remove unbound antibodies and mPEG-SH with the supernatant, and functionalized NSs were stored at 4°C in ultrapure water until use.

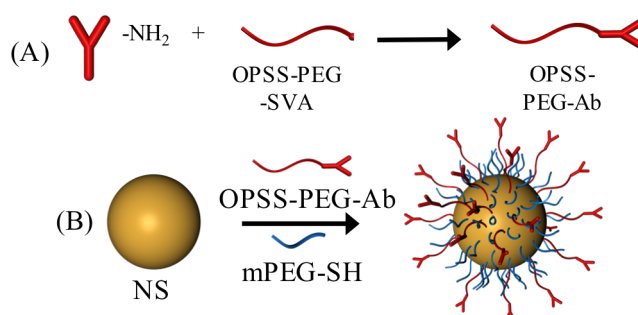


Figure 2.2: Schematic of antibody conjugation to NSs. (A) First, antibodies are combined with OPSS-PEG-SVA to form OPSS-PEG-Ab. (B) Then, OPSS-PEG-Ab and mPEG-SH are added to NSs to form Ab-NS conjugates.

2.2.3 Conjugation of siRNA to Nanoshells

Prior to any siRNA work throughout this dissertation, all working solutions were purchased or treated to be RNase-free by adding 0.01% diethyl pyrocarbonate (DEPC) for 15 min at 37 °C prior to autoclaving. NS solutions were rendered RNase-free by treating with 0.01% DEPC for three days at 37°C.

siRNA oligonucleotides were purchased as single strands from IDTDNA. Thiolated sense strands were mixed with complementary non-thiolated antisense strands in equimolar amounts, boiled at 95°C for 5 min, and then slowly cooled to 37°C over 1 hr to facilitate siRNA duplexing. In this manner, the 3' end of the sense

strand was directly attached to the gold surface via gold-thiol bonding, and the antisense strand was attached to the sense strand by complementary base pairs. The RNase-free NSs were diluted to 4.1×10^9 NS/mL (corresponding to OD 1.5) in milliQ water, and Tween-20 and 5 M NaCl were added to final levels of 0.2% and 20 mM, respectively. siRNA duplexes were added to NSs to a final concentration of 200 nM, and the solution was bath sonicated and rocked at room temperature. Samples were salt aged incrementally to a final NaCl concentration of 400 mM prior to rocking overnight. Next, 5 kDa methoxy-poly(ethylene) glycol-thiol (mPEG-SH) was diluted in milliQ water to 1 mM and added to NSs to a final concentration of 5 μ M mPEG-SH (Figure 2.3). After rocking for 4 hr at 4°C, the NS solutions were purified by centrifugation 3 times, resuspended 1X RNase-free phosphate buffered saline (PBS), and stored at 4°C until use.

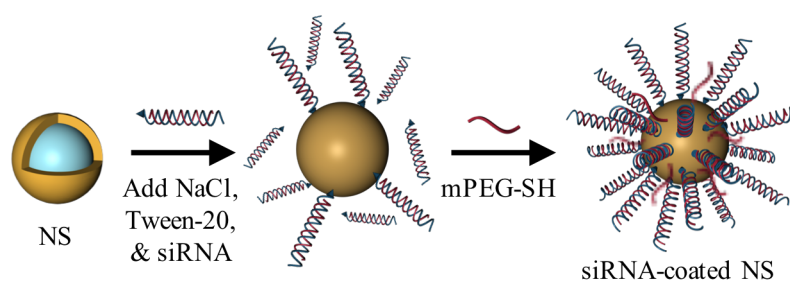


Figure 2.3: Schematic showing siRNA conjugation to NSs. First, NSs are combined with 5 M NaCl, Tween-20, and siRNA. Then, mPEG-SH is added as backfill for stability and increased circulation time.

2.3 Characterization Methods

The methods described in this section are used throughout this dissertation to characterize NSs and quantify loading of biomolecules attached to their surfaces.

2.3.1 Scanning Electron Microscopy (SEM)

SEM was used to evaluate the size, dispersity, and structure of silica cores and complete NSs. To prepare samples, silica cores or NSs were diluted in ethanol and 50 μL was added dropwise to SEM stubs, which were then dried in a covered chamber until the ethanol was evaporated. Stubs with silica cores were run on the sputter coater and coated in platinum to ensure visibility on the SEM. NSs were imaged on a Hitachi S4700 SEM without further modification.

2.3.2 Ultraviolet-Visible Spectrophotometry (UV-vis), Dynamic light scattering (DLS), and Zeta Potential Measurements

NSs (bare or coated with PEG, antibodies, and/or siRNA) were characterized by UV-vis to assess their optical properties, which are indicative of shell structure and thickness. Solutions of NSs were diluted in ultrapure water, placed into disposable cuvettes, and scanned from 400-1100 nm light on a Cary60 spectrophotometer using a scan rate of 2400 nm/sec, and a baseline was subtracted from the scan. NS concentration was determined using the peak absorbance and Beer's law. For reference, an optical density (OD) of 1.5 corresponds to $\sim 4.1\text{E}9$ NS/mL. NSs used for experiments in this dissertation distinctly produced four important UV-vis features: (i) a narrow peak at ~ 800 nm, (ii) a secondary hump at ~ 600 nm, (iii) a trough at ~ 500 nm, and (iv) a peak:trough absorbance ratio of at least 3:1. These features are critical to ensure the NSs have complete gold shells, are monodisperse with a diameter of ~ 150 nm, and are efficient photothermal converters.

For DLS and zeta potential measurements, NS solutions were diluted to $2.7\text{E}9$ NS/mL or $4.1\text{E}9$ NS/mL in ultrapure water. Samples were placed into disposable cuvettes for DLS or Zeta cuvettes for zeta potential analysis. Samples were analyzed

with an AntonPaar Litesizer 500 to measure the hydrodynamic diameter (z-average) and zeta potential, and the average of 3 runs was calculated.

2.3.3 Quantification of Surface-Conjugated Antibodies

Conjugation of antibodies to NSs was confirmed and quantified using a solution-based enzyme-linked immunosorbent assay (ELISA) as previously described.⁸⁶ Briefly, antibody-coated NSs diluted to 4.1×10^9 NS/mL in ultrapure water were incubated with 10 $\mu\text{g/mL}$ horseradish peroxidase (HRP)-conjugated secondary IgG antibodies (HRP-Ab, KPL) for 1 h at room temperature. Samples were pelleted by centrifugation (500 g, 5 min, thrice) to remove unbound secondary antibodies in the supernatant and were then suspended in 3% bovine serum albumin in 1X PBS (PBSA). Samples were further diluted 10X in 1X PBS prior to analysis. Then, 70 μL sample was developed in 700 μL 3,3',5,5'-tetramethylbenzidine (TMB, Sigma-Aldrich) for 15 min and then 200 μL sulfuric acid was added to stop the reaction. Absorbance at 450 nm was measured on a Cary60 spectrophotometer and compared to a standard curve of known HRP-Ab concentration to calculate the number of antibodies/NS.

2.3.4 Quantification of Surface-Conjugated siRNA

To quantify the number of siRNA loaded onto NSs, 200 μL of NSs diluted to 4.1×10^9 NS/mL was combined with 200 μL urea, then this solution was heated and mixed at 45°C for 20 min. The solution was centrifuged and the siRNA-containing supernatant was collected. siRNA content on NSs was quantified using the inherent fluorescence of the siRNA (such as in Chapter 4) or using the Quant-iT OliGreenTM ssDNA quantification kit (Thermo Fisher) according to manufacturer

recommendations and as detailed previously.⁸⁷ Sample fluorescence was read on a Biotek Synergy H1 microplate reader and compared to a standard curve of known antisense or duplex concentration (0-20 nM), while accounting for NS concentration to calculate the number of siRNA antisense strands or duplexes per NS.

Chapter 3
DUAL PHOTOTHERMAL AND PHOTODYNAMIC THERAPY
AS A COMBINATORIAL STRATEGY TO TREAT
TRIPLE-NEGATIVE BREAST CANCER

3.1 Introduction to Chapter 3

Light-activated therapies are ideal for treating cancer because they are non-invasive and are highly specific to the area of irradiation. Photothermal and photodynamic therapies (PTT and PDT, respectively) are two types of light-activated therapies that show great promise for treating solid tumors. In PTT, nanoparticles embedded within tumors emit heat in response to continuous wave near-infrared light irradiation (Figure 1.6), and this heat induces cancer cell death by triggering either necrosis or apoptosis based on the applied irradiation times and powers.⁸⁸ In PDT, photosensitizers (PS) activated with light transfer the absorbed energy to adjacent ground state tissue oxygen molecules to produce toxic singlet oxygen that kills cancer cells by DNA damage and other mechanisms.^{89,90} In this Chapter, we investigated the use of a novel photosensitizer, palladium 10,10-dimethyl-5,15-bis(pentafluorophenyl)biladiene modified with PEG (Pd[DMBi1]-PEG₇₅₀) to mediate PDT of TNBC cells. Further, we evaluate a combinatorial therapeutic approach to treat TNBC in which NSs were combined with Pd[DMBi1]-PEG₇₅₀ to enable dual PTT/PDT, with the anticipation that dual delivery could overcome the limitations of each individual therapy, as described in more detail in Section 3.1.3. The work

presented in Chapter 3 was performed in collaboration with Andrea Potocny, a graduate student in Dr. Joel Rosenthal's lab in the Chemistry Department at the University of Delaware, who performed the synthesis and characterization of Pd[DMBil1]-PEG₇₅₀. Some of this is under revision for publication in a manuscript titled "Photochemotherapeutic Properties of a Linear Tetrapyrrole Palladium(II) Complex Displaying an Exceptionally High Phototoxicity Index," *Journal of Inorganic Chemistry*. Further, some of the text has been adapted from my co-authored article: Melamed JR, Edelstein (Riley) RS, Day ES. "Elucidating the Fundamental Mechanisms of Cell Death Triggered by Photothermal Therapy," *ACS Nano Perspective*. 2015: 9(1);6-11.

3.1.1 Photodynamic Therapy by a Novel Photosensitizer

PDT is used clinically as a non-invasive treatment for solid tumors. In PDT, photosensitizing compounds are either intratumorally or intravenously injected and circulate throughout the body prior to accumulating at the tumor site where they are irradiated with an externally applied light source. Photosensitizers present within the illuminated tissue absorb the light and transfer energy to ground state molecular oxygen to produce toxic ¹O₂ that ultimately induces localized cell death (Figure 3.1A) in the area of irradiation. PDT is regarded as a promising treatment strategy for certain types of cancers and skin conditions⁹¹ because it is less invasive than surgical removal,⁹² has fewer side effects than radiation or chemotherapy,^{93,94} and can even stimulate an antitumor immune response.^{95,96}

Several photosensitizers (PS), most of which belong to the porphyrinoid family of macrocyclic tetrapyrroles, have been approved for use in PDT.^{97,98} However,

widespread clinical use of PDT has been hindered because these compounds lack photophysical and pharmacological attributes desired in an optimal PS. An ideal PS would be simple to synthesize and purify, demonstrate strong absorption of 600-850 nm light, which can penetrate deeper into tissues than other wavelengths of light,³⁴ and generate $^1\text{O}_2$ with a high quantum yield during irradiation. It is also critical that a PS for PDT is nontoxic in the absence of light to minimize off-target side effects. Lastly, water solubility is critical to ensure stability during storage or intravenous injection and to prevent aggregation-induced attenuation of the $^1\text{O}_2$ quantum yield. To meet this need for improved PSs, Dr. Rosenthal's group at the University of Delaware developed a linear tetrapyrrole metal complex palladium 10,10-dimethyl-5,15-bis(pentafluorophenyl)biladiene (Pd[DMBi1], Figure 3.1B) that is capable of sensitizing $^1\text{O}_2$ with a high quantum yield comparable to those of PSs currently used in PDT.⁹⁹ Importantly, Pd[DMBi1] is easily synthesized from commercially available starting materials, and it efficiently absorbs up to $\lambda = 550$ nm. However, early experiments showed that this molecule is insoluble in aqueous solutions, which is a requirement to use this PS for PDT. To improve upon the solubility and cytocompatibility of Pd[DMBi1], our collaborators modified the complex with a PEG functional group to produce Pd[DMBi1]-PEG₇₅₀ to overcome the hydrophobicity of the original compound. The addition of PEG substituents is commonly employed in the development of cancer therapeutics due to its biocompatibility and ability to readily dissolve in water.^{100,101} In this Chapter, we investigated the photophysical properties of Pd[DMBi1]-PEG₇₅₀ and we assessed its' use to mediate PDT in TNBC cells. Additionally, we evaluated the ability to provide simultaneous PDT and PTT of

TNBC cells with Pd[DMBil1]-PEG₇₅₀ and PEG-NS as a strategy to overcome the limitations each individual therapy as discussed below.

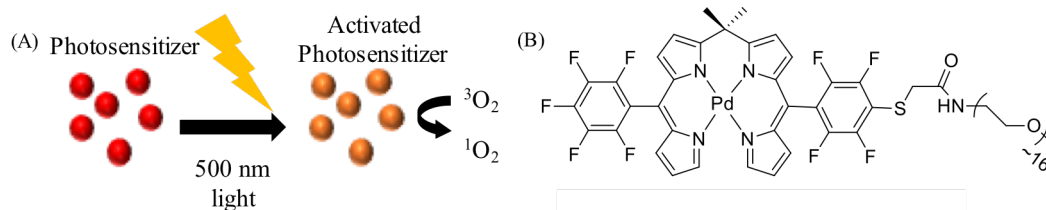


Figure 3.1: Schematics of photodynamic therapy. (A) Schematic showing production of singlet oxygen upon exposure to light. (B) Chemical structure of Pd[DMBil1]-PEG₇₅₀.

3.1.2 Nanoshell-Mediated Photothermal Therapy and the Importance of Inducing Apoptosis as the Mechanism of Cell Death

The first clinical application of NSs was for PTT, and to date NS-mediated PTT has been investigated in clinical trials for lung, head and neck, and prostate cancers.^{45-47,102} The initial results of these clinical trials have shown that NSs are highly biocompatible and safe for intravenous injection in humans.^{45,46} Importantly, NSs used in preclinical animal studies and in human clinical trials are always coated with mPEG-SH to produce “pegylated NSs” (PEG-NS, Figure 3.2A) because it extends circulation time, enhances stability, and improves biocompatibility of the NSs. Long term *in vivo* studies have shown that PEG-NS remain in some organs, particularly the liver, for extended periods of time, but this is not correlated with any adverse events.¹⁰³ As described in Chapters 1 and 2, the NSs used in this chapter and throughout this thesis are composed of 120 nm silica cores and 15 nm thick gold shells because they maximally absorb ~800 nm light, and NSs of this size display high photothermal conversion efficiency.

A main limitation of PTT is that high NS doses and laser powers typically lead to cellular necrosis, which has recently been correlated with local inflammation and disease recurrence.^{104,105} It would be more desirable to induce apoptosis, which does not have these detrimental outcomes. It is therefore important to understand the kinetics and mechanisms of cell death induced by PTT under different laser exposure conditions and NP doses to maximize therapeutic efficacy and to minimize the potential for undesirable side effects.¹⁰⁴ Towards this goal, researchers have recently begun investigating the fundamental cellular responses to PTT.¹⁰⁵ PTT that causes necrosis typically involves the loss of cellular plasma membrane integrity and the subsequent release of intracellular contents including damage-associated molecular patterns (DAMPs) into the extracellular milieu.¹⁰⁶ This abnormal release can trigger detrimental inflammatory and immunogenic responses, making necrosis an undesirable pathway for cell death. By comparison, cell membrane integrity is maintained during apoptosis, and “eat me” signals like phosphatidylserine (PS) relocate to the extracellular portion of the membrane to mark the cell for phagocytosis. Upon encountering phagocytes, apoptotic cells become transformed in a way that discourages inflammation, a distinct and more appealing outcome than that which occurs during necrosis (Figure 3.2B).^{104,106} However, if phagocytes do not rapidly clear an apoptotic cell, it can also experience loss of membrane integrity and release its intracellular contents, including DAMPs, in a process known as secondary necrosis.¹⁰⁶ In an effort to enable PTT-mediated apoptotic cell death by utilizing low NS dosages and laser powers without hindering overall therapeutic efficacy, we evaluated a powerful combination treatment strategy that utilizes PEG-NS and Pd[DMBi1]-PEG₇₅₀ to induce low-dose PTT and PDT, respectively, in an effort to induce primarily

apoptosis, rather than necrosis, by both mechanisms of treatment.

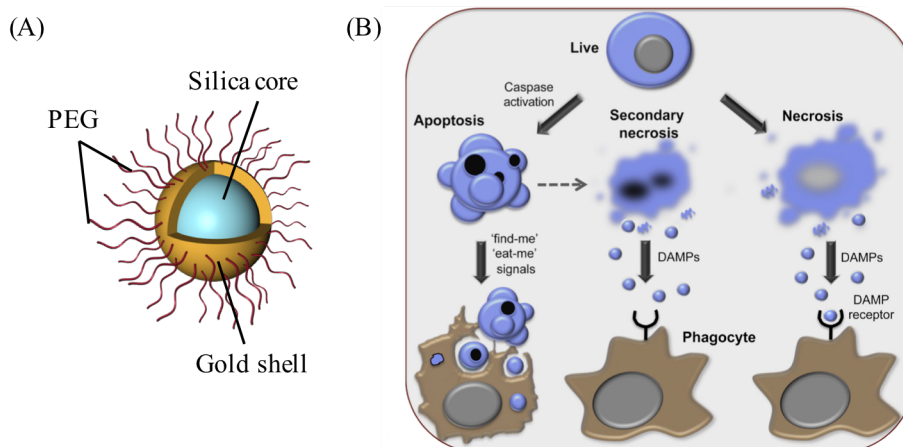


Figure 3.2: Schematic of PEG-NS and the mechanisms of cell death. (A) Schematic of PEG-NS. (B) Schematic showing the apoptotic and necrotic mechanisms of cell death following PTT. A cell undergoing apoptosis maintains its membrane integrity and produces “eat me” signals to mark the cell for phagocytosis without incurring inflammation. Apoptosis may lead to secondary necrosis in which the cell experiences loss of membrane integrity and release of damage-associated molecular patterns (DAMPs), but without activating phagocytosis. Conversely, primary necrosis destroys plasma membrane integrity to cause the release of DAMPs, leading to an inflammatory response. Image adapted from *Melamed, et al., ACS Nano, 2015*.

3.1.3 Combining Photothermal and Photodynamic Therapies for Multimodal Cancer Treatment

Our overarching hypothesis was that combining the two light-based therapies (PTT and PDT) could overcome the limitations of each as standalone therapies (Figure 3.3). For PDT, there are three major limitations we aimed to address. First, PSs often have high toxicity to healthy tissues even without light application, which limits the dosages that can be administered.¹⁰⁷ To address this, in the first part of this Chapter we evaluated the dose-related toxicities of Pd[DMBil1]-PEG₇₅₀ to TNBC cells both in the absence and presence of light, and we calculated the resulting phototoxicity

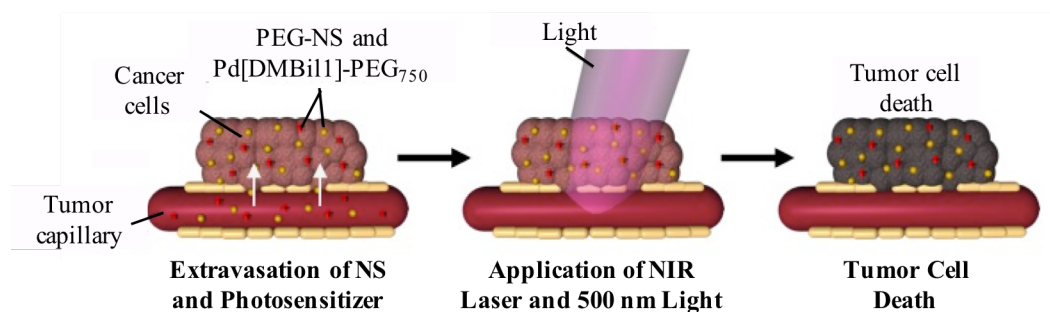


Figure 3.3: Dual photodynamic/photothermal therapy. Schematic showing the therapy regimen for our dual PDT/PTT strategy to treat cancer.

index. We then compared this phototoxicity index to that of commercially available PSs currently used for cancer treatment in order to demonstrate the benefits of this novel molecule as a mediator of PDT. The second limitation faced by PDT is that it requires sufficient oxygen in the native tissue to produce toxic $^1\text{O}_2$. However, the microenvironment deep within solid tumors is often hypoxic, thereby rendering the PSs and PDT ineffective in these regions.¹⁰⁷ Combining PDT with PTT could overcome this limitation because PTT is effective anywhere within tumors as long as sufficient amounts of NSs are present to produce heat, and it does not depend on the oxygenation level of the tumor. Lastly, PSs for PDT are often activated by low wavelengths of light (<600 nm) that may not penetrate across the entire depth of a tumor, resulting in uneven therapeutic effects.^{94,107} To improve upon this, some researchers are developing PSs that can be activated with longer near-infrared (NIR) wavelengths of light that can penetrate the entire tumor volume.^{108–110} Our approach is to combine PDT with PTT mediated by NIR-absorbing NSs so that therapeutic $^1\text{O}_2$ or heat is distributed throughout the entire tumor space.

Likewise, there is a key challenge for PTT that may be addressed by combining it with PDT. As mentioned above, high dose PTT is often used to ablate

tumors via necrotic cell death, but this is not ideal for long-term cancer remission. Low dose PTT can trigger apoptotic cell death, and we hypothesized that combining low dose PTT with PDT would enable effective cancer treatment via apoptosis, while offering the high specificity afforded by both treatment types while also decreasing potential for off-target effects to healthy tissues.

Given the potential benefits of combining PDT with PTT, many researchers have begun to investigate this dual treatment approach.^{108,109} Usually, NIR-absorbing NPs are used as carriers for PSs tethered to their surfaces, which allows these conjugates to be used to mediate both PDT and PTT.^{110,111} Alternatively, our approach is to induce dual PDT/PTT with two separate entities mixed together, but not physically attached to each other, with the benefit that both can distribute throughout the tumor independently to mediate each therapy, increasing the likelihood that all regions of the tumor would receive PDT and/or PTT. Further, in this technique, the timing and output powers of each light source can be easily controlled for maximal therapeutic outcomes. Due to these benefits, we hypothesized that dual PDT/PTT mediated through Pd[DMBil1]-PEG₇₅₀ and PEG-NS, respectively, would be more effective against cancer than either therapy alone. To test these hypotheses, in the second part of this Chapter we evaluated the use of Pd[DMBil1]-PEG₇₅₀ in combination with NSs for dual PDT/PTT therapy of TNBC cells.

3.2 Materials and Methods

3.2.1 Nanoshell Functionalization and Characterization

NSs were synthesized and functionalized with 5 kDa mPEG-SH (PEG-NS) as described in Chapter 2. After functionalization, PEG-NS were purified by

centrifugation and stored in ultrapure water at 4°C until use. PEG-NS diluted to 5.47E9 NS/mL in complete cell culture media (with or without 10 μ M Pd[DMBi1]-PEG₇₅₀) were characterized using UV-vis and DLS.

3.2.2 Synthesis and Characterization of PS

Pd[DMBi1] was synthesized according to published protocols from our collaborators.^{99,112,113} PEGylation of the parental Pd[DMBi1] molecule was facilitated by its *meso* pentafluorophenyl groups. Treatment of Pd[DMBi1] with mercaptoacetic acid and triethylamine in 90 °C DMF for 1 hr afforded a mixture of unreacted starting material, monomercaptoacetic acid-substituted product (Pd[MMDMBi1]) and dimercaptoacetic acid-substituted side product. The three components were separated by column chromatography, and PEGylation of Pd[MMDMBi1] was achieved through conversion of the mercaptoacetic acid substituent into an *N*-(methoxyPEG)mercaptoacetamide using carbodiimide coupling chemistry.^{1,2} Pd[MMDMBi1] was initially reacted with *N*-hydroxysuccinimide (NHS) and 1-ethyl-3-(3'-dimethylaminopropyl)carbodiimide hydrochloride (EDC) to form an NHS mercaptoacetate intermediate. Further treatment with triethylamine and a methoxy-PEG-amine with an average molecular weight of 750 Da resulted in the formation of Pd[DMBi1]-PEG₇₅₀ (Figure 3.1B).

The ¹H NMR, ¹³C NMR, and ¹⁹F NMR spectra of Pd[DMBi1]-PEG₇₅₀ were measured at 25°C on a Bruker 600 MHz spectrometer with a 5-mm Bruker SMART probe. Proton spectra are referenced to the residual proton resonance of the deuterated solvent (CDCl₃ = δ 7.26) and carbon spectra are referenced to the carbon resonances of the solvent (CDCl₃ = δ 77.16).¹¹⁴ Fluorine spectra are referenced to an external trifluoroacetic acid standard (TFA = δ -76.55 in CD₃CN).¹¹⁵ Chemical shifts are

reported using the standard δ notation in parts-per-million. High-resolution mass spectrometry analysis was performed at the Mass Spectrometry Laboratory in the Department of Chemistry and Biochemistry at the University of Delaware. Liquid injection field desorption ionization mass spectrometry was carried out using a Waters GCT Premier high-resolution time of flight mass spectrometer. Electrospray ionization mass spectrometry was conducted with a Thermo Q-Extractive Orbitrap high-resolution mass spectrometer.

All UV-vis absorbance spectra were measured using a StellarNet CCD array UV-vis spectrometer. Samples were prepared in quartz cuvettes (6Q) that had a 1.0 cm pathlength and were manufactured by Firefly Scientific. Absorption spectra were collected for solutions of Pd[DMBil1]-PEG₇₅₀ in room temperature methanol or PBS at concentrations of 4.0, 8.0, 12.0, 16.0, 20.0, and 24.0 μM .

3.2.3 Photodegradation of Pd[DMBil1]-PEG₇₅₀

Pd[DMBil1]-PEG₇₅₀ was diluted to 24 μM in PBS and placed into a quartz cuvette (6Q, path length = 1.0 cm) fused to a graded quartz to pyrex tube. The solution was stirred for 2 hr at room temperature during irradiation with light from a 150 Watt halogen lamp (Nikon, Inc., Model MKII) fitted with a 10 nm FWHM bandpass filter centered at 550 nm (Thor Labs, FB550-10). The absorption spectrum was recorded every minute over a 2 hr period.

3.2.4 Singlet Oxygen Production from Pd[DMBil1]-PEG₇₅₀

Data was collected using a automated Photon Technology International (PTI) QuantaMaster 40 fluorometer setup. All $^1\text{O}_2$ experiments were conducted in 1.0 cm

path length quartz cuvettes (6Q) from Firefly Scientific. $^1\text{O}_2$ quantum yields were calculated using the following equation:

$$\Phi_s = \Phi_{ref} \left(\frac{m_s}{m_{ref}} \right) \left(\frac{\epsilon_{ref}}{\epsilon_s} \right)$$

Where Φ_s and Φ_{ref} are the $^1\text{O}_2$ quantum yields for the sample and a reference standard, respectively, m_s and m_{ref} are the rates of consumption of a singlet oxygen trapping compound in the presence of the sample and standard respectively, and ϵ_s and ϵ_{ref} are the extinction coefficients of the sample and standard at the wavelength of irradiation. Reported $^1\text{O}_2$ quantum yields are averages obtained from three trials.

Singlet oxygen production in PBS was measured by monitoring the enhancement in fluorescence resulting from the reaction of the fluorescent probe Singlet Oxygen Sensor Green (SOSG) with $^1\text{O}_2$ with methylene blue as the standard ($\Phi_{ref} = 0.52$).^{116,117} 100 μg of SOSG was dissolved in 33 μL of methanol, and ultrapure water was added to make the 0.25 mM stock solution. The SOSG stock solution was added to samples to a final concentration of 2.5 μM SSOG and 0.05% methanol by volume. $^1\text{O}_2$ production was assessed following 0, 30, 60, 90, and 120 sec irradiation times with light from a 150 Watt halogen lamp (Nikon, Inc., Model MKII). Emission spectra of SOSG were obtained by exciting at $\lambda_{ex} = 480$ nm and scanning from $\lambda_{em} = 500 - 650$ nm using a step size of 1 nm and an integration time of 0.25 sec. Controls and samples without light treatment were used as controls to assess changes in SOSG emission. The change in integrated emission intensity of each cuvette was plotted as a function of irradiation time, and linear regression lines were fit to the data. The slopes of the regression lines from the dark controls were subtracted from the slopes of the

regression lines from the cuvettes exposed to 550 nm light to give values of m_s and m_{ref} used with the equation above to calculate Φ_s .

3.2.5 Temperature and 1O_2 Production During PDT and PTT

Solutions of PEG-NS (5.47E9 NS/mL) and/or Pd[DMBil1]-PEG₇₅₀ (4 μ M) were diluted in ultrapure water and placed into black-walled 96-well plates for 1O_2 analysis or into 24-well plates for temperature analysis. For 1O_2 detection, 10 μ L of the 0.25 mM stock solution of SOSG was added to 90 μ L of sample. The plates were irradiated with a LightPad 930 (Artograph) with a long pass $\lambda = 525$ nm filter (>500 nm light) for 10 min and then SOSG fluorescence was read on a Synergy H1 plate reader as described above. The irradiations were repeated four times to generate singlet oxygen production curves. For temperature analysis, samples were irradiated for 2 min with the continuous wave B&W Tek 808 nm laser with a 1 W/cm² power density and/or >500 nm light for 10 min. Temperature measurements were recorded using a FLIR A5 thermal camera.

3.2.6 Cell Culture

MDA-MB-231 TNBC cells were purchased from American Type Culture Collection (ATCC) and cultured in Dulbecco's Modified Eagle Medium (DMEM) supplemented with 10% fetal bovine serum and 1% penicillin-streptomycin. Cells were cultured in T75 cell culture flasks and incubated at 37°C in a 5% CO₂ humidified environment. Cells were passaged between flasks or into sample plates by detaching the cells from the flasks with Trypsin-EDTA, diluting the cells with complete medium, and counting the cells with a hemocytometer before transferring to a new flask or well plate.

3.2.7 Cellular Uptake of Pd[DMBil1]-PEG₇₅₀ and Nanoshells

For flow cytometry experiments to analyze cellular uptake of Pd[DMBil1]-PEG₇₅₀, MDA-MB-231 cells were plated at 25,000 cells/well in 24-well plates and were incubated overnight. Pd[DMBil1]-PEG₇₅₀ was diluted to 0, 0.5, 1.0, or 1.5 mM in complete cell culture media, which was then added to cells. Well plates were incubated with Pd[DMBil1]-PEG₇₅₀ for 48 hr in the dark and then cells were detached with trypsin-EDTA and transferred to 1.5 mL Eppendorf tubes. The samples were centrifuged to form a cell pellet, the supernatant was removed, and the cells were re-suspended in sterile 1X PBS. Samples were read on a Novocyte flow cytometer (ACEA Biosciences) with the phycoerythrin (PE) filter set (excitation, 488 nm; emission, 572/28 nm) and data analysis was performed in the NovoExpress software. The median fluorescence intensity (MFI) was calculated by averaging the fluorescence median from three experiments of each PS concentration.

To analyze uptake of Pd[DMBil1]-PEG₇₅₀ and PEG-NS by fluorescence or darkfield imaging, cells were plated at 15,000 or 25,000 cells/well, respectively, in a glass bottom 8-well plate with a removable well chamber and incubated overnight. Then, 1 mM Pd[DMBil1]-PEG₇₅₀ and/or 2.7×10^9 PEG-NS/ml diluted in cell culture media was added to cells for 24 hr. Cells were fixed with 4% formaldehyde for 15 min and rinsed 3X with 1X PBS. Cells were stained with DAPI and phalloidin to visualize cell nuclei and F-actin on the cytoskeleton, respectively. Well chambers were removed and slides were mounted with Vectashield mounting media. Cells were imaged with a Zeiss Axioobserver Z1 Inverted Fluorescent Microscope using the FITC (F-actin), DsRed (PS), and DAPI (nuclei) fluorescence channels and a darkfield condenser.

3.2.8 Analysis of the Mechanisms of Cell Death Induced by PTT and/or PDT

MDA-MB-231 cells were plated at 10,000 cells/well in black-walled 96-well plates and incubated overnight. For PDT only experiments, cells were treated with 0, 4, 6, or 8 μM Pd[DMBil1]-PEG₇₅₀ diluted in complete cell culture media for 24 hr in the dark. Then, cells were irradiated with the light plate (>500 nm light) for 0 or 30 min. For dual PDT/PTT experiments, cells were treated with 0 or 4 μM PS and/or NSs diluted to 0 or 5.47E9 NS/mL overnight and were then irradiated for 20 min with the light plate or for 2 min/well with the 808 nm laser at 1 (for PDT only) or 0.85 (for dual PTT/PDT experiments) W/cm^2 . After incubating cells for 1 hr, an AnnexinV-FITC stain (Cayman Chemicals) was conducted *via* manufacturer instructions. Briefly, cells were lifted with trypsin, washed once with 1X binding buffer (300xg, 5 min), and resuspended in 50 μL binding buffer containing 1:500 AnnexinV-FITC and 1:2000 propidium iodide (PI) stains for 10 min protected from light. Then, samples were diluted with 150 μL 1X binding buffer and run on the flow cytometer with the FITC (excitation, 488 nm; emission, 530/30 nm) and PerCP (excitation, 488 nm; emission, 675/30 nm) channels. Data analysis was performed in the NovoExpress software, and positive stained gates were based off of unstained cells. Single stained controls were used for compensation. Data shown are averaged amongst amongst three independent experiments and statistical significance was calculated using t-tests to compare cells treated with and without light for each treatment concentration.

3.2.9 Assessment of Cells' Metabolic Activity Following PDT and/or PTT

MDA-MB-231 cells were plated at 10,000 cells/well in black-walled 96-well plates and incubated overnight. Then, cells were treated with Pd[DMBil1]-PEG₇₅₀ at 0-5 mM for dark toxicity assays or 0-10 μM for light exposure experiments to assess

PDT as a standalone therapy. The commercial PS agents isohematoporphyrin (IHP) or hematoporphyrin dihydrochloride (HPDC) were used for comparison of therapeutic effect. The IHP or HPDC were diluted to 0-3 mM or 0-700 μ M for dark toxicity or light exposure experiments, respectively. All solutions of PSs were prepared by diluting the dried compounds in complete cell culture media. To evaluate the inherent PS toxicity in the dark, well plates were covered with aluminum foil to avoid light contamination and were incubated for 48 hr prior to Alamar blue metabolic activity assays. In the PDT experiments with light irradiation, plates were covered with aluminum foil and were incubated for 0 or 24 hr prior to light exposure. 96-well plates were placed onto a LightPad 930 (Artograph) with a long pass ($\lambda = 525$ nm) filter for 0, 10, 20, or 30 min. After light treatment, the PS-containing cell culture media was replaced with fresh media.

For dual PDT/PTT experiments, cells were treated with 0 or 0.25 μ M Pd[DMBil1]-PEG₇₅₀ and/or PEG-NS diluted to 0 or 5.47E9 NS/mL overnight and were then irradiated for 20 min with the light plate and/or 2 min/well with the 808 nm laser. After overnight incubation, the media was removed and the Alamar blue viability reagent (diluted 1:10 in cell culture media) was added per manufacturer recommendations. Samples fluorescence was measured on a Hybrid Synergy H1 plate reader with excitation and emission wavelengths of 560 nm and 590 nm, respectively. To analyze the data, background (Alamar blue reagent without cells) was subtracted from each well. Then, wells were averaged and normalized to untreated cells. Data shown is from at least three experiments that were each run with triplicate wells. Synergism based on light source was calculated using a coefficient of drug interaction from cells treated with Pd[DMBil1]-PEG₇₅₀ and PEG-NS and each light source

according to the equation $CDI = \frac{AB}{(A \times B)}$. In this equation, AB is the viability of cells treated with both light sources, and A and B are cell viability following treatment with only 808 nm or >500 nm light. The PDT/PTT experimental data with Pd[DMBil1]-PEG₇₅₀ and NSs was analyzed by 1-way ANOVA (based on light source) with post hoc Tukey-Kramer, and the IHP and HPDC data was analyzed by 1-way ANOVA with post hoc Tukey. Phototoxicity indexes were calculated by dividing the lethal dose for 50% cell viability (LD50) by the effective dose for 50% cell viability (ED50).

3.3 Results

3.3.1 Characterization and Singlet Oxygen Production of Pd[DMBil1]-PEG₇₅₀

The visible absorption profile of Pd[DMBil1]-PEG₇₅₀ consists of three features centered at 402, 483 and 540 nm in methanol (Figure 3.4A), which is nearly identical to that of the parental Pd[DMBil1] molecule. Although this absorbance spectrum shifts slightly to longer wavelengths in an aqueous PBS solution, the molecule obeys the Beer-Lambert Law between 4-24 μ M, indicating minimal aggregation. Further, Pd[DMBil1]-PEG₇₅₀ is highly resistant to photodegradation, as the absorption spectrum does not change over 2 hr irradiations with either 500 or 550 nm light (Figure 3.4B).

Singlet oxygen production from Pd[DMBil1]-PEG₇₅₀ in aqueous solutions was investigated using singlet oxygen sensor green (SOSG) as a ¹O₂ probe with methylene

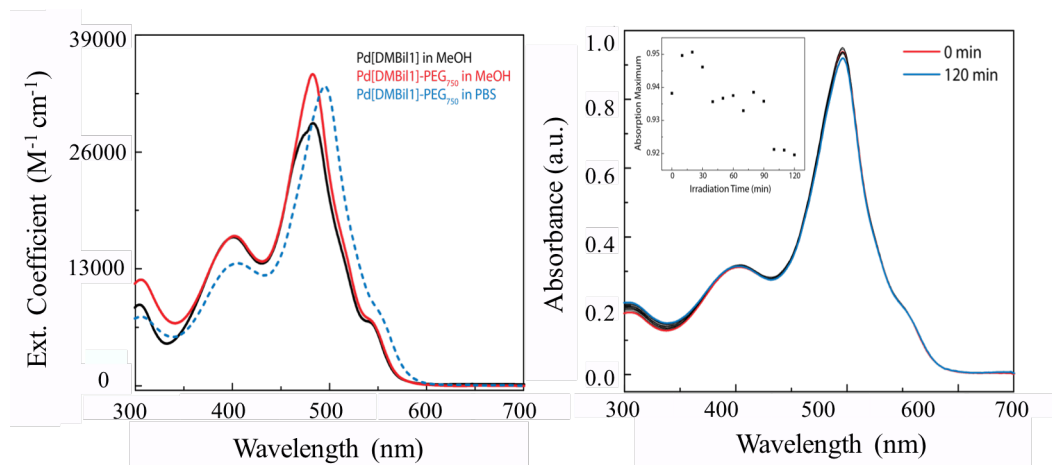


Figure 3.4: Absorbance spectrum of the photosensitizers. (A) Electronic absorption spectra of Pd[DMBil1] in methanol (black line), Pd[DMBil1]-PEG₇₅₀ in methanol (red line), and Pd[DMBil1]-PEG₇₅₀ in pH 7.4 PBS (dotted blue line). (B) UV-vis absorption profile of a 24 μ M solution of Pd[DMBil1]-PEG₇₅₀ in PBS during irradiation with 550 nm light for 2 hr.

blue as a standard curve. Samples were irradiated with 550 nm light, and SOSG sample fluorescence was measured to obtain a ¹O₂ quantum yield of $\Phi_{\Delta} \approx 0.23$. We anticipated that this level of singlet oxygen production is sufficient for use in PDT, so we investigated this PS for PDT to treat TNBC cells.

3.3.2 PEG-NS and Pd[DMBil1]-PEG₇₅₀ are Stable in Cell Culture Media

The stability of PEG-NS in complete cell culture media was examined by diluted them to a final concentration of $\sim 5.5 \times 10^9$ NS/ml in media and measuring the extinction spectrum immediately and again following a 24 hr incubation period at 37°C. The extinction spectrum was nearly identical before and after this incubation period, indicating that the PEG-NS are stable and not aggregating in this solution (Figure 3.5A). Next, we investigated the stability of PEG-NS and Pd-DMBil1]-PEG₇₅₀

combined in cell culture media. UV-vis absorbance measurements showed that the characteristic peaks of both the PS and PEG-NS were present before and after incubating the solutions in media at 37°C for 24 hr, indicating that both agents remain

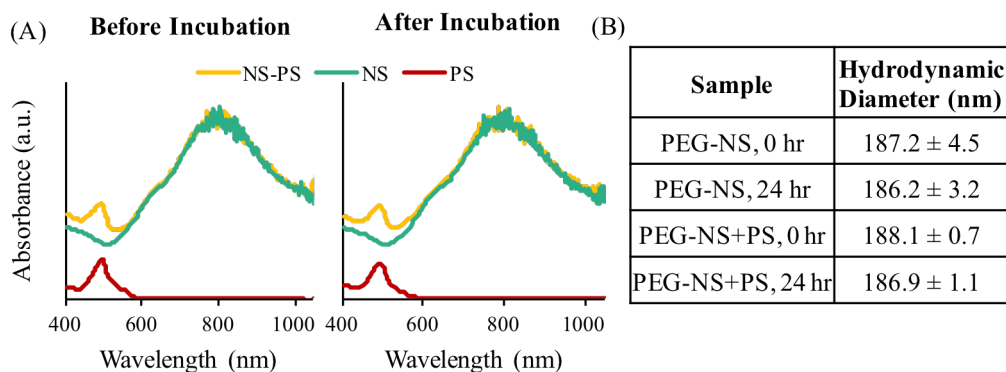


Figure 3.5: Characterization of solutions of PEG-NS and photosensitizer. (A) Electronic absorption spectra of PEG-NS and/or Pd[DMBil1]-PEG₇₅₀ in cell culture media before (left) and after a 24 hr incubation (right). (B) DLS measurements showing hydrodynamic diameter of PEG-NS with or without Pd[DMBil1]-PEG₇₅₀ in cell culture media before and after a 24 hr incubation.

separated and stable in solution (Figure 3.5A). Hydrodynamic diameter measurements of PEG-NS and the combined solutions before and after incubation further confirmed that both agents remained separate entities during incubation, as there is no size difference between PEG-NS with and without the PS (Figure 3.5B).

3.3.3 PEG-NS and Pd[DMBil1]-PEG₇₅₀ Produce Heat and ¹O₂ when Combined

To evaluate the PDT and PTT efficiencies of our agents, we irradiated solutions of Pd[DMBil1]-PEG₇₅₀ (4 μM) and/or PEG-NS (5.5X10⁹ NS/mL) with >500 nm light or the 808 nm laser and evaluated both the temperature and singlet oxygen production under each irradiation condition. For singlet oxygen measurements, each irradiation was repeated 4 times to generate curves showing increasing amounts of singlet oxygen from each repetition (Figure 3.6A). These data demonstrate that only

the combination of >500 nm light and the PS can result in PDT-mediated cell death. Alternatively, the results from 808 nm irradiations show that temperature increases are due to PEG-NS, as no temperature increases are observed from solutions containing only Pd[DMBil1]-PEG₇₅₀ (Figure 3.6B). Further, no temperature increases were observed for samples irradiated with the light box, demonstrating that temperature effects are only a result of PEG-NS combined with the 808 nm CW laser. Finally, no ¹O₂ was produced from 808 nm laser irradiations, indicating that any effect of PDT is purely resulting from PS exposure to the >500 nm lightbox. Together, these results indicate that both Pd[DMBil1]-PEG₇₅₀ and PEG-NS mixed together into one solution

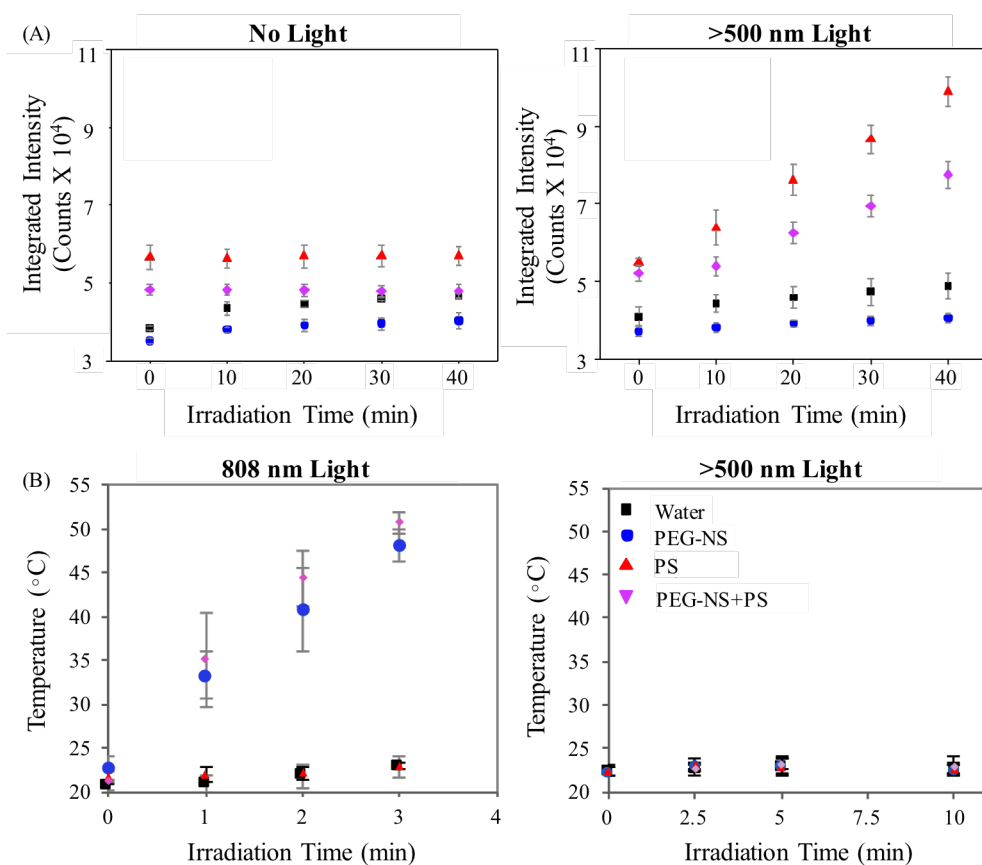


Figure 3.6: Temperature and singlet oxygen measurements. (A) Integrated intensity of fluorescence measurements from the singlet oxygen sensor green (SOSG) reagent in solution with water, PEG-NS, Pd[DMBil1]-PEG₇₅₀, or both, and irradiated with no light (left) or 550 nm light in 10 min increments (right). Irradiations were repeated 4 times and fluorescence was measured after each irradiation. (B) Temperature measurements during irradiation of water, PEG-NS, Pd[DMBil1]-PEG₇₅₀, or both with 808 nm light. Samples were irradiated for 2 min, and this was repeated four times. 52

retain their individual abilities to mediate PDT or PTT, respectively. Importantly, the temperature increases and $^1\text{O}_2$ production generated from the mixture of both agents was similar to each individual agent alone, indicating that any cell death from PDT is from the PS and >500 nm light, any PTT effect is mediated from PEG-NS and 808 nm light, and the combination of these two agents does not reduce their individual effect.

3.3.4 Pd[DMBil1]-PEG₇₅₀ and PEG-NS are Taken Up by TNBC Cells

Next, we examined cellular uptake of Pd[DMBil1]-PEG₇₅₀ and PEG-NS in TNBC cells. First, MDA-MB-231 cells were treated with 0-1.5 mM Pd[DMBil1]-PEG₇₅₀ for 48 hr and the cellular fluorescence was analyzed by flow cytometry, which revealed that cells treated with Pd[DMBil1]-PEG₇₅₀ experienced a 2-fold increase in median fluorescence intensity (MFI) compared to untreated cells (Figure 3.7A). To visualize cellular uptake of PEG-NS and Pd[DMBil1]-PEG₇₅₀, cells were treated with 1 mM Pd[DMBil1]-PEG₇₅₀ and/or 2.7E9 PEG-NS/mL for 24 hr, fixed, and cytoskeletons were stained with Phalloidan. Fluorescence imaging confirmed that Pd[DMBil1]-PEG₇₅₀ is taken up by cells during the incubation period, as indicated by the red fluorescent signal, and darkfield microscopy revealed that PEG-NS (gold signal) are present on cells as well (Figure 3.7B). These results were encouraging given that both agents need to be in close proximity or taken up by cells to be effective for PTT and PDT, leading us to investigate their use for individual and dual therapies. To do this, we first evaluated the safety and efficacy our novel PS to induce PDT of TNBC cells before evaluating the combination treatment strategy.

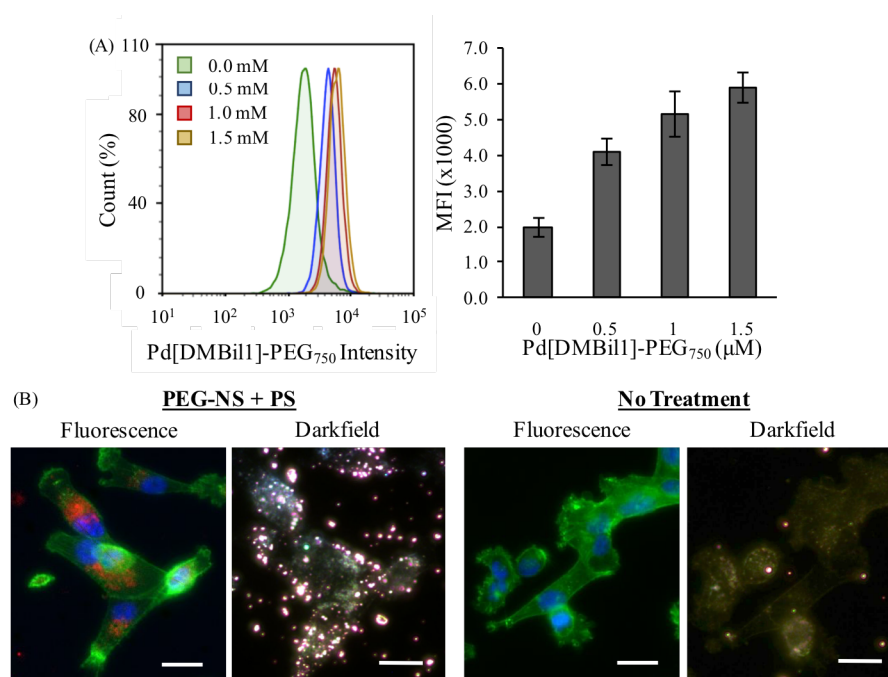


Figure 3.7: Cell uptake of PEG-NS and photosensitizer. (A) Histogram and normalized median fluorescence intensity (MFI) showing Pd[DMBil1]-PEG₇₅₀ intensity by flow cytometry following treatment of MDA-MB-231 cells with Pd[DMBil1]-PEG₇₅₀ for 48 hr. (B) Fluorescence images showing Pd[DMBil1]-PEG₇₅₀ uptake by MDA-MB-231 cells following a 24-hr incubation. Nuclei are stained blue (DAPI), F-actin in the cytoskeleton is stained green (phalloidan), and Pd[DMBil1]-PEG₇₅₀ appears red. Scale=25 μ m.

3.3.5 Pd[DMBil1]-PEG₇₅₀ is Minimally Toxic to TNBC Cells in the Dark

First, we evaluated the ability for Pd[DMBil1]-PEG₇₅₀ to mediate PDT as a standalone therapy. Since a common limitation to the clinical application of PDT is the inherent toxicity of PSSs, we first evaluated the safety of Pd[DMBil1]-PEG₇₅₀ without light. To evaluate the toxicity of Pd[DMBil1]-PEG₇₅₀, we treated TNBC MDA-MB-231 cells with 0-5 mM Pd[DMBil1]-PEG₇₅₀ for 48 hr in the dark and then conducted an Alamar blue cell viability assay. MDA-MB-231 cells were completely viable at Pd[DMBil1]-PEG₇₅₀ concentrations up to 0.5 mM (Figure 3.8A). Further, the lethal dose required for 50% cell death (LD₅₀) was 1.87 mM.

To demonstrate the safety profile of Pd[DMBil1]-PEG₇₅₀ and to facilitate a comparison with commercially available PSs, we evaluated cell viability following treatment with 0-3 mM of the two commercial PSs, HPDC and IHP. This revealed LD₅₀ values of 1.22 and 0.64 mM, respectively, both of which are lower than the LD₅₀ obtained with Pd[DMBil1]-PEG₇₅₀ (Figure 3.8B). These results demonstrate that Pd[DMBil1]-PEG₇₅₀ is substantially less toxic than two commercially available PSs suggesting that it may enable successful PDT without causing off-target side effects that often limit the allowable administered dosages.

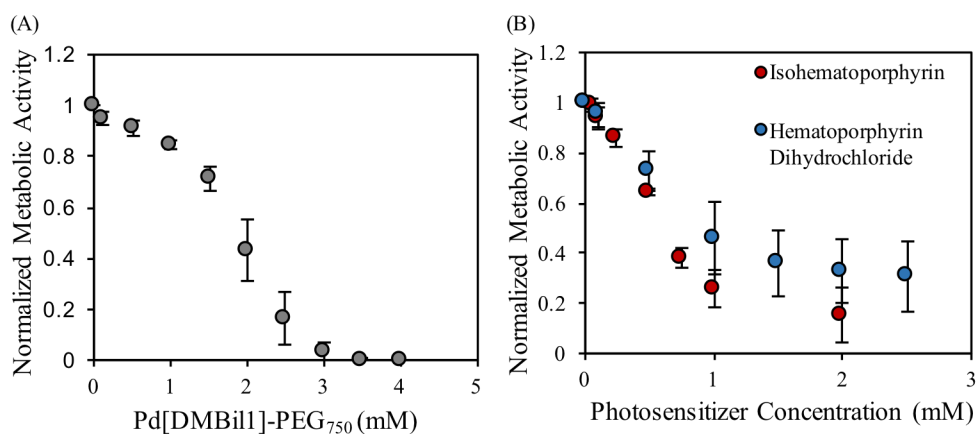


Figure 3.8: Photosensitizer toxicity. Normalized metabolic activity after incubation with varying concentrations of (A) Pd[DMBil1]-PEG₇₅₀ or (B) isohematoporphyrin (red) or hematoporphyrin dihydrochloride (blue), two commercial photosensitizers used for PDT in the dark. Cells were treated with each photosensitizer for 48 hr protected from light prior to adding the viability reagent.

3.3.6 The Phototoxicity Index of Pd[DMBil1]-PEG₇₅₀ is Substantially Higher than Commercial Photosensitizers

To investigate the ability of Pd[DMBil1]-PEG₇₅₀ to mediate PDT, MDA-MB-231 TNBC cells were treated with this PS at concentrations ranging from 0-10 μ M for 0 or 24 hr prior to light exposure for 0, 10, 20 or 30 min with $\lambda > 500$ nm light. Then, we conducted viability assays to assess cell death 16 hr post irradiation. Cells

incubated with Pd[DMBil1]-PEG₇₅₀ for 24 hr prior to irradiation were highly susceptible to PDT-mediated cell death compared to cells irradiated immediately after adding Pd[DMBil1]-PEG₇₅₀. More specifically, cells irradiated immediately following the addition of Pd[DMBil1]-PEG₇₅₀ required concentrations of at least 1 μM and 30 min of light exposure before any loss of cell viability was observed (Figure 3.9A). Alternatively, cells incubated with Pd[DMBil1]-PEG₇₅₀ for 24 hr prior to light application were susceptible to PDT with concentrations of PS as low as 0.25 μM , and 10 μM treatment resulted in complete loss of viability (Figure 3.9B). This enhancement in photo-induced toxicity in cells incubated with the PS before light treatment provides further evidence of cellular uptake of Pd[DMBil1]-PEG₇₅₀. From these results, we also determined that the effective dose of Pd[DMBil1]-PEG₇₅₀ required to reduce cell viability by 50% (ED_{50}) was 0.354 μM for cells incubated with the PS for 24 hr and then subjected to 30 min irradiation. Division of the LD_{50} by the ED_{50} gives the phototoxicity index as a measure of how effective a compound is with light compared to its inherent toxicity in the absence of light. Accordingly, these data demonstrate that Pd[DMBil1]-PEG₇₅₀ has a phototoxicity index of approximately 5300.

To compare the this phototoxicity index to that of the commercially available PSs, we conducted the same photodynamic activity experiments with HPDC and IHP. We treated MDA-MB-231 cells with each PS for 24 hr and then irradiated for 30 min, and found that the ED_{50} of HPDC was 48.65 μM and the ED_{50} of IHP was 327.56 μM (Figure 3.10A,B). The LD_{50} and ED_{50} values for HPDC and IHP resulted in phototoxicity indexes of 25 for HPDC and 1.96 for IHP. By comparison, the

phototoxicity index of Pd[DMBil1]-PEG₇₅₀ is quite impressive as it is approximately 200x and 3000x higher than those of HPDC and IHP, respectively.

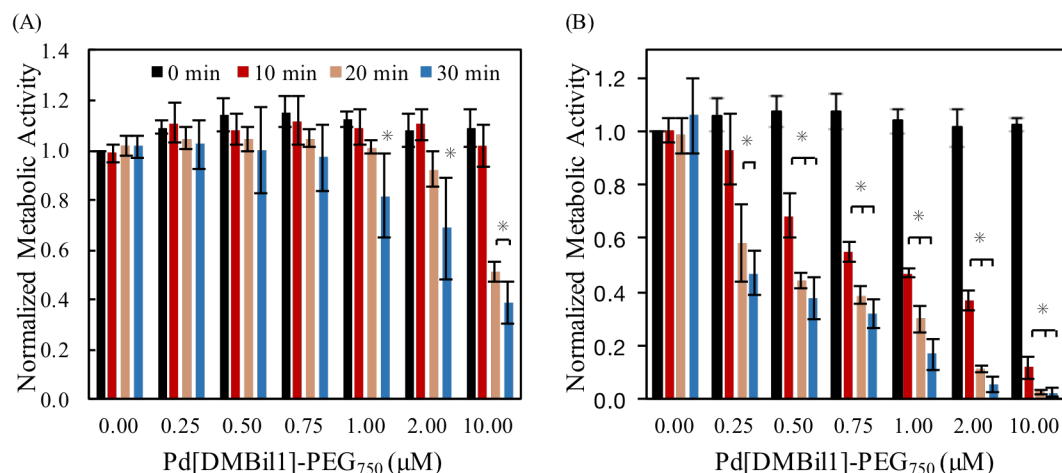


Figure 3.9: Cell viability following PDT. Normalized metabolic activity (A) after adding Pd[DMBil1]-PEG₇₅₀ to cells and immediately exposing cells to light. *p<0.02 by 2-way ANOVA with post hoc Tukey-Kramer compared to 0 min light exposure for each photosensitizer concentration. (B) after incubation with varying concentrations of Pd[DMBil1]-PEG₇₅₀ for 24 hr in the dark followed by light exposure. *p<0.0001 by 2-way ANOVA with post hoc Tukey-Kramer compared to 0 min light exposure for each photosensitizer concentration. Cells were irradiated for 0 (black), 10 (red), 20 (beige), or 30 (blue) min, and the Alamar blue viability reagent was added 16 hr post-irradiation.

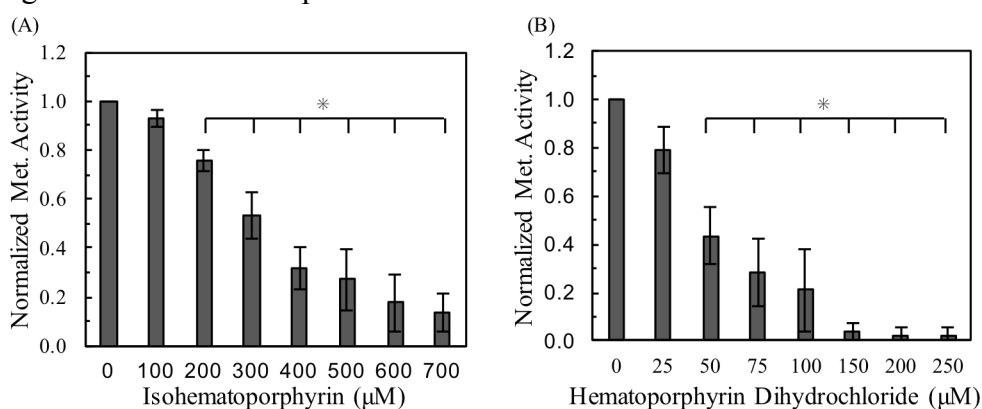


Figure 3.10: Cell viability following PDT with commercial photosensitizers. Normalized cell viability of MDA-MB-231 cells treated with (A) iso-hematoporphyrin and (B) hematoporphyrin dihydrochloride for 24 hr prior to light exposure for 30 min. *p<0.04 by 1-way ANOVA with post hoc Tukey compared to cells treated 0 μM photosensitizer.

3.3.7 PDT Triggers Primarily Apoptotic Cell Death

Since Pd[DMBil1]-PEG₇₅₀ is highly effective for inducing cell death *via* PDT, we next evaluated the mechanism of cell death that results from this therapy. It is ideal to induce apoptosis rather than necrosis because the latter causes the release of intracellular components that cause local inflammation and can stimulate further tumor growth if the cancer cells are not completely eradicated.¹¹⁸ Alternatively, apoptosis is anti-inflammatory and therefore discourages disease progression.¹⁰⁴ To assess the mechanism of cell death, we treated MDA-MB-231 cells with 0-8 μ M Pd[DMBil1]-PEG₇₅₀ for 24 hr, irradiated for 30 min and then incubated the cells for 1 hr prior to AnnexinV (FITC channel) and PI (PerCP channel) staining. We treated cells with higher PS concentrations than in the viability experiments because we analyzed the cells only 1 hr after light treatment. Although these PS concentrations are higher than required for effective PDT, they are still well below the LD₅₀. In these experiments, each mechanism of cell death appears in distinct quadrants depending on their level of staining. For example, live cells are negative for both FITC and PI (lower left quadrant), apoptotic cells stain positive for only FITC (lower right quadrant), late apoptotic cells stain positive for both FITC and PI (upper right quadrant), and necrotic cells stain positive for only PI (upper left quadrant). We found that PDT induces primarily apoptotic cell death, and that the percentage of apoptotic cells increases with higher PS concentrations (Figure 3.11). The maximum amount of positively stained cells resulted from treatment with 8 μ M Pd[DMBil1]-PEG₇₅₀. After averaging three individual experiments, we found that 20.21% of cells were undergoing early apoptosis, 17.08% of cells were undergoing late apoptosis, and 8.17% of cells were experiencing necrosis. Alternatively, cells that did not undergo light treatment experienced only minimal cell death by any mechanism. These results demonstrate

that approximately 82% of the cells killed by this treatment die *via* apoptosis rather than necrosis. Given that apoptosis is much preferred over necrosis for cancer treatment, this makes Pd[DMBil1]-PEG₇₅₀ attractive as a PS for use in PDT.

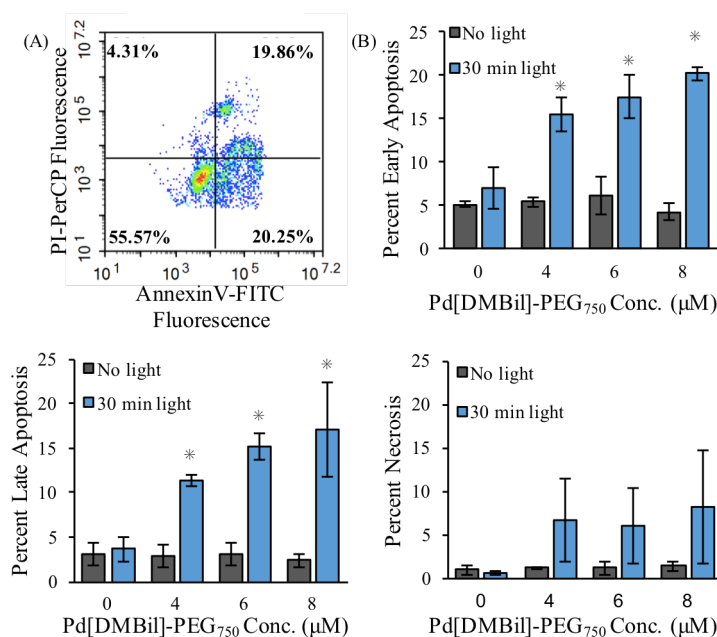


Figure 3.11: Mechanism of cell death from PDT. Apoptosis and necrosis assays after incubation with 0, 4, 6, or 8 μM of Pd[DMBil1]-PEG₇₅₀ for 24 hr, light treatment for 30 min, and incubation for 1 hr. (A) Representative flow cytometry density plot of cells treated with 8 μM Pd[DMBil1]-PEG₇₅₀. (B-D) Flow cytometry analysis of cell populations in early apoptosis, late apoptosis, and necrosis following treatment with the photosensitizer. *p<0.05 by t-tests compared to no light treatment for each concentration.

Overall, these studies demonstrate that Pd[DMBil1]-PEG₇₅₀ is a novel PS with an extremely high phototoxicity index that can mediate PDT of TNBC cells *in vitro*. However, as mentioned earlier, a main limitation of PDT as a standalone therapy to treat solid tumors is that it requires sufficient oxygen in the adjacent tissue to be effective, and solid tumors are characterized by highly hypoxic interiors. This led us to explore the use of Pd[DMBil1]-PEG₇₅₀ as a dual strategy to treat TNBC to have a

more cohesive approach that ablate entire tumors. Further, the light used to activate Pd[DMBi1]-PEG₇₅₀ may not penetrate across an entire tumor. These limitations led us to explore the use of Pd[DMBi1]-PEG₇₅₀ in combination with PEG-NS for dual PDT/PTT of TNBC, which would offer a more complete approach to eliminate entire tumors.

3.3.8 Dual PDT/PTT is a Potent Strategy to Treat TNBC

To evaluate dual PDT/PTT as a strategy to treat TNBC, we treated TNBC cells with Pd[DMBi1]-PEG₇₅₀ (0 or 0.75 μ M) and/or PEG-NS (0 or 5.5E9 NS/mL) for 24 hr. Then, cells were irradiated with the 808 nm laser with 0.75 W/cm² output power for 2 min/well and/or >500 nm light (on the light plate) for 10 min. After overnight incubation, cellular metabolic activity was assessed using an Alamar Blue assay. We found that cells treated with PEG-NS and 808 nm light, as well as cells treated with both agents and only 808 nm light, experienced 11% and 15% decreases in metabolic activity, respectively, compared to cells treated with no light. Additionally, cells treated with Pd[DMBi1]-PEG₇₅₀, or cells treated with both agents, and only >500 nm light, experienced 45% loss in viability. These results demonstrate that PTT and PDT can impact cell viability independently and with minimal cross-over between the two therapies, as cells treated with PEG-NS and >500 nm light, or cells treated with the PS and 808 nm light experienced only minimal loss of cell viability. However, cells co-treated with both the PS and PEG-NS and both light sources experienced a 67% loss of metabolic activity, which is substantially better than either therapy alone (Figure 3.12). To assess if this effect is additive or synergistic, we calculated the CDI as explained in Section 3.2.9. In this equation, a CDI=1 or <1 indicates additive or synergistic effects, respectively. Using cell viability from cells treated with both PEG-

NS and Pd[DMBil1]-PEG₇₅₀ and each mode of irradiation, we calculated a CDI=0.7. This indicates that treating cells with both PDT and PTT has a synergistic effect on cell viability. All together, these results prove that dual PDT/PTT is a viable therapeutic strategy to further explore for solid tumor treatment.

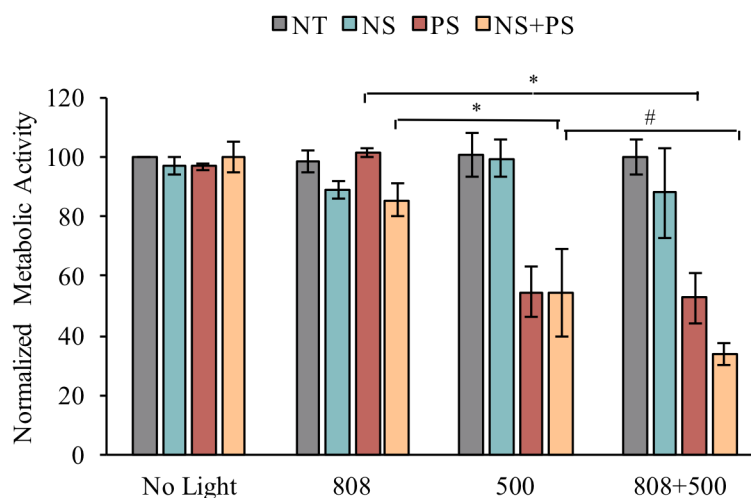


Figure 3.12: Cell viability following dual PDT/PTT. Normalized metabolic activity of MDA-MB-231 cells following treatment with PEG-NS and/or Pd[DMBil1]-PEG₇₅₀ for 24 hr followed by irradiation with 808 nm and/or >500 nm light sources. #p=0.06 and *p<0.05 by 1-way ANOVA with post hoc Tukey-Kramer.

To confirm that dual therapy still primarily induces apoptotic cell death, we conducted Annexin/PI staining following treatment as described earlier. Cells were treated with Pd[DMBil1]-PEG₇₅₀ (0 or 4 μ M) and/or PEG-NS (0 or 5.5E9 NS/mL) for 24 hr, irradiated, and stained after a 1 hr incubation. For these experiments, we treated cells with higher concentrations of PS due to the shorter incubation time before staining compared to the viability experiments. Importantly, these results show that dual PDT/PTT induces primarily apoptotic cell death similar to the PDT only results (Figure 3.13). This validates our hypothesis that low-grade PTT can be used to induce apoptotic cell death when in combination with PDT.

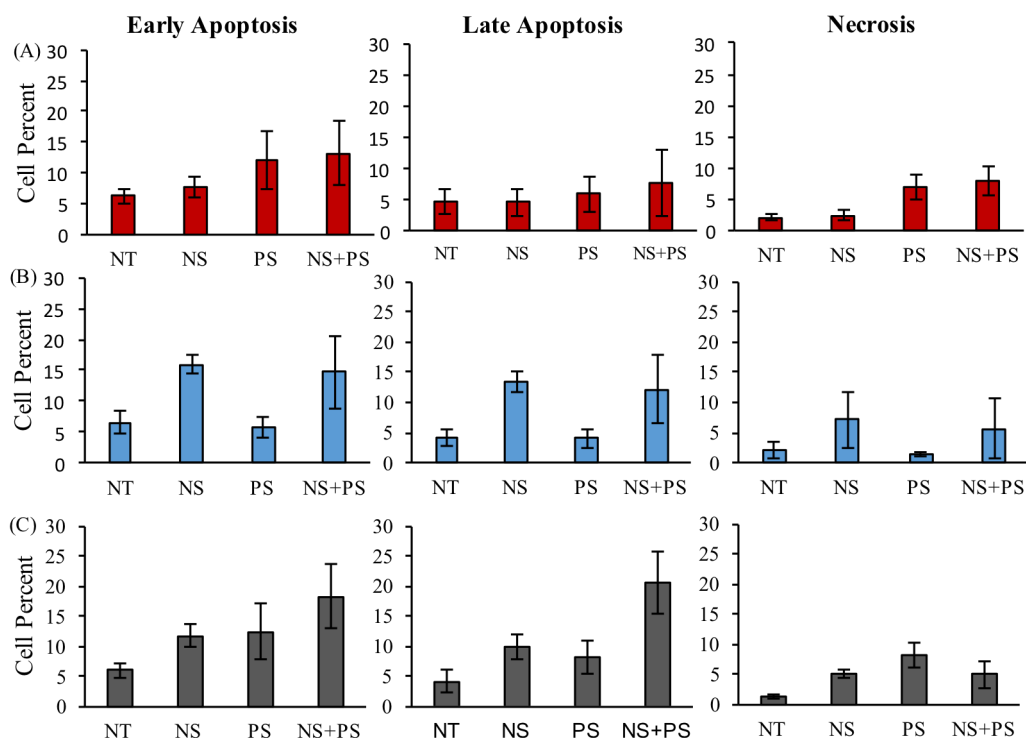


Figure 3.13: Mechanism of cell death following PDT/PTT. Cells were treated with PEG-NS and/or Pd[DMBil1]-PEG₇₅₀ and (A) >500 nm light, (B) 808 nm light, or (C) >500 and 808 nm light. Early apoptotic cells are shown in the left column, late apoptosis is in the middle column, and necrosis is in the right column.

3.4 Discussion

PDT is routinely used clinically to treat several types of cancer including skin, esophageal, and non-small cell lung cancer, among others.⁹¹ The PSs are typically administered topically or intravenously, allowed to accumulate within tumors for 2-3 days, and then light is applied. For esophageal and lung cancers, the light is applied through an endoscope or bronchoscope, respectively, that is placed down the patient's throat.⁹¹ Alternatively, PDT can be performed during surgery to reach deeply embedded tumors to ablate residual cancer cells left behind during surgery. However, since visible light cannot penetrate tissue, PDT's use as a standalone therapy is limited to surface-localized or easily accessible tumors. Another main challenge faced by

PDT is that it requires sufficient oxygen levels in adjacent tissue to be effective. Since large tumors are highly hypoxic, PDT can only be used to treat small tumors. Finally, PDT as a standalone therapy is limited by toxicity to healthy tissue due to high required doses of commercial PSs. Patients injected with a PS are required to be protected from light for several months following treatment, which may be a hindrance to quality of life. Therefore, a major research focus is to develop novel PSs with decreased toxicity and higher treatment efficacy to mitigate some of these challenges.

The work presented in this Chapter is the first time Pd[DMBil1]-PEG₇₅₀ has been evaluated as a standalone therapy for PDT, or evaluated in combination with PTT. To demonstrate the benefits of Pd[DMBil1]-PEG₇₅₀ compared to other PSs, we investigated the ED₅₀ and LD₅₀ of it and two commercially available PSs in TNBC cells. Through our experiments, we calculated an impressive phototoxicity index of 5300 for Pd[DMBil1]-PEG₇₅₀, which is substantially higher than those of HPDC and IHP. This drastic improvement over commercially available PSs shows that Pd[DMBil1]-PEG₇₅₀ is a very promising PS for PDT.

Although Pd[DMBil1]-PEG₇₅₀ has a better phototoxicity index than existing commercial PSs, it does not address the other key challenges associated with PDT (excitation with visible light and reliance on tissue oxygen). Therefore, a major goal for this research was to evaluate PDT in combination with PTT as a platform for solid tumor treatment that can ultimately be used to reach hypoxic regions of tumors with longer wavelengths of light, while allowing lower doses of the PS, NSs, and various sources of light to be applied. We demonstrated in TNBC cells that dual PDT/PTT was more effective than either therapy alone, as the resultant metabolic activity of

cells was lower when treated with dual PDT/PTT than with either individual therapy. This suggests that lower dosages of each treatment could be applied to enable effective treatment while minimizing potential risk.

Importantly, our studies also confirmed that dual PDT/PTT induces primarily apoptosis, which is vastly preferred over a necrotic cell death mechanism. To date, the most commonly reported *in vitro* cellular response to PTT is necrosis, although a few studies have suggested that apoptosis can be initiated under controlled light exposure conditions.^{104,119,120} More specifically, high-energy irradiation can lead to necrosis while low-energy irradiation can promote apoptosis. Indeed, we showed that applying PDT and PTT with low laser powers could cause cell death *via* apoptosis rather than necrosis. Together, the results presented here demonstrate that dual PDT/PTT mediated through Pd[DMBil1]-PEG₇₅₀ and PEG-NSs is a viable therapeutic strategy that overcomes the common limitations of both PDT and PTT individually, and this should be investigated in solid tumors *in vivo* in the future.

3.5 Conclusions

The results reported herein describe a novel PS characterized by high water solubility, efficient ¹O₂ generation, and a remarkable phototoxicity index. We show that Pd[DMBil1]-PEG₇₅₀ can efficiently produce ¹O₂ with a quantum yield comparable to those observed from PSs currently used in PDT. In fact, we demonstrate that Pd[DMBil1]-PEG₇₅₀ is highly effective for PDT in TNBC cells due to its amenability to cellular uptake, low inherent dark toxicity and high photo-induced toxicity where cell death occurs primarily *via* apoptosis. With these results, the calculated phototoxicity index of this PS is ~5300, which is substantially higher than two commercially available PSs.

Next, we evaluated dual PDT/PTT as a treatment strategy for TNBC to overcome the limitations of each individual therapy. Through these experiments, we demonstrated that dual therapy is more effective than either therapy alone, and this effect is synergistic. We showed that this combination strategy enables primarily apoptotic cell death, which is ideal for any phototherapy to minimize inflammation that can lead to disease recurrence. In summary, the results presented in this Chapter indicate that dual PDT/PTT mediated by Pd[DMBil1]-PEG₇₅₀ and PEG-NS, respectively, warrants further investigation of this strategy to treat TNBC and other cancers characterized by solid tumors.

3.6 Future Work

As previously mentioned, a main limitation of PDT is that it utilizes low wavelengths of light that cannot penetrate tissue to reach tumors within the body. In the dual therapy approach investigated here, we used both >500 nm light from a lightbox and 808 nm light from a laser to independently activate the PS and NSs, respectively. Moving forward, there is great opportunity to conjugate Pd[DMBil1]-PEG₇₅₀ onto the surface of NSs using a thiolated PEG linker. Upon excitation with a pulsed 800 nm laser, NSs emit 500-600 nm light that extends only a few nanometers from their surface. Therefore, directly conjugating the PS onto NSs may provide a means to both mediate PTT directly and to activate the PS to produce ¹O₂ with only tissue-penetrating NIR light. While this work shows that both PEG-NS and Pd[DMBil1]-PEG₇₅₀ are taken up by cells, and that dual therapy causes cell death more efficiently than either therapy alone, it is critical to evaluate this strategy in a murine model of TNBC. The administered doses here were optimized for experiments in adherent cell culture, and the translation into animal models will require dose

optimization studies for both the PS and NSs to ensure sufficient penetration into solid tumors. Further, the toxicity and PDT efficacy of Pd[DMBi1]-PEG₇₅₀ has not been evaluated in animal models, which will be critical for clinical translation. The PDT results from Pd[DMBi1]-PEG₇₅₀ should be compared to clinically relevant doses of a PS currently used for PDT to demonstrate its benefits *in vivo* over the current gold standard. Finally, we expect that different light parameters (time of irradiation and laser power) will be required *in vivo* compared to the *in vitro* studies presented here. We anticipate that the proposed follow up studies would demonstrate the clinical translatability of Pd[DMBi1]-PEG₇₅₀-mediated PDT, as well as dual therapy, using both this novel PS and PEG-NS. Further, we expect these studies would confirm that combining PS with PEG-NS enables lower required dosages of each while maintaining better efficacy than each therapy alone.

Chapter 4

AN EVALUATION OF THE MECHANISMS OF LIGHT-TRIGGERED siRNA RELEASE FROM NANOSHELLS FOR ON-DEMAND GENE REGULATION

4.1 Introduction to Chapter 4

The ability to regulate intracellular gene expression with exogenous nucleic acids such as small interfering RNAs (siRNAs) has substantial potential to improve the study and treatment of disease. However, most nanoparticle-based carriers that are used for the intracellular delivery of nucleic acids cannot distinguish between diseased and healthy cells, which may cause them to yield unintended widespread gene regulation. The overarching goal of this Chapter was to demonstrate that the unique photophysical properties of NSs could enable them to be used as a platform for on-demand gene regulation. The underlying hypothesis was that NSs coated with siRNA molecules could remain inactive until the siRNA molecules were released from the NSs by activation with tissue-penetrating near-infrared laser light. In examining this hypothesis, we also evaluated the mechanisms of siRNA release of from NSs under two modes of laser irradiation (continuous wave or pulsed) to demonstrate the importance of thoroughly characterizing photoresponsive nanosystems for applications in triggered gene regulation. The structural differences of the siRNA released by each mode of irradiation was characterized, and it was demonstrated that laser irradiation does not damage the siRNA. It was also shown that the ratio of siRNA duplexes to single-stranded molecules that are released is higher for pulsed irradiation than

continuous wave irradiation, making pulsed conditions preferable for gene regulation. Finally, we show that siRNA-NS conjugates can enable on-demand gene silencing upon pulsed laser irradiation using green fluorescent protein (GFP) as a model target. The work presented in this Chapter was published in: Riley RS, *et al.*, Evaluating the Mechanisms of Light-Triggered siRNA Release from Nanoshells for Temporal Control Over Gene Regulation. *Nano Letters*. 2018, 10.1021/acs.nanolett.8b00681.

4.1.1 Small Interfering RNA (siRNA) As A Tool for Gene Regulation

Regulating gene expression by RNA interference (RNAi) *via* the intracellular delivery of siRNA is a promising means to study and treat cancer, as introduced in Chapter 1. In RNAi, siRNA duplexes inside cells are recognized by RISC, which separates the duplex and escorts the antisense strand to its target mRNA to inhibit the transcription of the encoded protein.⁶³ siRNA is desirable as gene regulatory agents because it is more potent and longer-lasting than antisense DNA oligonucleotides, which have been used in the majority of light-triggered nucleic acid-nanoconjugate systems, and it requires no additional chemical modifications to be active inside cells.^{121,122} However, the pre-clinical and clinical use of siRNA is limited by molecular instability, short circulation times, and low cellular uptake.¹²³ Naked siRNA can be complexed with transfection agents to enable cellular uptake, but these cannot be used *in vivo* due to their toxicity and lack of specificity for diseased versus healthy cells, which leads to nonspecific gene regulation. In this Chapter, we designed a siRNA carrier platform composed of NSs coated with radially projected thiolated siRNA molecules via gold-thiol bonding. We hypothesized that this nanoconjugate design could overcome the toxicity and lack of specificity associated with other siRNA

carriers by enabling spatiotemporal control over gene regulation via activation with NIR light.

4.1.2 Nanoparticle Platforms for On-Demand Gene Regulation for Cancer Therapy

Nanoparticle delivery platforms that either encapsulate siRNA or carry siRNA on their surfaces can overcome many of the limitations of naked siRNA by stabilizing the molecules, improving their biodistribution, and enhancing their delivery into cells.^{80,124} Accordingly, siRNA nanocarriers are recognized as powerful gene regulatory agents for cancer treatment. However, these carriers typically cannot distinguish diseased cells from normal cells and, once inside cells, they often fail to reach the cytosol due to entrapment within intracellular compartments, rendering the attached oligonucleotides ineffective.¹²³ To promote successful cytosolic delivery, siRNA nanocarriers are often coated with additional moieties such as cell penetrating peptides or polymers that improve endosomal escape.^{74,125} Unfortunately, these modified NPs may be more toxic than their unmodified counterparts, and they still cannot distinguish healthy cells from diseased cells, which may cause them to elicit unintended widespread gene regulation and substantial off-target effects. An ideal NP platform for gene regulation would enter cells without additional penetration reagents and keep its siRNA cargo inactive until stimulated by an external trigger. Such a system could facilitate on-demand, localized gene regulation while avoiding impacts to non-targeted healthy tissue. To meet this need, researchers have recently begun to develop light-responsive nanocarriers for siRNA delivery and on-demand gene regulation.

Gold-based NPs, such as NSs, that maximally absorb near infrared (NIR) light (~700-1200 nm) are ideal for photoresponsive therapies because these wavelengths can safely penetrate several centimeters of healthy tissue.^{126,127} Literature has shown that light-triggered release of molecules from gold NPs offers several attractive features for gene regulation. First, it has been shown that low-intensity laser irradiation can promote NPs' endosomal escape by producing sufficient heat in the vicinity around the NPs to rupture surrounding endosomes without impact overall cell viability.^{73,128} This is important for NPs carrying siRNA because the siRNA needs to enter the cytosol in order to be recognized by RISC to induce gene silencing. Second, phototherapies and gene regulation can offer synergistic outcomes. For example, PTT has been shown to sensitize cells to gene regulation, and vice versa, gene regulation has been used to sensitize cells to PTT, so the combination of these treatments offers a more robust approach to cancer treatment.^{34,129} Lastly, researchers have shown that laser light can trigger the release of siRNA or other gene regulatory agents such as antisense DNA oligonucleotides from NPs for on-demand gene regulation.^{60,62,73,130,131} In this approach, gene regulation occurs only where light is applied to cause the conjugated gene regulatory agents to release from the NP surface and enter the cytosol; accordingly, this treatment offers very high precision. In this Chapter, we evaluated the mechanism of siRNA release from NSs to understand their capabilities for on-demand gene regulation.

Several gold NP designs have been developed to study the intracellular delivery and light-triggered release of nucleic acids, including nanorods,^{132,133} nanoshells,^{60,130,134} and hollow gold NPs,^{53,73} among others.¹³¹ As mentioned before, however, many of these platforms reported in literature have utilized additional agents

to promote cell uptake that may result in nonspecific off-target gene silencing.^{73,125} An overarching goal in this Chapter was to develop siRNA-coated NSs as a platform for light-triggered gene silencing that does not require additional uptake agents. We used NSs as the core material of our platform to study light-triggered siRNA release from nanocarriers because they are specifically engineered to maximally absorb ~800 nm light, they offer easy bioconjugation, and they have proven safety in human clinical trials.^{45,46,86,127} Further, they are able to penetrate solid tumors and enter cells, two features that are critical for gene regulatory platforms.¹³⁵

4.1.3 Continuous Wave versus Pulsed Laser Irradiation for Triggering Release of Molecules from Nanoparticles

In photoresponsive siRNA nanocarriers, the core NP is carefully chosen for its inherent photophysical properties that enable activation by externally applied light. Upon laser excitation, any surface-conjugated siRNA is released to silence the targeted proteins. Importantly, RISC only recognizes double stranded siRNA,¹³⁶ so it is critical to ensure that the majority of the siRNA released from photoresponsive NPs retains a duplexed structure.

The mode of laser irradiation is a critical experimental design feature, as it is believed to dictate the structure of the released siRNA (Figure 4.1). Prior work using DNA-NS conjugates has shown that continuous wave (CW) irradiation causes large temperature increases of bulk NS solutions over time, which may yield duplex denaturation such that primarily single-stranded oligonucleotides are released, in addition to causing nonspecific cell death.⁶⁰ Alternatively, delivering very short, high energy pulses of laser light to NSs yields a hot-electron transfer effect that breaks the gold-thiol bond attaching the nucleic acids to the NSs without increasing bulk solution

temperature.^{61,73} Jain, *et al.* speculated that this bond dissociation is due to coupling of the NPs' photoexcited electrons and the gold-sulfur bond vibrations, rather than thermal heating as experienced through CW irradiation.⁶¹ Due to these differences, it is commonly believed that CW irradiation leads to release of single-stranded oligonucleotides, while pulsed laser irradiation leads to release of entire duplexes to induce RNAi-mediated gene regulation (Figure 4.1). In this Chapter, this belief is tested using a powerful combination of NP characterization and molecular biology techniques to characterize the siRNA that is released from NSs under exposure to various CW or pulsed irradiation conditions.

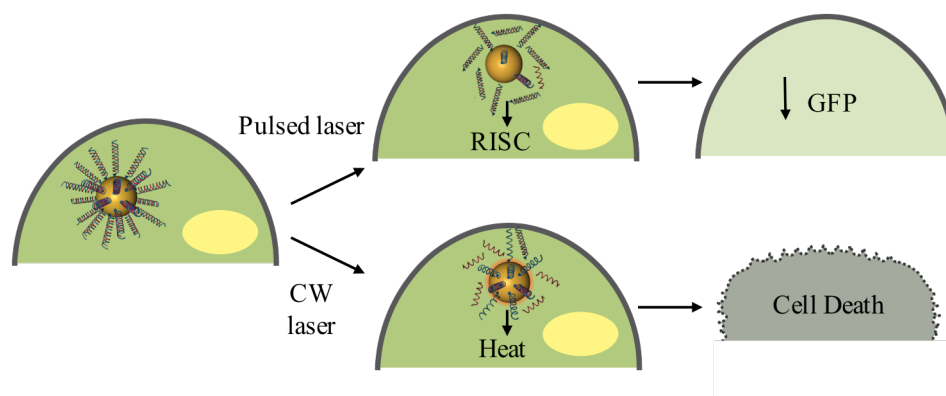


Figure 4.1: Schematic showing the process of on-demand gene regulation with siRNA-NS conjugates. When cells treated with siRNA-NS are exposed to a femtosecond pulsed laser, there is no change in temperature and the released siRNA consists primarily of duplexes. Upon release, the duplexed siRNA molecules are recognized by RISC, which guides the siRNA to its' target mRNA to induce degradation. Alternatively, CW irradiation causes NSs to generate a substantial amount of heat that releases both single stranded RNA and duplexes and that can cause nonspecific cell death without achieving the desired gene silencing. In this work, we evaluate light-triggered release of GFP siRNA to induce GFP downregulation in cells.

4.2 Materials and Methods

NSs were synthesized and functionalized with siRNA and mPEG-SH as explained in Chapter 2. To quantify and characterize siRNA release from NSs upon CW or pulsed laser irradiation, we coated NSs with a scrambled form of GFP-targeted siRNA tagged with a Cy5 fluorophore on the 3' end of the antisense strand for detection (Figure 4.2). For light triggered gene regulation experiments, NSs were coated with GFP or scrambled siRNA duplexes without any conjugated fluorophores (Table 4.1). siRNA content was quantified using a Quant-iT OliGreen™ ssDNA quantification kit or by the inherent Cy5 fluorescence as explained in Chapter 2.

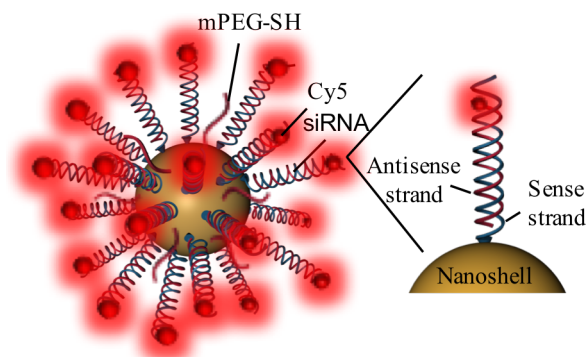


Figure 4.2: Schematic of Cy5-siSCR-NS showing position of Cy5 fluorophore on the 3' end of the antisense strand of the siRNA.

Table 4.1: siGFP, siSCR, and Cy5 siSCR siRNA sequences used in this work, denoted 5' to 3'.

Name	Sequence
GFP Antisense	GGUGCGUCCUGGACGUAGCCTT
GFP Sense	GGCUACGUCCAGGAGCGCACCTT-(Sp18)(Sp18)-Thiol
Scram Antisense	UGCCGAUCGGCACGGUCGCGUTT
Scram Sense	ACGCGACCGUGCCGAUCGGCATT-(Sp18)(Sp18)-Thiol
Cy5 Scram Antisense	UGCCGAUCGGCACGGUCGCGUTT-Cy5

4.2.1 Characterization of Temperature and siRNA Release Upon Laser Irradiation

Cy5-siRNA-NS were diluted in RNase-free milliQ water to 5.5×10^9 NS/mL (corresponding to OD 2), and 2 mL was placed into RNase-free disposable cuvettes with stir bars and samples were stored on ice until use. For both CW and pulsed laser experiments, samples were irradiated from the side while stirring. An 808-nm CW laser (B&W Tek) was applied at 0, 5, 10, 20, or 25, or 30 W/cm² with a 2 mm spot size (corresponding to 0, 157, 314, 628, 785, 942 mW output powers) for 30 min. Thermal images were taken every 5 min with an FLIR A5 thermal camera (FLIR Systems) and the highest temperature at each timepoint was recorded. The 800 nm pulsed laser utilized in these experiments (Coherent) was equipped with a modelocked Ti:Sapphire oscillator (Mantis) and a regenerative amplifier (Legend Elite). Samples were irradiated with a 10 kHz repetition rate and 40 fs pulse length. Samples exposed to this laser were irradiated with a 50 μ m spot size focused using a fused silica lens with a focal length of 30 cm. siRNA-NS were irradiated with 1, 2, or 3 mW output power for 10, 20, or 30 min.

Following irradiation with the CW or pulsed laser, samples were read on a UV-vis spectrophotometer, centrifuged to form a pellet (1500xg, 5 min), and the supernatant containing any released RNA was collected. Sample Cy5 fluorescence was read on a Synergy H1 plate reader and compared to a standard curve of known siRNA concentration (0-10 nM) to quantify the amount of siRNA released. The remaining supernatant was lyophilized overnight for gel electrophoresis to analyze the structure of the released siRNA. For this, samples were diluted in milliQ water and RNA content was determined using a Take3 plate on the Synergy H1 plate reader using the absorbance at 260 nm. Samples were combined with 2X formamide buffer,

boiled at 99°C for 3 min, and quickly cooled on ice. 100 ng of siRNA duplexes, Cy5-antisense strands, thiolated sense strands, or released siRNA was run on 4-20% TBE gels (Lonza) at 125-175 V for 1 hr in 1X TBE buffer. Then, gels were placed into 1X SYBR Gold (Thermo Fisher) diluted in TBE buffer for 20 min. Lastly, gels were imaged using the ethidium bromide filter on a ChemiDoc-iTTM2 Imager (UVP) with a 5 sec exposure time. Band intensity was analyzed in Fiji (ImageJ) software using the gel analyzer feature.

Following centrifugation, the NS-containing pellets were suspended in 2 mL milliQ water and analyzed by dynamic light scattering for hydrodynamic diameter and by flow cytometry for Cy5 fluorescence intensity using a forward scatter cutoff of 10 and the APC filter (excitation/emission 640 nm/660 nm). The purpose of these assays was to provide qualitative evidence of siRNA release and NS structure.

4.2.2 U373.eGFP Cell Culture

U373.eGFP (enhanced green fluorescent protein) glioma cells were gifted from Dr. Susan Blaney of Texas Children's Hospital and were cultured in Dulbecco's Modified Eagle Medium (DMEM) supplemented with 10% fetal bovine serum (FBS) and 1% penicillin-streptomycin. Cells were cultured in T75 cell culture flasks, passaged with 0.25% trypsin-EDTA, and incubated at 37°C in a 5% CO₂ environment. Flasks were grown to 80-90% confluence prior to plating for experiments.

4.2.3 Transfection with Released GFP siRNA

The following methods were utilized to evaluate whether siRNA released from NSs upon activation with pulsed light retains its gene silencing functionality. U373.eGFP cells were detached from flasks with 0.25% trypsin-EDTA, counted on a

hemocytometer, plated at 5,000 cells/well in 96 well plates in complete cell culture media, and incubated overnight. siGFP-NS and siSCR-NS were diluted in RNase-free water to 5.5×10^9 NS/mL (OD2), and 4 mL of each sample type was placed into cuvettes with stir bars. The NS samples were irradiated with the pulsed laser at 3 mW for 30 min while stirring. Then, samples were centrifuged to form a pellet and the supernatant containing released RNA was collected and lyophilized overnight. Following lyophilization, the released siRNA was diluted in RNase-free water and the RNA concentration was determined using the Take3 plate on the Synergy H1 plate reader using the absorbance at 260 nm. To examine whether the released RNA retained its functionality, plated U373.eGFP cells were transfected with 100 nM of the released GFP or scramble siRNA with Dharmafect (Dharmacon) per manufacturer recommendations, and after 6 hr the transfection solution was replaced with antibiotic-free media. Cellular GFP expression was analyzed at 48 hr and 96 hr post-transfection by fluorescence imaging with an EGFP filter on a Zeiss Axioobserver Z1 Inverted Fluorescence Microscope. For flow cytometry (to quantify GFP silencing), cells were lifted with 0.25% trypsin-EDTA and treated with propidium iodide (PI, Thermo Fisher) for 5 min at room temperature per manufacturer recommendations to enable the exclusion of dead cells by flow cytometry. To analyze the flow cytometry data throughout this Chapter, first the cell population was selected using forward scatter versus side scatter density plots. Then, singlet cells were gated using forward scatter height versus area density plots. Finally, eGFP expression was determined using the FITC channel (excitation/emission 488/530). The median fluorescence intensity (MFI) data shown are the averages and standard deviations from three independent experiments.

4.2.4 Light-Triggered GFP Silencing in U373.eGFP Cells with siRNA-NS

To assess cell uptake of siRNA-NS conjugates, U373.eGFP cells were plated at 5,000 cells/well in 96 well plates and incubated overnight. Cy5-siRNA-NS diluted to 1.4×10^{10} NS/mL (OD5) in complete cell culture medium were added to the cells, which were then incubated for 3 hr. For flow cytometry, cells were lifted with 0.25% trypsin-EDTA, centrifuged, suspended in 1X PBS, and the Cy5 signal was measured using the APC filter. For imaging, cells were fixed with 4% formaldehyde in PBS for 15 min and then treated with DAPI overnight at 4°C to stain cell nuclei. After overnight incubation, cells were imaged on the Zeiss Axioobserver Z1 fluorescent microscope using the DsRed, EGFP, and DAPI filter sets.

To assess GFP knockdown, U373.eGFP cells were plated at 100,000 cells/well in 6-well plates and incubated overnight. Then, cells were treated with 2 mL of siGFP-NS or siSCR-NS diluted to 1.4×10^{10} NS/mL (OD5) in complete cell culture media. After 3 hr, cells were detached with 0.25% trypsin-EDTA, centrifuged 1X at 200xg for 5 min, and suspended in 1 mL of sterile 1X PBS. Cells were placed into sterilized cuvettes with stir bars and kept on ice throughout the duration of the experiment, except during irradiation. While the NS-treated cells stirred in the cuvettes, the femtosecond pulsed laser was applied at 0 or 3 mW for 20 min. After irradiation, the cells were centrifuged, suspended in media, counted, and plated in 24 well plates at 45,000 cells/well. The media was replaced every day, and the cells were analyzed for GFP expression using fluorescence microscopy (EGFP channel) and flow cytometry (FITC channel) 4 days after light treatment. The MFI data shown are normalized to the siSCR-NS treated cells in each experiment and then averaged together from four independent experiments. Statistics were analyzed by one-way analysis of variance with posthoc Tukey Kramer.

4.3 Results

4.3.1 Continuous Wave Laser Irradiation Causes Substantial Temperature Increases Compared to Pulsed Irradiation

Solutions of Cy5-siSCR-NS at a concentration of 5.37×10^9 NS/mL were irradiated from the side with either an 808-nm CW laser or a femtosecond pulsed 800-nm laser while stirring (Figure 4.3). Samples undergoing CW irradiation were exposed to 0, 157, 314, 628, 785, 942 mW (corresponding to 0, 5, 10, 20, 25, or 30 W/cm^2) laser powers for 30 min to investigate the temperature dependence on siRNA release. Thermal images were taken with an FLIR camera every 5 min, and the highest temperature of the NS solution was recorded. In agreement with literature,⁶⁰ we found that the bulk solution temperature dramatically increased upon CW irradiation in accordance with exposure time and laser power, and samples reached temperatures up to 52°F with the powers used in this study (Figure 4.4). Importantly, the high temperatures reached during CW irradiation are sufficient to cause nonspecific cell death,^{104,137} making the laser powers studied here irrelevant for light-triggered gene regulation. Bulk solution temperatures were also investigated under pulsed laser irradiation using 3 mW output power, which is the highest power we investigated for siRNA release, for up to 30 min, and we found that the bulk solution temperature did not change (Figure 4.4, black dotted line). These results demonstrate that the use of CW irradiation for triggered gene regulation is limited by changes in bulk solution temperature, and any resultant siRNA release is a temperature-dependent process.⁶⁰ Alternatively, pulsed laser irradiation is a temperature-independent process, suggesting that siRNA release is caused by a different mechanism such as breakage of the gold-thiol bond.

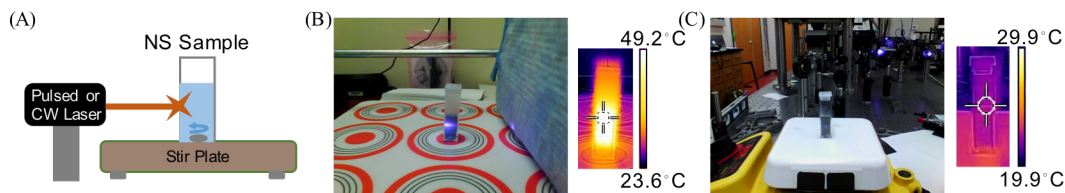


Figure 4.3: Laser irradiation setup. (A) Schematic of irradiation setup for bulk NS solutions under both continuous wave and pulsed laser irradiation (schematic not to scale). (B) and (C) Photographs and thermal images showing the 808 nm continuous wave laser experimental setup, and the pulsed irradiation experimental setup, respectively.

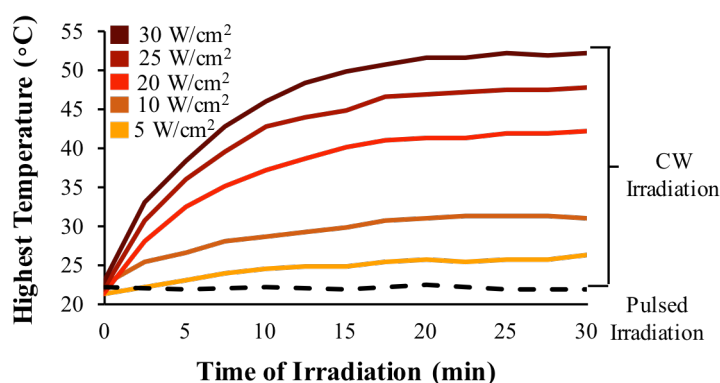


Figure 4.4: Bulk solution temperature measurements of Cy5-siSCR-NS exposed to 808 nm continuous wave light (solid lines) or 800 nm pulsed light at 3 mW for 30 min (dotted black line).

4.4 NS Irradiated with Continuous Wave Light Experience Structural Changes

Next, we tested the ability of CW and pulsed laser irradiation to induce siRNA release, and we thoroughly characterized both the NSs and the released siRNA following laser treatment. First, we investigated how CW or pulsed laser irradiation impact NS structure and size by UV-visible spectrophotometry (UV-vis) and dynamic light scattering (DLS) (Figure 4.5). CW irradiation with 0, 5, 10, 20, 25, or 30 W/cm² for 30 min caused no critical changes in the extinction spectrum or hydrodynamic diameter of Cy5-siSCR-NS, indicating that NSs are still intact and functionalized with

a substantial amount of siRNA and mPEG-SH following CW irradiation (Figure 4.5A).

Alternatively, irradiation with 1, 2, or 3 mW pulsed light for 10, 20, or 30 min resulted in extensive structural changes to Cy5-siSCR-NS (Figure 4.5B).

Spectrophotometry results demonstrate that the structural integrity of NSs is preserved up to 3 mW output power for 20 min. At 3 mW, the peak extinction at 800 nm decreases, indicating a change in NS structure. Further, this change depends on irradiation time, as samples irradiated with the pulsed laser at 3 mW for 10 min do not experience a change in their extinction spectrum (Figure 4.5B, left). DLS measurements show that the hydrodynamic diameter of Cy5-siSCR-NS decreases from 181.3 ± 7.1 nm before laser treatment to 173.7 ± 23 nm and 155.1 ± 7.3 nm after irradiation with 3 mW for 20 or 30 min, respectively. With these higher irradiation times, the hydrodynamic diameter of the laser-treated NSs is reduced to the original size of bare NSs, whereas lower laser powers and irradiation times do not result in notable changes in hydrodynamic diameter (Figure 4.5B, right). This confirms our spectrophotometry results that indicate the structure of Cy5-siSCR-NS changes with pulsed laser irradiation at 3 mW, and suggests that the majority of both siRNA duplexes and mPEG-SH are removed from NS surfaces upon pulsed laser excitation.

An added benefit of utilizing NSs as the core material for investigating light-triggered siRNA release from nanocarriers is that NSs can be detected by forward- and side- scatter profiles in flow cytometry, a technique that has not yet been explored to directly detect fluorescently tagged NSs. We expected that the Cy5 signal from NSs would decrease proportionally to the amount of siRNA released during irradiation. In agreement with our spectrophotometry and DLS data, we found that Cy5-siSCR-NS

solutions treated with CW light do not experience a shift in Cy5 fluorescence intensity, indicating that the majority of the Cy5 fluorophores remain attached to the NS surface following irradiation (Figure 4.6A). Alternatively, the fluorescence of Cy5-siSCR-NS decreases with increased pulsed laser powers and irradiation times, indicating that the pulsed laser sufficiently triggers release of surface-conjugated molecules (Figure 4.6B).

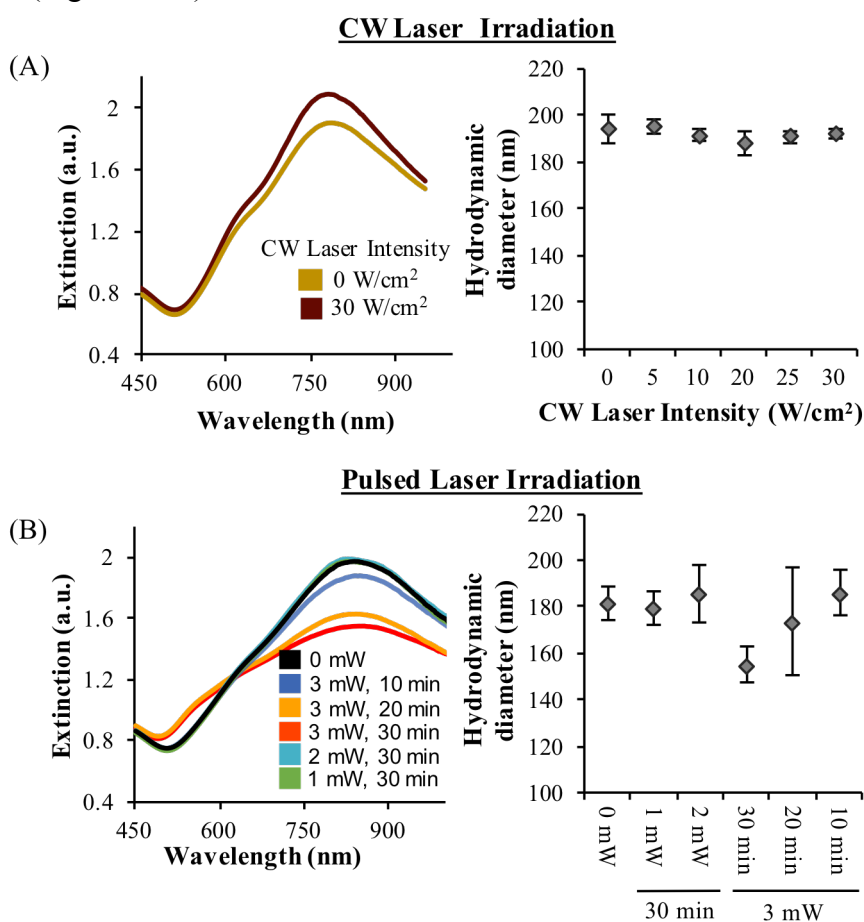


Figure 4.5: NS characterization after laser treatment. (A) Characterization of Cy5-siSCR-NS irradiated with the CW laser. UV-visible spectrophotometry following irradiation with 808 nm CW light for 30 min (left), and hydrodynamic diameter of Cy5-siSCR-NS following irradiation with the 808 nm continuous wave laser at 0, 5, 10, 20, 25, or 30 W/cm² for 30 min (right). (B) Characterization of Cy5-siSCR-NS irradiated with a femtosecond pulsed laser at 0, 1, 2, or 3 mW for 0, 10, 20, or 30 min. UV-visible extinction spectrum (left) and hydrodynamic diameter measurements after irradiation (right).

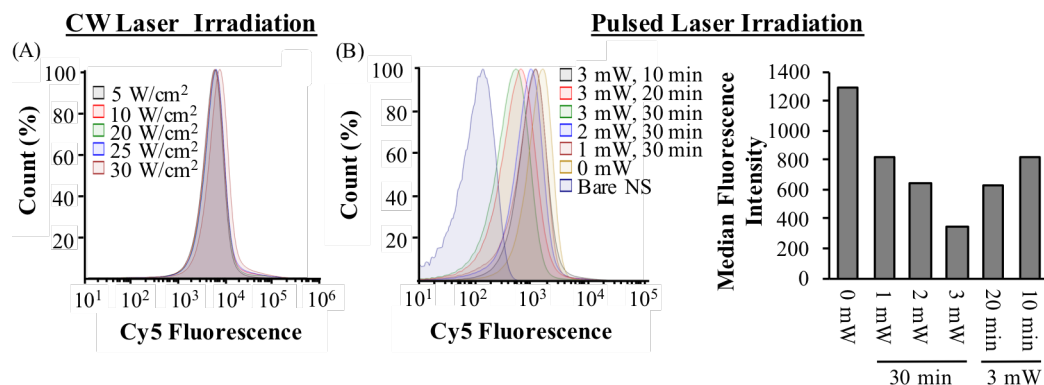


Figure 4.6: Flow cytometry analysis of NS structure. Characterization of Cy5-siSCR-NS following siRNA release by flow cytometry of Cy5 fluorescence signal. (A) Samples were irradiated with the CW laser for 30 min at 5, 10, 20, 25, or 30 W/cm². (B) Samples were irradiated with the pulsed laser at 0, 1, 2, or 3 mW for 10, 20, or 30 min.

4.4.1 Pulsed Laser Irradiation Triggers the Release of siRNA from NS with Higher Efficiency than CW Laser Irradiation

We hypothesized that siRNA release from NSs upon pulsed or CW excitation would depend highly on laser power and irradiation time. To investigate this, we quantitatively examined the efficacy of CW and pulsed laser irradiation for triggered siRNA release by detecting the Cy5 signal of released siRNA following laser irradiation. The original loading of siRNA on NSs was determined by first separating the duplexes using urea and comparing the Cy5 signal in the supernatant to a standard curve of known antisense concentration. Following irradiation with the CW laser (0, 5, 10, 20, 25, or 30 W/cm² for 30 min) or the pulsed laser (0, 1, 2, or 3 mW for 0, 10, 20, or 30 min), samples were centrifuged and the siRNA-containing supernatant was collected. siRNA content in the supernatant was quantified by comparing the Cy5 fluorescence from each sample to a standard curve of known siRNA content. Then, we divided the amount of released siRNA by the original loading to determine the percent siRNA released at each laser power and irradiation time.

We found that the amount of siRNA released under both modes of irradiation was highly dependent on both laser power and irradiation time. For example, CW irradiation resulted in a linear increase in released siRNA at the laser powers studied here, and the maximum siRNA release was 36% with 30 W/cm² (Figure 4.7A). Notably, the temperatures reached during CW irradiation at 30 W/cm² (Figure 4.4) would cause nonspecific cell death and therefore this strategy would not be effective for light-triggered gene regulation. Alternatively, pulsed laser irradiation caused an exponential increase in released siRNA (Figure 4.7B). Pulsed irradiation at 1 mW only minimally released siRNA above background levels, but samples treated with 2 mW or 3 mW of pulsed light experienced 33% and 72% siRNA release, respectively (Figure 4.7B, left). A similar trend was observed for increasing irradiation times when samples were exposed to the 3 mW output power (Figure 4.7B, right). These results agree with our DLS and flow cytometry analyses and demonstrate that the pulsed laser is substantially more effective than the CW laser for triggering siRNA release at the laser parameters studied here.

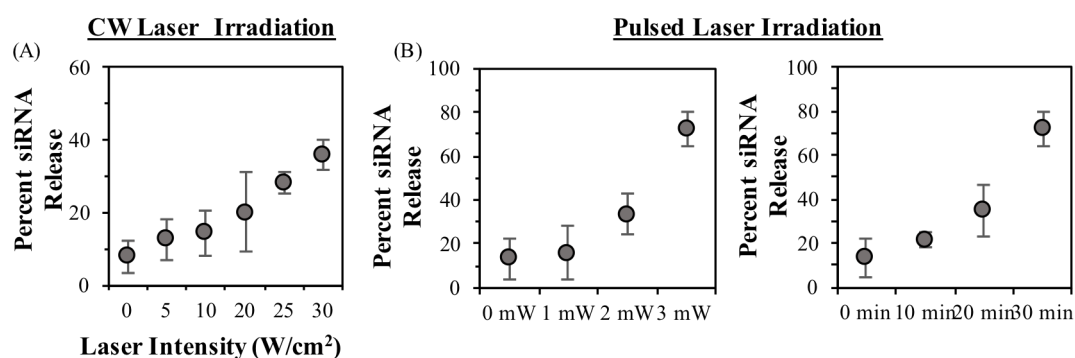


Figure 4.7: Percent siRNA release following irradiation of Cy5-SCR-NS with (A) 808 nm continuous wave irradiation at 0, 5, 10, 20, 25, or 30 W/cm² for 30 min, or (B) Pulsed laser irradiation with 0, 1, 2, or 3 mW for 30 min (left) or 3 mW pulsed light for 0, 10, 20, or 30 min (right), to show the power and time dependence of the siRNA release from NS.

4.4.2 Pulsed Irradiation Primarily Releases More siRNA Duplexes than CW Irradiation

Next, we evaluated whether the siRNA released from NSs retains the proper structure to mediate gene regulation inside cells. As previously mentioned, the released siRNA must be duplexed in order to be recognized by RISC and guide degradation of its target mRNA. Therefore, it is critical to investigate the structure of the released siRNA under each mode of irradiation. It is generally believed that the increased temperatures generated during CW irradiation primarily cause only antisense strands to be released due to duplex denaturation,¹³⁸ whereas pulsed laser irradiation releases entire duplexes by breakage of the gold-thiol bond.^{61,139} Here, we employed gel electrophoresis to directly analyze the siRNA structure based on its size, which is directly related to the number of oligonucleotides in the sequence. After irradiating solutions of Cy5-siSCR-NS, we pelleted the NPs by centrifugation, lyophilized the supernatant, and ran gel electrophoresis on 100 ng of the released siRNA. Contrary to literature,^{60,133,134} we found that CW irradiation leads to a mixture of both duplexes and antisense strands being released from NSs (Figure 4.8A). This underscores the importance of the experimental method we utilized for this work.

Alternatively, and as expected, the siRNA released with the pulsed laser was primarily double-stranded, as the brightest band from these samples appears at ~40 base pairs (Figure 4.8B). To quantitatively compare the amount of duplexes and antisense strands released from NSs, we quantified the band intensities from the gel electrophoresis experiments and calculated the ratio of duplex to antisense released for both modes of irradiation at the highest laser powers used. Pulsed laser irradiation with 3 mW exposure and CW irradiation with 30 W/cm² exposure resulted in duplex:antisense band intensity ratios of 3.2 and 1.23, respectively. Overall, this

shows that pulsed laser irradiation releases a higher percentage of duplexes than CW irradiation with substantially lower incident laser powers. Our findings demonstrate that researchers should carefully characterize their photoresponsive nucleic acid carriers using a variety of techniques, and also suggest that more studies are needed to identify laser parameters for CW irradiation that may enable duplex release without causing substantial temperature increases.

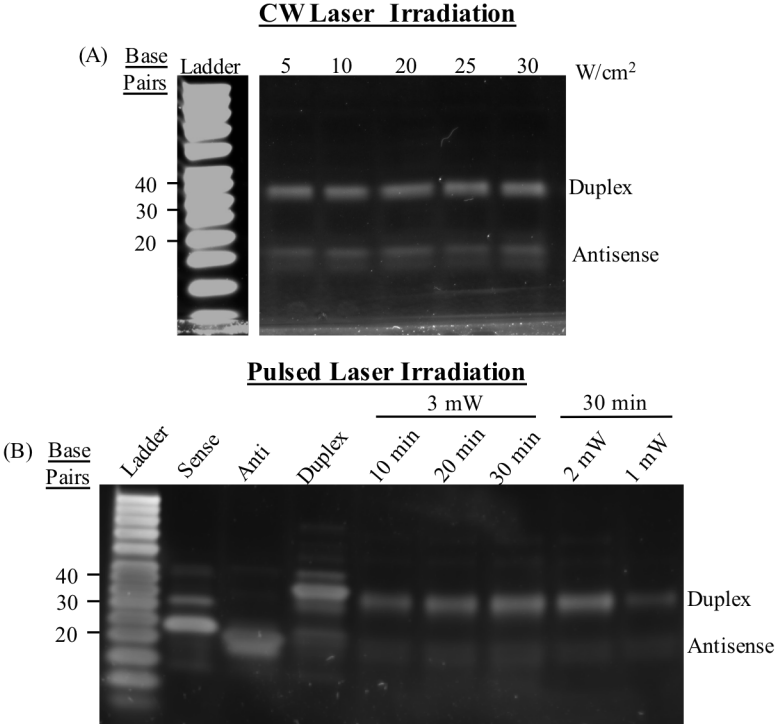


Figure 4.8: Gel electrophoresis of siRNA released from NSs following (A) Continuous wave irradiation at 0, 5, 10, 20, 25, or 30 W/cm² for 30 min or (B) pulsed laser irradiation with 1, 2, or 3 mW for 10, 20, or 30 min. For size comparison, the gel in (B) also shows stock siRNA sense strands, antisense strands, or duplexes that did not undergo laser irradiation.

4.4.3 Released siRNA Retains its Gene Silencing Functionality

We also performed experiments to ensure that the siRNA released from NSs upon laser treatment retains its functionality and is not damaged during laser irradiation. For this study, we designed siRNA-NS conjugates to silence green fluorescent protein (GFP, siGFP-NS) in U373.eGFP cells. We used this cell line because it stably expresses GFP and therefore serves as an ideal platform to investigate light-triggered gene silencing by fluorescence analysis. First, we collected released siRNA from the supernatant of siGFP-NS conjugates following pulsed laser irradiation, and transfected cells with 100 nM of this released siRNA. Cells transfected with GFP siRNA that had been released from NSs experienced substantial downregulation of GFP expression compared to cells transfected with scrambled (SCR) siRNA that had been released from NSs at both 48 hr and 96 hr, indicating that the siRNA is still functional following laser treatment (Figure 4.9). Importantly, this data shows that siRNA-mediated GFP silencing is prominent for at least 4 days following transfection, which is an important feature for gene regulation.

4.4.4 siRNA-NS Conjugates Enter Cells to Mediate On-Demand Gene Regulation

Next, we directly evaluated the ability of siRNA-NS conjugates to enter U373.eGFP cells and mediate on-demand gene silencing. First, we treated U373.eGFP cells with Cy5-siSCR-NS for 3 hr to evaluate cell uptake by fluorescence imaging, which showed a substantial amount of uptake at this time point (Figure 4.10A). These results were confirmed by flow cytometry, which revealed a 22-fold enhancement in Cy5 signal from cells treated with Cy5-siSCR-NS compared to untreated cells (Figure 4.10B).

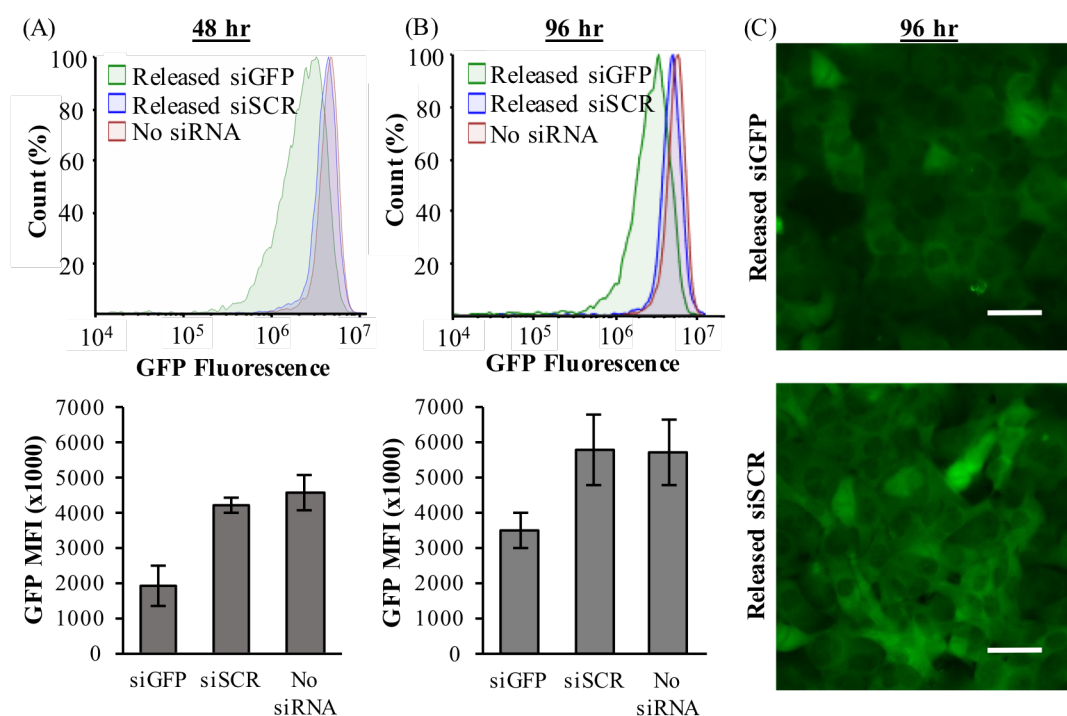


Figure 4.9: GFP knockdown in transfected cells. (A and B) Flow cytometry analyses and (B) fluorescence images showing GFP expression in U373 cells transiently transfected with 100 nM GFP siRNA, SCR siRNA, or no siRNA that was released from NS using 3 mW femtosecond pulsed laser for 30 min while stirring. The data shown is (A) 48 hr and (B and C) 96 hr post-transfection. Scale=50 μ m.

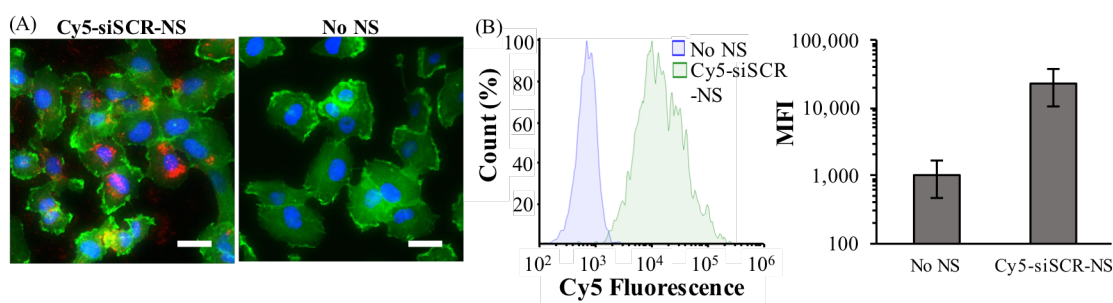


Figure 4.10: Cell uptake of Cy5-siSCR-NS. Fluorescence imaging (A) and flow cytometry (B) of Cy5-siSCR-NS (red) uptake by U373.eGFP cells 3 hr post-addition to the culture medium (scale = 50 μ m; GFP=green, nuclei=blue). Control cells were treated with no NS.

To examine light-triggered gene knockdown in U373.eGFP cells, the cells were treated with NSs coated with GFP-targeted siRNA (siGFP-NS) or its scrambled

form (siSCR-NS) at 1.4×10^{10} NS/mL in complete cell culture media for 3 hr, then placed into sterile cuvettes for laser treatment with 3 mW pulsed laser for 20 min while stirring. After laser treatment, the cells were plated in 24-well plates and incubated for 4 days prior to GFP analysis. Flow cytometry revealed that cells treated with siGFP-NS and the laser experienced a 35% decrease in normalized median fluorescence compared to cells treated with siSCR-NS (Figure 4.11). Further, cells treated with siGFP-NS and the pulsed laser had 33% lower GFP expression than cells treated with siGFP-NS and no laser. Interestingly, the original siRNA loading on siGFP-NS was 652-1463 siRNA/NS, which correlates to 15-34 nM siRNA added to cells. Therefore, the amount of siRNA present on siGFP-NS in these experiments was 3-6.5X less siRNA than the 100 nM siRNA used for the transfections previously discussed (Figure 4.9). These results indicate that NS-mediated delivery of siRNA is more effective for gene silencing than using commercially available transfection reagents. Further, utilizing NSs as the core nanomaterial enables on-demand control over gene silencing, which will ultimately avoid undesired side effects from nonspecific and widespread gene regulation.

4.5 Discussion

In this Chapter, we have presented several new insights into the field of on-demand gene regulation. Most light-triggered release studies evaluate the release of DNA from NPs rather than siRNA, although the latter provides many benefits for gene regulation over DNA.^{60,121,122,133,139,140} This is because DNA is more stable than siRNA, making it easier to study. However, because siRNA has a unique secondary structure, it cannot be assumed that its release mechanisms will match those that have been observed for DNA. Previously, Jain *et al.* demonstrated that DNA release from

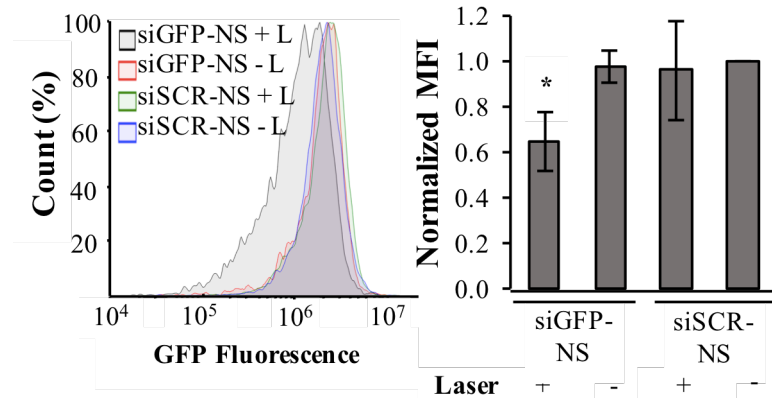


Figure 4.11: Analysis of GFP silencing upon pulsed laser irradiation. Flow cytometry of GFP expression in U373.EGFP cells treated with siGFP-NS or siSCR-NS for 3 hr and then irradiated for 30 min with 0 or 3 mW pulsed light. The data shown represents GFP expression 4 days after irradiation compiled from four independent experiments. * $p < 0.05$ by one-way ANOVA with posthoc Tukey-Kramer.

photoresponsive NPs upon pulsed laser irradiation is a result of hot electron transfer effects between the gold NP and the DNA molecules.⁶¹ Since we primarily see duplex release from pulsed laser irradiation, our results also indicate a hot electron transfer effects between the molecules and NS surfaces as the primarily mechanism of action.

Using gel electrophoresis, we also demonstrated in this Chapter that CW irradiation can release duplexed siRNA from NSs, which is critical for RNAi, but this release is not as efficient as release triggered by pulsed laser irradiation. This finding is contrary to literature, as most studies have shown or assumed that CW laser light causes solely antisense siRNA strands to be released. This antisense release is due to NP heating in response to the CW laser, which causes duplex denaturation such that only antisense strands release while thiolated sense strands remain tethered to the NP surface. The results presented in this Chapter show that CW light can release both duplexed siRNA and antisense strands, so additional studies evaluating shorter CW

irradiation times with higher laser powers may enable siRNA-NS conjugates to be used for gene regulation under either pulsed or CW laser modalities.

In addition to characterizing the released siRNA following laser irradiation, we also showed that siGFP-NS are substantially more effective for GFP knockdown than unconjugated siRNA complexed with a commercial transfection reagent. This is important because siGFP-NS can silence GFP with dosages as low as 15 nM. Of note, we accomplish comparable GFP knockdown with 100 nM siRNA introduced with a commercial transfection reagent, indicating that as much as 6.6X less siRNA is required using our platform compared to transfection reagents. As previously mentioned, a main limitation regarding the clinical translatability of siRNA is that it requires high treatment dosages leading to off target impacts to healthy tissue. Therefore, the siRNA-NS platform explored here can be used to overcome this limitation by enabling much lower siRNA doses to be administered.

A key limitation of most siRNA nanocarriers is that they enter both healthy cells as well as diseased cells, which can lead to undesirable gene regulation in healthy tissues that require normal gene expression. Light-triggered nanoplatforms such as siRNA-NS are ideal for overcoming this hurdle because they can remain inactive until excited with laser light. Since siRNA release occurs only where light and siRNA-NS are combined at the tumor site, this strategy offers very high precision. Notably, we demonstrated in this Chapter that our siRNA-NS platform does not require any additional materials to enhance cellular uptake or promote gene silencing. This is a key feature of our design as compared to other light-responsive siRNA nanocarriers,^{74,125} as cell penetrating peptides and polymers may lead to nonspecific toxicity and gene regulation in healthy tissues. Taken together, the results provided in

this Chapter demonstrate the use of NSs as the base platform for siRNA delivery for tumor cell-specific gene regulation. Additionally, this platform can be adapted to silence any oncogene of interest for high precision silencing in cancer cells.

4.6 Future Work

The work in this Chapter shows that NSs can serve as a platform for light-triggered siRNA release under either CW or pulsed laser irradiations, but pulsed laser irradiation is more efficient and can therefore be used to mediate on-demand silencing of GFP in GFP-expressing glioma cells. While knockdown of fluorescent markers like GFP is critical to demonstrate the potential of this siRNA-NS platform, it is imperative moving forward to also study this system using a clinically relevant oncogenic target. For example, this platform could be investigated using NS coated with β -catenin siRNA to inhibit the Wnt signaling pathway in TNBC, which is described in more detail in Chapter 5. Further, additional investigations into the use of CW laser light for light-triggered gene regulation would prove that the utility of this system is flexible and can be optimized for two modes of irradiation. This is important because CW lasers are cheaper than pulsed lasers, and may therefore be more readily implemented into the clinic. Additionally, this platform is robust, so it can be adapted to silence any overactive oncogenic gene of interest simply by interchanging the conjugated siRNA molecules. Finally, this platform should be evaluated in murine models of solid tumor cancers, such as TNBC. This is important since the parameters of light irradiation that are needed for on-demand gene regulation *in vivo* are likely different from those observed *in vitro*, and *in vivo* studies would also confirm that this platform can increase tumor-specific gene silencing while decreasing off-target effects to healthy

tissues not exposed to laser light. Overall, with further development, siRNA-NS conjugates have substantial potential as tools for high precision cancer therapy.

4.7 Conclusions

Our overarching goal in this work was to evaluate light-triggered siRNA release from NSs upon CW or pulsed laser irradiation and to demonstrate the importance of carefully choosing laser parameters for maximal release and gene knockdown. We developed siRNA-coated NSs and thoroughly characterized their use for on-demand gene regulation using pulsed and CW NIR light. Using gel electrophoresis, we demonstrated that pulsed laser irradiation primarily releases duplexes of siRNA, making it usable for RNAi. Interestingly, we found that CW irradiation also releases duplexes of siRNA at the laser powers studied here, although not as effectively as pulsed laser irradiation. Additionally, the temperatures reached during CW irradiation would cause nonspecific cell death, making CW irradiation impractical for gene regulation purposes. Further, we found that pulsed laser irradiation with 3 mW can induce up to 72% release of the conjugated siRNA, and we show that the released siRNA is still functional to enable on-demand GFP knockdown in GFP-expressing U373 cells. This platform offers temporal control over gene silencing with low concentrations of siRNA to overcome the common limitations with other nanoparticle systems, and our results demonstrate that light-triggered siRNA release facilitated through siRNA-NS conjugates is a promising means of enabling gene regulation on-demand.

Chapter 5

**MOLECULARLY-TARGETED NANOSHELLS FOR MULTIVALENT
BINDING AND WNT SIGNALING INHIBITION IN
TRIPLE-NEGATIVE BREAST CANCER**

5.1 Introduction to Chapter 5

Antibodies that antagonize cell signaling pathways specific to their targeted receptor are invaluable tools to study and treat malignancies, but their utility is limited by high production costs and treatment dosages. Researchers have shown that antibodies conjugated to nanoparticles display increased avidity for their target relative to freely delivered antibodies due to multivalency (the ability to engage multiple receptors simultaneously for increased binding strength). We hypothesized that the multivalent binding afforded by antibody-NP conjugates could enable them to inhibit oncogenic cell signaling more effectively than freely delivered antibodies. In this Chapter, we tested this hypothesis using Frizzled7 (FZD7) antibody-coated NSs (FZD7-NS) to treat TNBC cells that are characterized by hyperactive Wnt signaling mediated through overexpressed FZD7 transmembrane receptors. We targeted Wnt signaling because which is critical for disease progression.³⁰ Importantly, a major benefit of the NP platform designed here is that it binds the extracellular portion of FZD7 receptors to block activation by extracellular Wnt ligands, thus negating the need for NPs to enter cells to render therapeutic benefits. An overarching goal of this Chapter was to demonstrate that antibody-functionalized nanoparticles can exploit

multivalency for improved signal cascade interference over free antibodies, which may ultimately permit lower antibody dosages to be administered to study signaling pathways or to manage diseases. Another goal of this Chapter was to conduct a pilot study to assess the biodistribution and therapeutic efficacy of FZD7-NS in a murine model of lung-metastatic TNBC. All animal work conducted in this Chapter was performed under IACUC approval (protocol #1318). The work presented in this Chapter was published in: Riley RS, Day ES. Frizzled7 Antibody-Functionalized Nanoshells Enable Multivalent Binding for Wnt Signaling Inhibition in Triple Negative Breast Cancer Cells. *Small*. 2017; 13: 1700544.

5.1.1 Antibodies as Therapeutic Agents for Cancer Management

Antibodies have emerged as invaluable tools for the study and treatment of cancer because they can manipulate signaling pathways that drive cancer progression with high specificity.^{24,141} The advantage of using antibodies to manipulate cellular signaling rather than small molecule inhibitors, gene regulation agents, or peptides, is that they offer high specificity and stability, and they do not require cellular uptake to be effective. Further, antibody therapies provide an indirect means of gene regulation to inhibit oncogenic cell signaling. While antibodies can be designed to either agonize or antagonize specific receptors upon binding, they are most commonly used to obstruct pro-oncogenic signaling downstream of their targeted receptor by acting in an antagonistic manner.⁷⁵ Several targeted antibody therapies are currently used to treat breast cancer patients, including trastuzumab and pertuzumab that target HER2-positive breast cancers.¹⁴² However, two major challenges that hinder the clinical translatability of antibodies are that they are extremely expensive to produce and require high injected dosages that can yield adverse side effects, which limits their

therapeutic success.^{76,77} Therefore, the two main goals of this Chapter were to demonstrate that NPs can improve upon the therapeutic impacts of antibodies by enabling multivalent binding, and to provide an initial assessment of the ability of FZD7-targeted NPs to accumulate within TNBC lung metastases to slow disease progression.

5.1.2 Wnt Signaling Drives TNBC Progression and Lung Metastasis

The Wnt signaling pathway is a promising therapeutic target for TNBC because it has recently been revealed as a key driving force behind disease progression. Further, deregulated Wnt signaling is highly correlated with the formation of lung metastasis from TNBC, making it an attractive target to treat both primary tumors and metastatic lesions.^{10,143} Wnt signaling is a highly regulated process in healthy cells; normally, a destruction complex composed of adenomatous polyposis coli (APC), axin, glycogen synthase kinase-3 β (GSK-3 β), and casein kinase 1 (CK1) binds and phosphorylates β -catenin, leading to its constitutive degradation (Figure 5.1A).^{144–148} In contrast, Wnt signaling is activated in TNBC cells and other aggressive cancers when extracellular Wnt proteins, such as Wnt3a, bind Frizzled (FZD) and LRP 5/6 receptors that are amplified on the cell surface (Figure 5.1B). This recruits Dishevelled to the cell membrane and blocks GSK-3 β activity to stabilize β -catenin and limit its degradation. Once stabilized, β -catenin accumulates in the cytoplasm and enters the nucleus where it associates with Tcf/Lef proteins to activate the transcription of Wnt target genes including Axin2, Cyclin D1, and c-Myc. Of these genes, Axin2 is the global downstream transcriptional target and main indicator of Wnt activity.^{149–151} While Wnt hyperactivity in some cancers is due to mutations in the genes encoding β -catenin or APC,¹⁵² in TNBC it is mainly due to increased expression

of FZD7 receptors on the cell surface. In fact, FZD7 is overexpressed in 67% of TNBC tumors and is the only member of the 10 FZD family receptors that is significantly overexpressed.^{30,145,153} Accordingly, FZD7 provides an excellent biomarker for studying the effects of multivalent nanoparticle targeting on signal cascade interference and for suppressing Wnt signaling in TNBC.

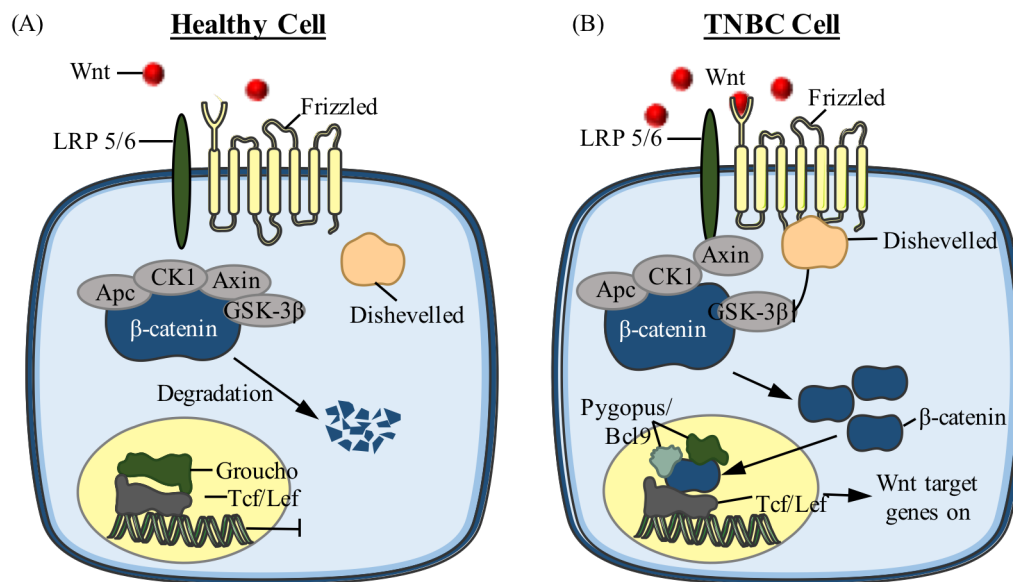


Figure 5.1: Schematic of the Wnt signaling pathway and validation of FZD7 overexpression in TNBC cells. (A) In healthy cells, extracellular Wnt proteins are minimally available to bind Frizzled and LRP5/6 coreceptors. When Wnt signaling is inactive, a destruction complex composed of Apc, Axin, and GSK-3 β continuously regulates β -catenin expression by enabling its phosphorylation and subsequent degradation by GSK-3 β and CK1. (B) In many cancers, including TNBC, extracellular Wnt proteins and Frizzled7 receptors are overexpressed, leading to hyperactive Wnt signaling. When Wnt proteins bind Frizzled and LRP5/6 coreceptors, Dishevelled is activated to inhibit the β -catenin destruction complex. Stabilized β -catenin accumulates in the cytoplasm and enters the nucleus to bind TCF/Lef transcription factors and activates Wnt target genes.

The potential of using FZD7 as a target for Wnt signaling inhibition and management of TNBC is supported by the fact that shRNA-mediated knockdown of

FZD7 decreased β -catenin stabilization and nuclear localization in TNBC cells.³⁰ Additionally, FZD7 antibodies have been proven effective against Wilms' tumor as a standalone therapy.¹⁵⁴ Further, Gurney *et al.* demonstrated that OMP-18R5, an antibody against 5 of the 10 FZD receptors, could inhibit Wnt signaling to decrease tumorigenicity and increase chemosensitivity in a variety of cancers.³³ Interestingly, OMP-18R5 is currently being evaluated in clinical trials in combination with chemotherapy.³¹ However, a limiting factor of antibody therapies to treat cancer is that the high required treatment dosages may be cost prohibitive and lead to adverse side effects. Since inhibiting Wnt signaling has been shown to be effective for cancer treatment, our goal in this work was to demonstrate that FZD7 antibodies conjugated to NSs are more effective than freely delivered FZD7 antibodies due to NP multivalency as described below. By capitalizing on multivalent binding effects to reduce the antibody dosage required for Wnt signaling inhibition, FZD7-NS could ultimately result in cheaper and safer treatment, making them an excellent platform for managing TNBC.

5.1.3 Antibody-Nanoparticle Conjugates for Active Tumor Targeting

In addition to having the therapeutic potential of FZD7-NS to inhibit Wnt signaling more effectively than freely delivered antibodies, FZD7-NS also offer the ability to enable active tumor targeting, as discussed in Chapter 1. Following intravenous administration, NPs accumulate within solid tumors *via* passive targeting that exploits the EPR effect. However, NPs that are not coated with targeting agents are not retained within tumor tissue for extended periods of time because they are cleared by the tumor lymphatics, and passively targeted NPs (i.e., NPs coated with PEG) are not efficiently taken up by cancer cells within the tumor.^{36,155-157} Coating NPs with

targeting moieties such as antibodies, aptamers, or peptides provides “active tumor targeting” capabilities that enable the NPs to specifically bind desired cancer cells within the tumor microenvironment. This active targeting increases NP retention within tumors and promotes cellular uptake of the NPs to enable longer lasting and more potent effects than achieved with passively targeted NPs.¹⁵⁷ In this sense, we hypothesized that FZD7-NS could enable active targeting of TNBC cells both *in vitro* and *in vivo* as well as enable signal cascade interference by binding FZD7 receptors in a multivalent manner to block their activation by Wnt ligands (Figure 5.2). In this Chapter, we evaluated this hypothesis both *in vitro* and *in vivo*. For the *in vivo* work, we performed a pilot study using an experimental murine model of lung-metastatic TNBC.

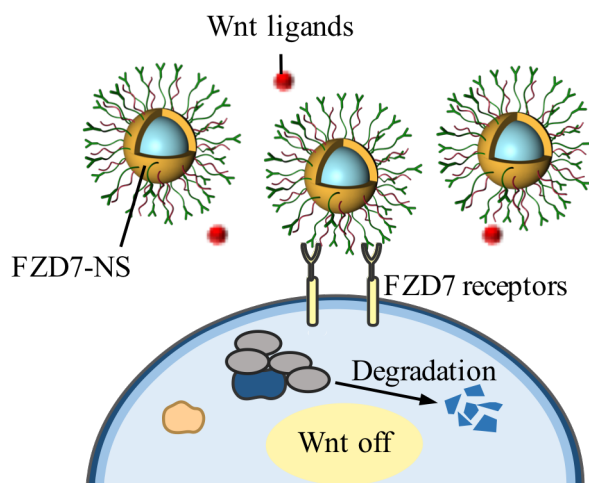


Figure 5.2: Wnt signaling inhibition by FZD7-NS. NSs coated with FZD7 antibodies (green) and poly(ethylene) glycol (purple) can bind FZD7 receptors multivalently to block extracellular Wnt activation by Wnt ligands (red), leading to the subsequent degradation of β -catenin.

5.1.4 Nanoparticle Multivalency Enhances Binding Avidity and Signal Cascade Interference

Antibody-NP conjugates can overcome many of the inherent limitations of naked antibodies by enhancing the target binding affinity due to multivalency, in which antibodies on NPs can engage multiple targeted antigens to increase the binding strength between ligand and receptor.¹⁵⁸ In fact, multivalency is recognized as a means to improve upon targeted therapeutics, such as antibodies, peptides, and aptamers, that have defined biological properties.⁸⁰ In this Chapter, we hypothesized that multivalent binding could be exploited to specifically bind targeted cells and thus yield enhanced oncogenic cell signaling inhibition relative to free antibody delivery. Therefore, the overarching goal of this Chapter was to demonstrate that FZD7-NS are more effective than freely delivered FZD7 antibodies, and to provide proof-of-concept that FZD7-NS could enable active targeting of TNBC lung metastases *in vivo*.

5.2 Materials and Methods

NSs were synthesized and functionalized with antibodies and mPEG-SH as explained in Chapter 2. For this work, NSs were coated with FZD7 antibodies or nonspecific isotype control IgG antibodies in addition to mPEG-SH. Prior to attachment of Ab-PEG conjugates to NS, antibodies were purified against 1X PBS at 4°C using microdialysis devices with a 10 kDa molecular weight cutoff (Spectrum Labs). Control NSs were coated with only mPEG-SH. DLS, Zeta potential, SEM, and UV-vis were conducted for NS characterization, and antibody loading was quantified by solution-based ELISAs as detailed in Section 2.3.3.

5.2.1 Cell Culture

MDA-MB-231 and BT20 TNBC cells were purchased from American Type Culture Collection (ATCC) and cultured in Dulbecco's Modified Eagle Medium (DMEM) or Eagle's Minimum Essential Medium (EMEM), respectively, each supplemented with 10% fetal bovine serum and 1% penicillin-streptomycin (Life Technologies). Non-cancerous MCF-10A breast epithelial cells were kindly provided by Dr. Kenneth Van Golen and were cultured in a 50:50 DMEM and F12 base medium supplemented with 5% FBS, 10 $\mu\text{g}/\text{mL}$ insulin, 0.5 $\mu\text{g}/\text{mL}$ hydrocortisone, 50 $\mu\text{g}/\text{mL}$ bovine pituitary extract, 20 ng/mL epidermal growth factor, and 100 ng/mL cholera toxin. Cells were cultured in T25 or T75 cell culture flasks and incubated at 37°C in a 5% CO_2 environment.

5.2.2 Immunohistochemical Staining of FZD7

MDA-MB-231, BT20, and MCF-10A cells were detached from cell culture flasks with trypsin-EDTA, plated in 24-well plates at 40,000 cells/well, and incubated overnight. Then, cells were fixed with 4% formaldehyde and rinsed 3X with PBS. Endogenous peroxidases were blocked with 3% hydrogen peroxide for 10 min and nonspecific protein interactions were blocked with 3% PBSA for 60 min. Mouse anti-human FZD7 antibodies (LifeSpan Biosciences) diluted in PBSA to 5 $\mu\text{g}/\text{mL}$ were added to each well and samples incubated overnight at 4°C. Anti-FZD7 antibodies were removed, samples were rinsed 3X in PBS, and then HRP-anti-mouse IgG (Sigma-Aldrich) diluted to 3 $\mu\text{g}/\text{mL}$ was added for 60 min at room temperature. Samples were rinsed 3X in PBS and 3-amino-9-ethylcarbazole (AEC, Sigma-Aldrich) was added for 20 min to stain bound HRP secondary antibodies. To stop the reaction, samples were rinsed with PBS. Stained cells were imaged on a Zeiss Axioobserver Z1

inverted fluorescence microscope using brightfield light capabilities and a color camera. This same microscope was used to image samples for all experiments except where indicated. IHC experiments were conducted at least three times, and at least three images were acquired per treatment group in each experiment.

5.2.3 Specific Binding of FZD7-NS to TNBC Cells

MDA-MB-231 and MCF-10A cells were detached from culture flasks with trypsin-EDTA, seeded at 100,000 cells/well in 8-well chambered coverglass and incubated overnight. Cells were treated with FZD7-NS or PEG-NS at 8.2×10^9 NS/mL (corresponding to an optical density (OD) of 3 at 800 nm), or with no NSs, in complete media for 4 h at 37°C and then rinsed 3X with PBS to remove unbound NSs. Cells were then fixed with 4% formaldehyde and imaged with a Zeiss LSM 510 NLO multiphoton microscope equipped with a pulsed Ti:sapphire laser. The laser was tuned to the peak resonance wavelength of the NSs (which was ~830 nm but varied by experiment since different NS batches have different resonance wavelengths), and cells were imaged with a 20X objective in combination with a long pass dichroic mirror. This experiment was repeated at least three times for each combination of cell type and nanoparticle type, and the sample wells were imaged in at least three locations.

5.2.4 Binding Avidity of FZD7-NS and Free FZD7 Antibodies

MDA-MB-231 cells were seeded at 15,000 cells/well in 96 well plates. Following overnight incubation, cells were fixed with 4% formaldehyde and rinsed with 1X PBS. Cells were treated with 3% hydrogen peroxide for 10 min, followed by 3% PBSA for 2 hr. FZD7-NS (0-7.36 nM antibody) or free FZD7 solutions (0-133.3

nM) were prepared in ultrapure water and were added to cells and incubated at room temperature for 1.5 hr. Samples were then washed 3X with PBST for 10 min each, and 2.5 $\mu\text{g}/\text{mL}$ HRP-anti-rabbit secondary antibodies (400X dilution) were added for 1 hr. After washing 3X with PBST for 15 min each, samples were developed in 3,3',5,5'-tetramethylbenzidine (TMB, Sigma-Aldrich) and then sulfuric acid was added to stop the reaction. Absorbance at 450 nm was measured on a Cary60 spectrophotometer and plotted versus FZD7 antibody concentration. Data was fit to a modified Langmuir isotherm model as described by Puig *et al.*¹⁵⁹ to find the effective dissociation constant using the equation $\text{OD} = \frac{\text{Ab}_{\text{conc}}}{K_{\text{D}}^{\text{eff}} + \text{Ab}_{\text{conc}}}$. In this equation, Ab_{conc} is the concentration of antibody added to cells and $K_{\text{D}}^{\text{eff}}$ is the effective dissociation constant. Further, OD is optical density at each antibody concentration normalized according to the equation $\text{OD} = \frac{\text{OD}_{\text{raw}} - \text{OD}_{\text{back}}}{\text{OD}_{\text{high}} - \text{OD}_{\text{back}}}$, where OD_{raw} is the initial optical density reading prior to any calculations, OD_{back} is the optical density of background signal (cells treated with no primary antibody and treated with secondary antibody), and OD_{high} is the optical density of the highest (saturated) signal. Binding affinity experiments were conducted with at least two replicates per antibody concentration, and the experiments were conducted three times.

5.2.5 Immunofluorescence Staining for β -catenin Expression

MDA-MB-231 cells were seeded at 30,000 cells/well in 8-well chambered coverglass, incubated overnight, and serum starved for 24 h. Then, cells were treated with FZD7-NS or PEG-NS at a density of 2.7×10^{10} NS/mL, or 50 $\mu\text{g}/\text{mL}$ free FZD7 antibodies for 6 h in serum free media. Wnt3a (125 ng/mL) was added for the final 4 h of the treatment period. Control samples received no NSs. Cells were rinsed 3X with PBS to remove unbound nanoparticles, fixed with 4% formaldehyde, and

permeabilized with 0.5% Triton-X in PBSA for 10 min. Next, samples were blocked with 10% PBSA for 30 min. Mouse anti-human β -catenin antibody (Santa Cruz) diluted to 2 $\mu\text{g}/\text{mL}$ in 1% PBSA with 0.01% Tween-20 (PBST) was incubated with cells overnight at 4°C. Samples were washed 3X with PBSA and incubated with AlexaFluor 488-conjugated goat anti-mouse IgG (ThermoFisher Scientific) diluted to 2 $\mu\text{g}/\text{mL}$ in PBST for 1 h at room temperature. Slides were mounted with Vectashield Antifade Mounting Medium with DAPI (VWR) and imaged under fluorescence microscopy on a Zeiss Axioobserver Z1 microscope with the EGFP (ex. 488 nm, em. 509 nm) and DAPI filter sets. β -catenin nuclear signal intensity was quantified in ImageJ software. First, the nuclear and β -catenin channels were split. A threshold was applied to the nuclear channel to define individual nuclei as regions of interest (ROIs). Then, the average nuclear intensity was analyzed in the β -catenin channel using the ROIs defined by the nuclear threshold. The images shown represent the mean fluorescence intensity across three replicates for each treatment group with 3 or 5 images acquired in each well. Although the exact number of cells in each field of view varied, we imaged at least 400 cells/treatment group in each experiment.

5.2.6 Western Blot Analysis for β -catenin or Frizzled7 Expression

Cells were lysed in RIPA buffer (Amersco) supplemented with Halt Protease Inhibitory Cocktail (Life Technologies) per the manufacturer's instructions. Lysate from untreated MDA-MB-231, BT20, and MCF-10A cells was used to assess baseline Frizzled7 expression. To assess β -catenin expression, MDA-MB-231 or BT20 cells were seeded at 50,000 cells/well in 24 well plates, incubated overnight, and serum starved for 24 h. Cells were treated in an identical manner as described for immunofluorescence staining experiments, and at least 3 experimental replicates were

completed. Following the 6 h incubation, cells were washed 1X with PBS and lysed in RIPA buffer (Amresco) supplemented with Halt Protease Inhibitor Cocktail (Life Technologies) per the manufacturer's instructions. Protein concentration was determined using a DC Protein Assay (BioRad). 10 μ g of protein was separated on 8% Bis-tris gels at 165V for 35 min. Then, the protein was transferred to nitrocellulose membranes for 12.5 min using the Pierce Power System (Thermo Scientific). Membranes were blocked for 90 min in tris buffered saline with 0.1% Tween-20 (TBST) and 5% BSA and then incubated with mouse anti-human β -catenin antibodies (Santa Cruz) diluted to 0.4 μ g/mL (1:500) or mouse anti-human Frizzled7 antibodies (Santa Cruz) diluted to 0.5 μ g/mL, in TBST with 5% BSA overnight at 4°C. Mouse anti-human β -actin diluted to 0.2 μ g/mL (1:5000) was used as the normalization control. After overnight incubation, membranes were washed 3X in TBST and incubated with HRP-anti-mouse IgG (Santa Cruz) diluted to 0.02 μ g/mL (1:5000) in TBST with 5% BSA for 1 h at room temperature. Membranes were washed 3X in TBST, followed by 1X in TBS (without Tween-20) and protein bands were visualized using an Amersham enhanced chemiluminescence detection solution (ECL, GE Healthcare). For the Frizzled7 western blot, membranes were incubated with stripping buffer (Amresco) for 30 min and rinsed 3X with TBST prior to incubation with the β -actin antibodies. In these experiments, the band densities were quantified in ImageJ, and the blot shown represents the average band density across experiments.

5.2.7 qRT-PCR Analysis for Axin2 mRNA Expression

MDA-MB-231 or BT20 cells were treated with free FZD7 antibodies, FZD7-NS, PEG-NS, IgG-NS, or no NSs in an identical manner to immunofluorescence experiments. Following the 6 h incubation, total RNA was extracted using the Isolate

II RNA Mini Kit (Bioline) per manufacturer instructions. PCR reactions were performed using the SensiFAST SYBR No-ROX One-Step Kit (Bioline). Reactions pre-incubated for 20 min at 48°C and then for 10 min at 95°C followed by 40 cycles of 95°C for 10 s, 60°C for 20 s, and 72°C for 20 s (Roche LightCycler 96). The primer sequences (Life Technologies) used for qRT-PCR were:

- (1) GAPDH Forward: ACAGTCAGCCGCATCTTCTT,
- (2) GAPDH Reverse: ACGACCAAATCCGTTGACTC,
- (3) Axin2 Forward: TTATGCTTTGCACTACGTCCCTCCA,
- (4) Axin2 Reverse: CGCAACATGGTCAACCCTCAGAC.

The Delta-Delta Ct method was used to calculate relative Axin2 mRNA expression, and the data shown are the means \pm standard deviations of triplicate experiments. Data was analyzed by ANOVA with posthoc Tukey.

5.2.8 Analysis of Cellular Metabolic Activity

MDA-MB-231 or BT20 cells were treated with free FZD7 antibodies, FZD7-NS, PEG-NS, IgG-NS, or no NSs in an identical manner to immunofluorescence experiments. After a 16 hr incubation, the NS and Wnt3a-containing media was replaced with AlamarBlue reagent (Thermo Fisher) per manufacturer instructions. After 4 hr, the samples' fluorescence was read on a Hybrid Synergy H1 plate reader, and data was normalized to untreated controls for each cell line. The data shown are the means \pm standard deviations of three individual experiments, each with 3 wells that were treated as biological replicates. The data was analyzed by one-way ANOVA with post hoc Tukey Kramer.

5.2.9 Formation of TNBC Lung Metastases and Nanoparticle Injections in Mice

MDA-MB-231 cells that were stably transfected with luciferase (luc-231) were kindly donated from Haifa Shen's lab at Houston Methodist. Female athymic nude mice (6 weeks old, 23 mice) were injected with 1×10^6 luc-231 cells suspended in saline *via* tail vein (Day 0). Mice were weighed and imaged on the *in vivo* imaging system (IVIS) twice per week starting 11 days after cell injections. During each imaging session, mice received intraperitoneal injections of 150 mg/kg d-luciferin diluted in saline and were imaged on the IVIS 10 min following injections using luminescence signal. Mice were imaged on days 11, 17, 25, 31, 41, 45, 49, 52, 55, and 58 during this study. Bioluminescent intensity in the lungs was quantified throughout the study using ImageJ software and instrument background from a mouse without lung tumors was subtracted for each time point. Once the majority of mice had detectable signal in the lungs (day 17), they were divided into two groups that received tail vein injections of 100 μ L saline or FZD7-NS at 1.6×10^{11} NS/mL (corresponding to OD60) on days 17, 20, 25, 39, 42, and 45. Only mice that grew lung tumors were included in the analyses presented here ($n=3$ for FZD7-NS and $n=4$ for saline). Mice were euthanized by carbon dioxide asphyxiation followed by cervical dislocation once the mouse with largest tumors reached the highest allowable luminescent intensity (day 46), and then the lungs, heart, femur, kidney, brain, intestine, spleen, liver, and blood were collected from each animal for histological and biodistribution analysis.

5.2.10 Hematoxylin and Eosin (H&E) Staining

Upon extraction, tissues were split into two parts for histology or inductively coupled plasma-mass spectrometry (ICP-MS). For histology, tissue sections were placed into cassettes and fixed in 4% paraformaldehyde in 1X PBS for 3 days at 4° C.

Then, sections were thoroughly rinsed with ultrapure water (3X, 10 min each) and stored in 70% ethanol until processing. Samples in cassettes were processed in a tissue processor (Sakura Finetek) and were then embedded in paraffin wax. Cassettes were mounted on a microtome and 5 μm sections were cut and placed onto charged glass slides (Globe Scientific) that were then baked overnight at 60° C. Tissue sections were deparaffinized through xylene twice for 5 min each and were then re-hydrated through ethanol diluted in water to 100% (twice, 5 min), 95% (once, 2 min), and 70% (once, 2 min). Then, slides were rinsed in ultrapure water and stained in Mayer hematoxylin for 8 min followed by bluing by rinsing in running tap water for 10 min. Slides were rinsed in 95% ethanol and were then counterstained in eosin Y (1.25 min) and dehydrated through 95% and 100% ethanol. Lastly, slides were placed into xylene (twice, 5 min) and mounted with xylene-based mounting medium. Slides were imaged under brightfield microscopy using a color camera on a Zeiss Axioobserver Z1 Inverted Fluorescent Microscope with the 10X or 20X objectives.

5.2.11 Inductively Coupled Plasma-Mass Spectrometry (ICP-MS) for Analysis of Gold Content in Tissues

The second half of each tissue was placed into a microcentrifuge tube that was weighed both empty and with the wet tissue. The sample tubes were frozen overnight at -80° C, lyophilized, and the dry weight of the tissue in the tubes was recorded. The dried samples were digested in 97% nitric acid and 3% hydrochloric acid (volume varied by tissue type) in a ventilated oven at 60° C overnight. Next, the samples were diluted in an acid matrix containing 2% nitric acid and 2% hydrochloric acid in ultrapure water (the dilution amount varied by tissue type), and a standard curve containing 0-100 ppb (parts per billion) gold was prepared. Samples were analyzed on

a Agilent 7500c ICP-MS instrument and the gold content in ppb was recorded for each sample. The gold content per gram of dried tissue was calculated by first subtracting instrument background obtained from mice treated with saline. Standard deviations represent variability in gold content in each tissue among mice treated with FZD7-NS.

5.3 Results

5.3.1 Nanoshell Characterization

NSs composed of silica cores (~120 nm) and thin gold shells (~15 nm) were synthesized according to previously published methods.¹⁶⁰ SEM images indicated the NSs had a highly monodisperse size distribution (Figure 5.3A). UV-visible spectrophotometry revealed the NSs had a peak plasmon resonance at 830 nm (Figure 5.3B), which is important for their use as contrast agents for multiphoton microscopy to assess cellular binding, as described in detail later. Note that Figure 2C displays the extinction of NSs from a single synthesis batch; the peak wavelength varied by several nanometers for each batch. For our studies, we developed three types of NS formulations: (1) NSs coated with FZD7 antibodies and methoxy polyethylene glycol-thiol (mPEG-SH) (FZD7-NS), (2) NSs coated with nonspecific IgG antibodies and mPEG-SH (IgG-NS), and (3) NSs coated with only mPEG-SH (PEG-NS). Antibody and mPEG-SH attachment to NSs was confirmed by dynamic light scattering (DLS), which showed increased hydrodynamic diameter and zeta potential upon functionalization compared to bare NSs (Figure 5.3C). Further, the peak plasmon resonance shifted ~20 nanometers following NS functionalization with antibodies, indicating successful conjugation. We conducted solution-based ELISAs to quantify

antibody loading on NSs, and NSs with loading of at least 40 antibodies/NS were used for experiments.

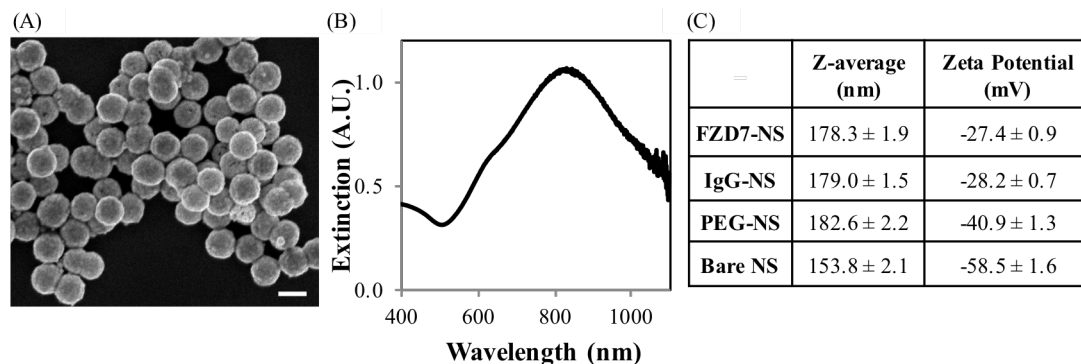


Figure 5.3: Characterization of FZD7-NS. (A) Scanning electron microscopy (SEM) image of bare nanoshells showing homogenous structure and complete gold shell. Scale bar = 150nm. (B) Plasmon resonant extinction spectra of nanoshells with peak absorbance at ~800 nm. (C) Dynamic light scattering (hydrodynamic diameter) and zeta potential measurements of nanoshell formulations.

5.3.2 TNBC Cells Overexpress FZD7 Receptors

We used MBA-MB-231 and BT20 TNBC cells, as well as MCF10A noncancerous breast cells, as models for our studies. Both MDA-MB-231 and BT20 cells are known to have overactive Wnt signaling mediated by FZD7 cell surface receptors.³⁰ We validated the relative FZD7 expression of these cells versus MCF10A cells by immunohistochemical (IHC) staining and Western blotting (Figure 5.4A,B). Consistent with literature,³⁰ we found that both MDA-MB-231 and BT20 cells express high levels of FZD7 relative to MCF10A cells, as indicated by the positive red stain in the IHC samples and by the amplified band density in Western blot samples.

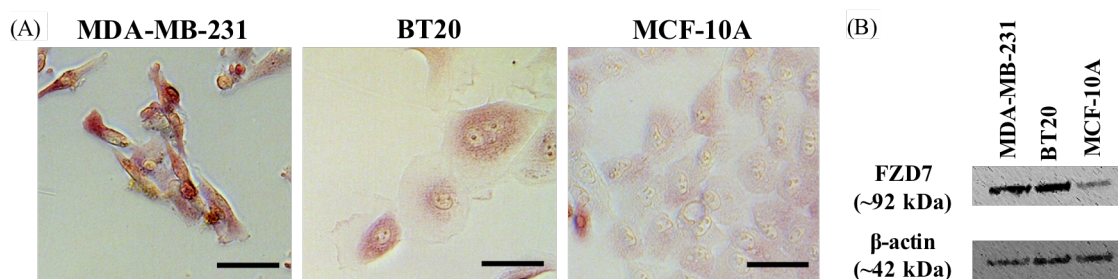


Figure 5.4: FZD7 expression in TNBC cells. (A) Immunohistochemical staining and (B) Western blotting of Frizzled7 expression (red in A) in MDA-MB-231 and BT20 TNBC cells versus non-cancerous MCF-10A cells. Scale bars = 50 μ m.

5.3.3 FZD7-NS Bind TNBC Cells with Higher Avidity than Free FZD7 Antibodies

We evaluated the ability of FZD7-NS and non-targeted NSs to selectively bind TNBC cells using two-photon microscopy (TPM), in which NSs act as natural contrast agents by emitting light in response to a pulsed near infrared (NIR) laser tuned to the peak NS plasmon resonance wavelength.¹⁶¹ Following a 4 h incubation with FZD7-NS, PEG-NS, or no NSs, TPM showed specific binding of FZD7-NS to TNBC cells but not to healthy cells, as indicated by the blue signal (Figure 5.5). As expected, PEG-NS did not bind either cell type.

To probe our hypothesis that FZD7-NS would bind TNBC cells with higher avidity than free FZD7 antibodies due to their multivalency, we employed a modified Langmuir isotherm model as described by Puig *et al.*, which describes the binding of a free ligand, in this case FZD7-NS or free FZD7 antibodies, to an immobilized antigen, such as cells fixed to a plate.¹⁵⁹ Using this model, we found an effective dissociation constant of 4.83E-10 M for FZD7-NS and 1.38E-8 M for free FZD7 antibodies (Figure 5.6). The lower effective dissociation constant for FZD7-NS compared to free FZD7 antibodies indicates that FZD7-NS have approximately a 100-fold increased binding avidity to FZD7 cell surface receptors relative to freely delivered FZD7

antibodies. The data shown in Figure 5.6 is representative from three individual experiments for both FZD7-NS and free FZD7 antibodies. The averaged dissociation constant among all three experiments was $4.9\text{E-}10 \pm 1.73\text{E-}10$ M and $1.48\text{E-}8 \pm 1.48\text{E-}9$ M for FZD7-NS and free FZD7 antibodies, respectively. This study was critical since minimal research has investigated how increased binding avidity from antibody-nanoparticle conjugates correlates with oncogenic cell signaling blockade. Next, we investigated how this increased binding avidity correlates to Wnt signaling inhibition.

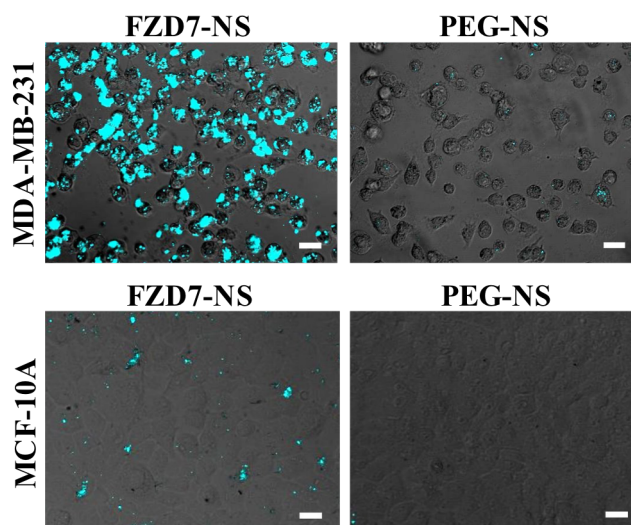


Figure 5.5: Two-photon microscopy showing binding capacity of FZD7-NS and PEG-NS (blue) to MDA-MB-231 and MCF10A cells, which express high and low levels of Frizzled7, respectively. Scale bars = 25 μ m.

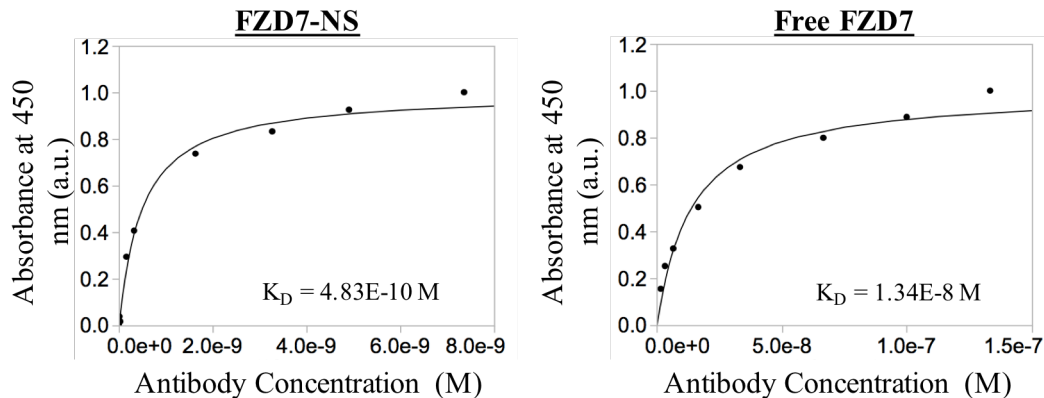


Figure 5.6: Effective dissociation constant of FZD7-NS (left) and free FZD7 antibodies (right) to MDA-MB-231 cells. Data was fit to a modified Langmuir isotherm model.

5.3.4 FZD7-NS Suppress Wnt Signaling in TNBC Cells More Effectively than Free FZD7 Antibodies

Since FZD7-NS could specifically bind TNBC cells with higher avidity than free FZD7 antibodies, we hypothesized that they could also manipulate Wnt signaling more effectively than free antibodies. To investigate this, we co-treated TNBC cells with either FZD7-NS, free FZD7 antibodies, PEG-NS, IgG-NS, or no NSs and the extracellular Wnt ligand Wnt3a. Overactive Wnt signaling is often due to extracellular Wnt proteins, particularly Wnt3a, that are available to bind overexpressed FZD7 receptors on TNBC cells.^{30,153} We determined the optimal concentration of Wnt3a to activate Wnt signaling by analyzing β -catenin expression in cells exposed to various concentrations of Wnt3a (Figure 5.7A) and found that β -catenin levels are maximized in MDA-MB-231 cells treated with at least 125 ng/mL Wnt3a. Since Wnt3a activates Wnt signaling through FZD7 receptors, we hypothesized that FZD7-NS would competitively bind FZD7 receptors in place of Wnt3a ligands to block Wnt stimulation and ultimately reduce β -catenin and Axin2 expression levels. Further, we expected FZD7-NS to be more effective at inhibiting Wnt signaling compared to free

FZD7 molecules, due to their enhanced binding avidity. As mentioned above, we treated MDA-MB-231 cells with FZD7-NS, PEG-NS, IgG-NS, free FZD7 antibodies, or no NSs for 6 h and added 125 ng/mL Wnt3a for the final 4 h of the incubation to competitively bind FZD7 receptors. Importantly, free FZD7 antibodies were added to cells at 50 $\mu\text{g}/\text{mL}$, which is approximately 50-fold more antibody than in cells treated with FZD7-NS. Western blotting revealed that cells treated with FZD7-NS had lower β -catenin protein levels than cells treated with free FZD7 antibodies (representative Western blot shown in Figure 5.7B). Comparing band densities from cells treated with IgG-NS relative to cells treated with PEG-NS revealed that both control NS types do not influence β -catenin levels to the same extent as FZD7-NS (Figure 5.7B).

The impact that FZD7-NS have on β -catenin levels was confirmed by immunofluorescence staining, which showed lower cytoplasmic and nuclear levels in cells treated with FZD7-NS compared to free antibody, PEG-NS, or no NS (Figure 5.7C). In this data, β -catenin was stained green with Alexa Fluor 488-conjugated secondary antibodies that bound to anti- β -catenin primary antibodies and nuclei were stained blue with DAPI. The images shown represent the average β -catenin nuclear fluorescence intensity in each treatment group from three individual experiments as quantified using ImageJ software (detailed analysis provided in the Experimental section). In these experiments, cells treated with free FZD7 antibodies were exposed to 50 $\mu\text{g}/\text{mL}$ antibody, which is approximately 50X excess antibody compared to cells treated with FZD7-NS, demonstrating that multivalency plays a critical role in nanoparticle-mediated signal cascade interference. Interestingly, both immunofluorescence staining and Western blotting demonstrate that cells treated with PEG-NS may experience a modest effect on β -catenin levels compared to no NSs.

This indicates that NSs alone may have an effect on Wnt signaling at the concentrations used in these experiments, although not to the same extent achieved when the NSs are coated with FZD7 antibodies. This is not surprising given that NPs can inherently influence cell signaling processes.^{162,163} Regardless, the anti-FZD7 functionalization enables FZD7-NS to specifically bind TNBC cells overexpressing FZD7 receptors and results in greater knockdown of β -catenin than PEG-NS, ensuring that the effect is FZD7/Wnt-specific.

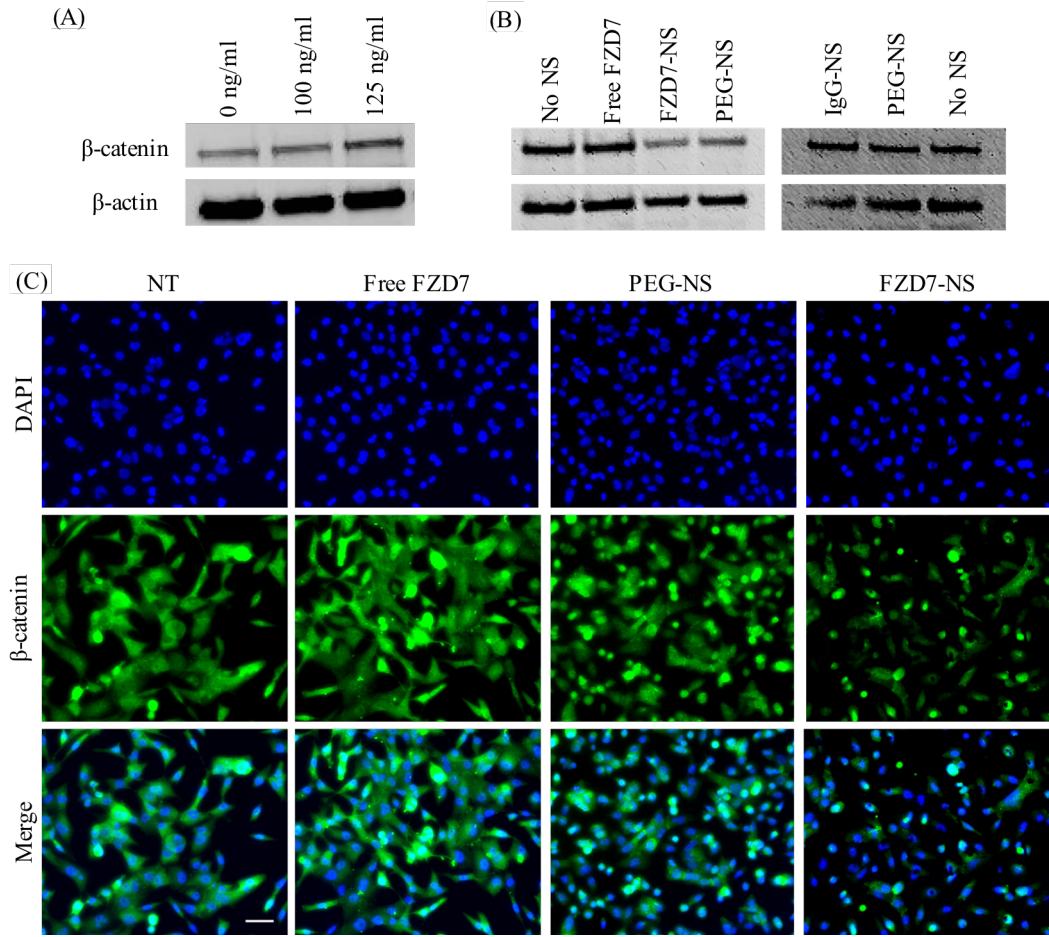


Figure 5.7: FZD7-NS mediated inhibition of β -catenin. (A) Western blotting showing β -catenin expression following treatment with 0, 100, or 125 ng/ml Wnt3a for 4 hr. (B) Representative Western blots and (C) immunofluorescence analysis showing β -catenin expression in MBA-MB-231 cells following treatment with free FZD7 antibodies, FZD7-NS, PEG-NS, or no NSs in the presence of 125 ng/ml Wnt3a. Scale bar=50 μ m.

To confirm that FZD7-NS directly inhibit Wnt signaling specifically, we also investigated the effect of treating MDA-MB-231 and BT20 cells with FZD7-NS, IgG-NS, PEG-NS, or free FZD7 antibodies on the universal downstream Wnt target Axin2. The expression of Axin2 is often measured to assess activation or depletion of Wnt activity, as this avoids common experimental issues when studying β -catenin.¹⁶⁴ Accordingly, Axin2 is considered the definitive marker of Wnt signaling activity. In TNBC cells, Axin2 expression is upregulated compared to healthy cells, particularly when activated by Wnt3a; in our studies, treatment with 125 ng/mL Wnt3a resulted in an 8.2-fold increase in Axin2 expression (Figure 5.8A).¹⁶⁴ We found that both TNBC cell lines that were co-treated with FZD7-NS and Wnt3a experienced a ~60% decrease in Axin2 mRNA expression compared to untreated cells, indicating significant downstream Wnt inhibition (Figure 5.8B, * and # indicate $p < 0.05$ by ANOVA with post-hoc Tukey-Kramer, $n=3$). Cells treated with free FZD7 antibodies (at ~50X excess antibodies), IgG-NS, or PEG-NS experienced minimal effects on Axin2 mRNA expression relative to untreated cells.

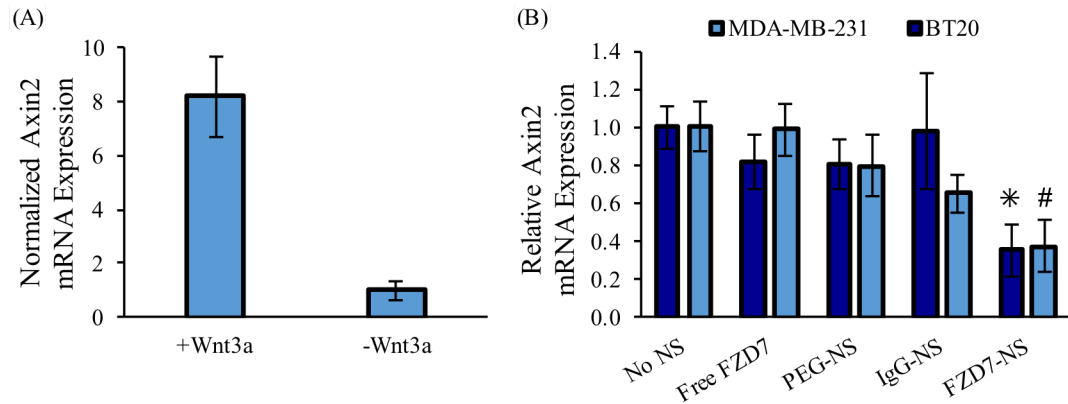


Figure 5.8: Axin2 expression following treatment. (A) qRT-PCR analysis of Axin2 mRNA expression in MDA-MB-231 cells following exposure to 125 ng/ml pr 0 ng/ml Wnt3a for 4 h. (B) qRT-PCR analysis of Axin2 mRNA expression in MDA-MB-231 and BT20 cells following treatment with free FZD7 antibodies, FZD7-NS, PEG-NS, IgG-NS or no NSs for 6 hr. Cells were in the presence of 125ng/ml Wnt3a for the final 4 hr of treatment. By one-way ANOVA with posthoc Tukey-Kramer (#) indicates $p < 0.05$ compared to cells treated with PEG-NS, free FZD7, and no NSs, and (*) indicates $p < 0.05$ compared to cells treated with IgG-NS or no NSs.

5.3.5 FZD7-NS Suppress Metabolic Activity of TNBC Cells

We investigated how inhibited Wnt signaling influences cell viability by treating MDA-MB-231 cells with FZD7-NS, IgG-NS, PEG-NS, or no NSs and Wnt3a. We assessed cell viability using an Alamar blue assay, which measures the cells' metabolic activity. Since Wnt signaling is critical for TNBC cell proliferation and disease progression, we anticipated that FZD7-NS would decrease cell viability by blocking Wnt signaling activation. After a 16-hr incubation with each treatment group, we found that FZD7-NS decreased cell viability ~25% relative to controls (Figure 5.9), which is substantial given that 16-hr is less than one doubling time for the cell lines evaluated. We did not see significant decreases in cell viability in any control groups, including cells treated with an excess of free FZD7 antibodies, which indicates that nanoparticle multivalency is playing a critical role for Wnt signaling inhibition and cell growth. To confirm our *in vitro* results and to ensure that FZD7-NS can

induce a therapeutic benefit on TNBC by decreasing cell viability, we next performed a pilot *in vivo* study in a murine model of metastatic TNBC.

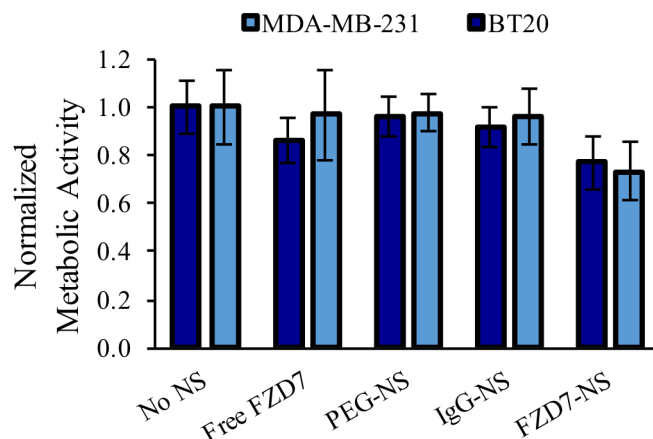


Figure 5.9: Cell viability analysis 16 hr post-treatment with FZD-NS, IgG-NS, PEG-NS, free FZD7 antibodies, or no NSs. (#) $p < 0.05$ compared to cells treated with IgG-NS, PEG-NS, free FZD7 antibodies, or no NSs. (*) $p < 0.05$ compared to cells treated with IgG-NS, PEG-NS, and no NSs by one way ANOVA with post hoc Tukey-Kramer.

5.3.6 A Pilot Study Indicates that FZD7-NS can Enter TNBC Lung Metastases to Slow Tumor Growth

We employed a lung metastatic TNBC model for a pilot *in vivo* investigation of FZD7-NS because Wnt signaling in TNBC is highly correlated with lung metastasis. We hypothesized that FZD7-NS could accumulate within small lung metastases and be well retained due to active targeting, which in turn would inhibit tumor growth via Wnt signaling inhibition. In this model, Luc-231 TNBC cells are injected into athymic female mice *via* tail vein and small lung lesions begin forming within just 2 weeks following injection (a therapeutic schedule is shown in Figure 5.10). Mice were imaged by IVIS twice per week following cell injection, and FZD7-NS or saline were injected starting 2 weeks after cell injections once the majority of mice had detectible luminescence signal in their lungs. We found that mice treated

with FZD7-NS had substantially lower overall luminescence in their lungs over the course of the study compared to mice treated with saline (Figure 5.11). Two mice treated with FZD7-NS did not form tumors throughout the study and were thus excluded from the analysis. Of the remaining three mice treated with FZD7-NS, two experienced slower tumor growth than the saline-treated mice, and one mouse experienced a loss in luminescent signal from the lungs throughout the study, indicating tumor regression. Further, three of the four mice treated with saline experienced substantial lung tumor growth throughout the study. The results of this pilot study indicate that FZD7-NS may have substantial potential as a treatment for lung metastatic TNBC. To ensure that the reduced growth of lung metastases in the FZD7-NS treated mice resulted from FZD7-NS accumulating the metastatic nodules, we next assessed the biodistribution of FZD7-NS in these mice.

5.3.7 H&E Staining of Lung Sections and Biodistribution of FZD7-NS

Vital organs were collected from all the animals and split into two sections for H&E staining or ICP-MS for histological or quantitative gold analysis, respectively. Lungs were visually assessed for small tumor lesions, which appear as darker red spots or large bumps by eye (Figure 5.12A). H&E staining of healthy lung appears as a highly organized network (Figure 5.12B, left), and lung tumors are apparent in H&E stained sections as large clumps of cells with larger nuclei than the healthy surrounding tissue (Figure 5.12B, right).

The ability to easily visualize lung tumors by H&E staining enabled us to assess FZD7-NS distribution within small lung lesions. Mice treated with FZD7-NS show dark contrast (black spots) within small lung tumors, indicating that FZD7-NS are accumulated within these areas (Figure 5.13A), but not within the healthy

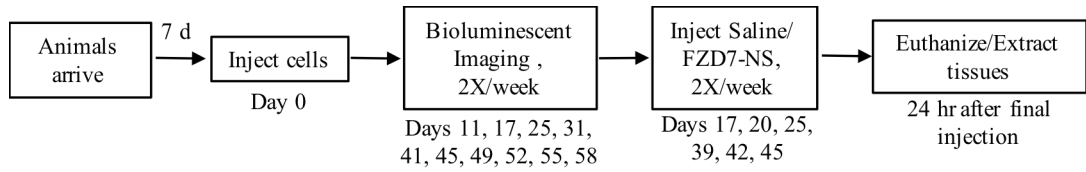


Figure 5.10: Timeline of the pilot in vivo study to investigate the use of FZD7-NS to treat lung metastatic TNBC in mice.

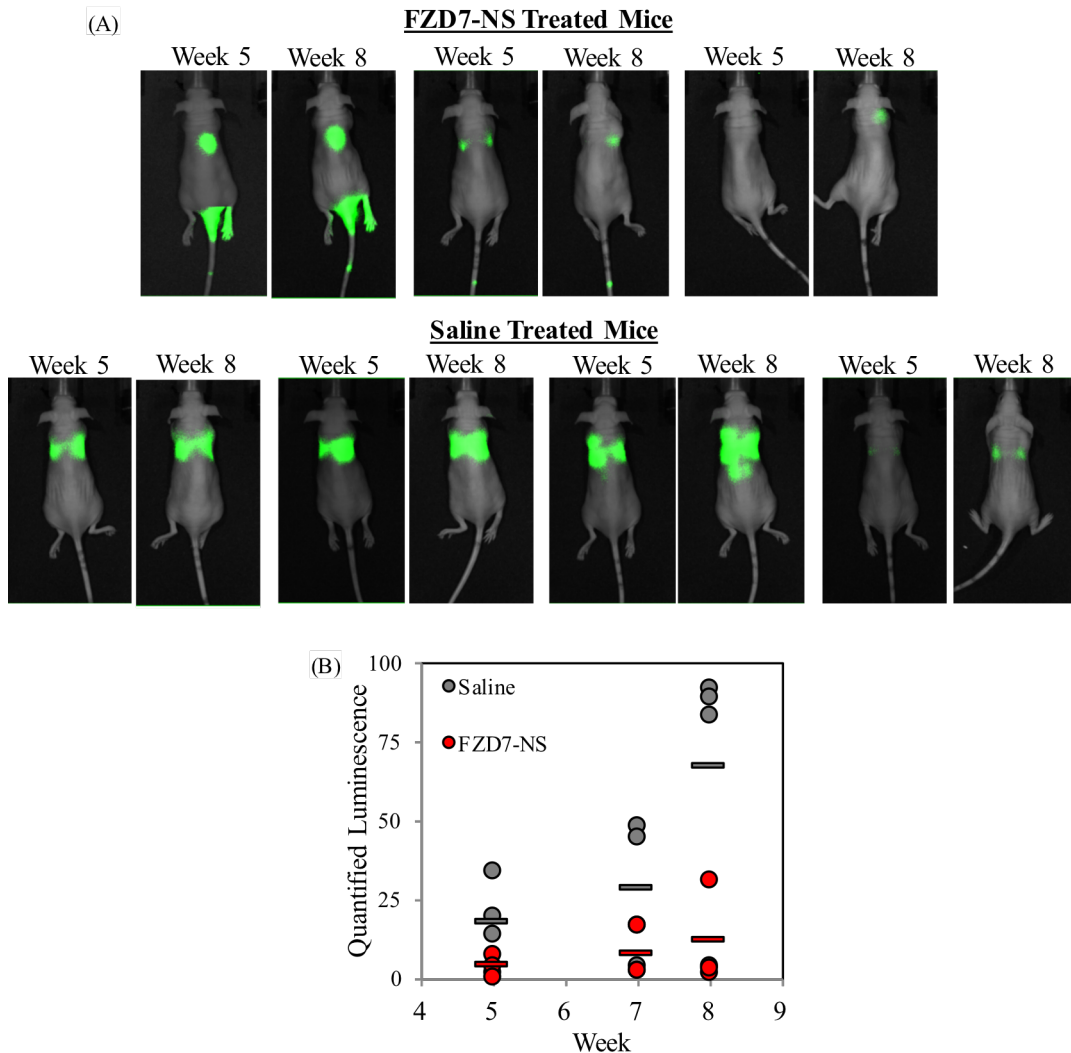


Figure 5.11: Analysis of tumor growth. (A) Bioluminescent images of mice treated with FZD7-NS or saline at Weeks 1, 5 and 8. (B) Overall luminescence intensity quantification at Weeks 5, 7, and 8 for mice treated with FZD7-NS or saline.

surrounding tissue. These results were confirmed by ICP-MS, which showed that FZD7-NS mostly accumulate within the liver, spleen, and lungs compared to other tissues. The observation that FZD7-NS accumulate in the lungs to similar extents as the liver and spleen is impressive given that most NP platforms have much higher accumulation in the liver and spleen compared to the lungs.¹⁶⁵ Together, our ICP-MS and H&E staining results indicate that FZD7-NS can actively target FZD7-expressing TNBC metastases in the lung to inhibit tumor growth, and future studies should compare inhibition of tumor growth with free FZD7 antibodies as described in Section 5.5 and also evaluate this therapy in a larger scale study.

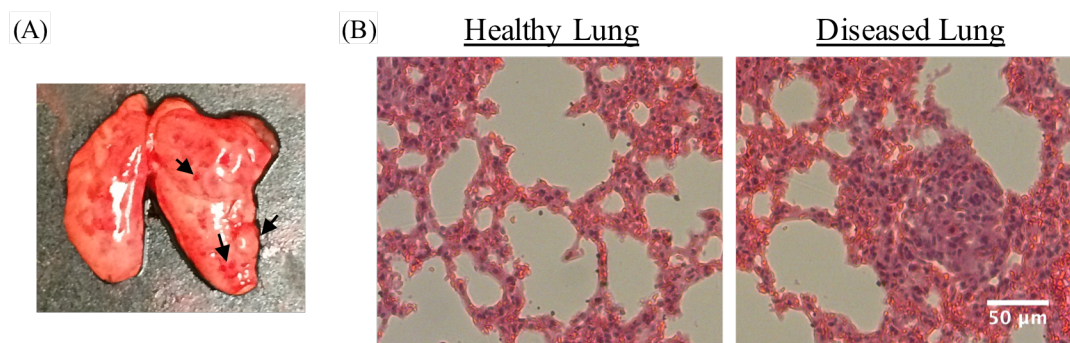


Figure 5.12: Lung tumors in murine model of metastatic TNBC. (A) Photograph of lungs with or without MDA-MB-231 tumors. Dark spots indicate small lung metastases. (B) Hematoxylin and eosin (H&E) staining of lung tumor sections.

5.4 Discussion

Since Wnt ligands bind FZD7 receptors to initiate Wnt signaling in TNBC cells, our overarching hypothesis in this Chapter was that NSs coated with FZD7 antibodies could competitively bind these receptors to block extracellular Wnt activation, leading to the destabilization of β -catenin and decreased Axin2 expression. Further, we expected that FZD7-NS would have an amplified inhibitory effect on Wnt signaling relative to unconjugated FZD7 antibodies due to multivalency, resulting in increased binding avidity towards FZD7 receptors. Finally,

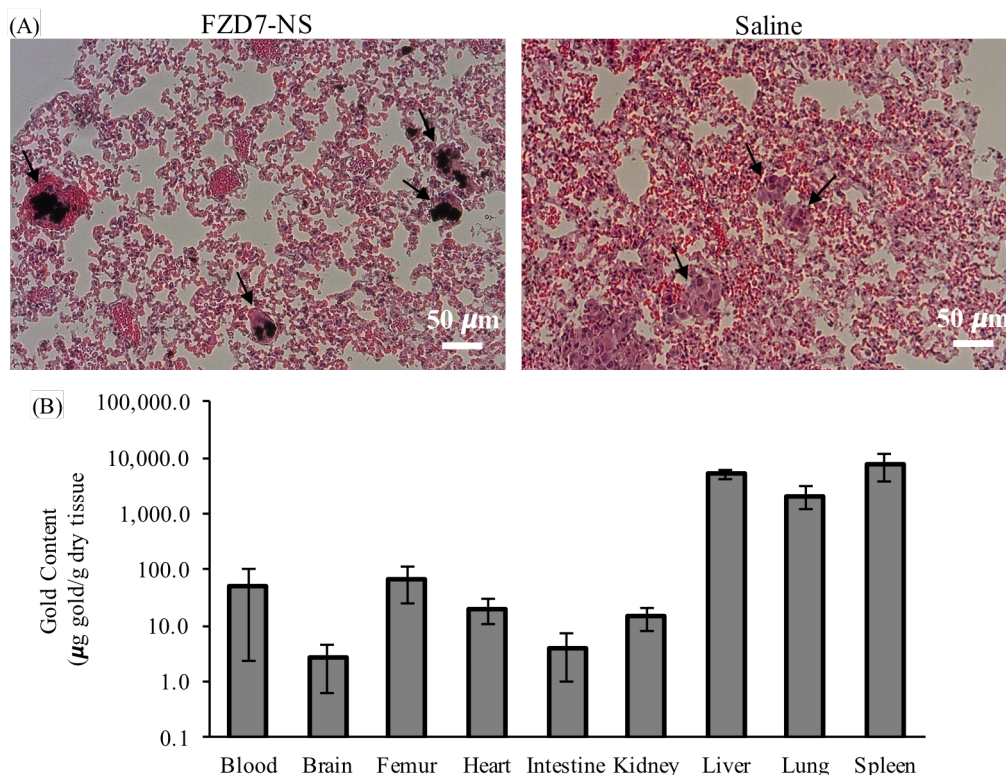


Figure 5.13: NS biodistribution in lung tumors. (A) Brightfield imaging of lung sections from mice treated with FZD7-NS (left) or saline (right). NSs appear as black areas. (B) Gold accumulation in mouse tissues by ICP-MS.

we anticipated that FZD7-NS could actively target lung metastases *in vivo* to inhibit tumor growth.

While our studies focus on using FZD7-NS to manipulate Wnt signaling in TNBC, from a broader perspective they provide important insight into the role of multivalency in signal cascade manipulation. The ability to enhance tumor cell-specific binding or internalization of NPs with targeting agents like antibodies has been thoroughly investigated,^{166,167} but only recently have researchers begun to examine the impact of these targeted NPs on downstream signaling events.^{168,169} These studies are important because cell signaling manipulation by targeted nanoparticles is

recognized as a promising therapeutic technique.⁷⁸ Researchers have evaluated the ability for functionalized or loaded NPs to initiate therapeutic benefits over their naked constituents using a variety of agents including RNAs, drugs, or peptides.^{156–158,170–173}

In this work, we used antibodies to study signal cascade interference because they offer high specificity and stability, and they do not require cellular uptake to be effective. The findings we report here contribute to an exciting new era of investigation regarding the use of antibody-functionalized NPs to block interactions between cancer cell receptors and their native ligands in the tumor microenvironment.

In summary, we developed and evaluated FZD7-NS to demonstrate that antibodies conjugated to the surface of NSs can exploit the multivalent binding effects afforded by nanocarriers relative to free antibodies in order to potently manipulate downstream gene expression. The ability to inhibit oncogenic signaling cascades, such as Wnt signaling, with ligand-targeted NPs is an underexplored area in the field of nanomedicine. Our *in vitro* data indicate that using targeted NPs to block native ligands from binding their intended receptors has substantial promise as a therapeutic strategy. Further, we show that using nanocarriers as delivery agents leads to enhanced signaling impacts with lower doses compared to free antibody delivery. These findings support further development of NPs functionalized with ligands that elicit known cell signaling responses to improve upon their therapeutic capabilities. The success of many antibody therapies used clinically to treat cancer is limited by high required dosages, which make treatment expensive and may lead to adverse side effects. As demonstrated here, antibodies conjugated to nanoparticles may lead to lower required dosages and therefore fewer side effects than freely delivered antibodies. Ultimately, this approach may be applied to a wide range of NP cores functionalized with various

antagonistic antibodies to enhance disease management. Further, our *in vitro* results provide a basis to study the translatability of FZD7-NS as a treatment for TNBC *in vivo*.

Our pilot *in vivo* study demonstrates the therapeutic potency of Wnt signaling inhibition using FZD7-NS to treat lung metastatic TNBC. The IVIS and biodistribution results presented here confirmed our *in vitro* active targeting data and viability results, as mice treated with FZD7-NS had decreased metastatic growth as determined by luminescence measurements compared to mice treated with saline. While our H&E staining data show that FZD7-NS can efficiently penetrate small metastatic nodules in the lung, future work should assess injection dose and timing to maximize delivery to large lung tumors. The results presented in this Chapter agree with literature that demonstrates Wnt signaling is a driving force behind growth of TNBC lung metastases.¹⁰ For example, Dey *et al.* investigated the level of Wnt activity in human TNBC samples and found that upregulated Wnt signaling increased the risk of lung metastases.¹⁰ Our *in vitro* and *in vivo* results demonstrating the impact of FZD7-NS on TNBC cells and tumors, respectively, support further assessment of FZD7-NS as a treatment for lung metastatic TNBC.

The results presented here support the continued development of antibody-functionalized nanoparticles for signal cascade interference in TNBC that is driven by aberrant Wnt signaling. Ultimately, our results suggest that antibody-NP conjugates may be useful alternatives to freely delivered antibodies in both fundamental biological studies and treatment strategies that require active NP targeting and efficient signal cascade interference.

5.5 Future Work

In this Chapter, we show that FZD7-NS are significantly more effective at inhibiting Wnt signaling than freely delivered FZD7 antibodies. Our results provide multiple opportunities to further understand the therapeutic potential of antibody-NP conjugates and particularly Wnt signaling-targeted NPs. First, the loading density of antibodies on the surface of NPs is likely to impact the binding avidity and subsequent ability of the NPs to inhibit cell signaling. This idea stems from the fact that ligand density is known to influence binding avidity towards the targeted cell surface receptor.¹⁷⁴ Further, Jiang *et al.* showed that NP size impacts binding and subsequent internalization of NPs.⁷⁸ Thus, the binding, internalization, and subsequent therapeutic impact of targeted NPs depends on both NP size and loading density. Accordingly, the antibody loading density on FZD7-NS could be further optimized to maximize their therapeutic potential. In this study, we used NPs coated with 40-100 antibodies/NS; no quantifiable differences in Wnt signaling inhibition were recorded, but larger antibody loading ranges should be investigated to evaluate the cost-benefit relationship between antibody loading density and therapeutic results. Additionally, we anticipate that *in vivo* studies that compare the biodistribution of NPs with various loading densities would provide invaluable information regarding the relationship between antibody loading and subsequent therapeutic impacts.

The *in vitro* studies presented here provide opportunities to further study the mechanisms of action of FZD7-NS at the cellular level. Although we did not evaluate the mechanism of cellular uptake of FZD7-NS here, such studies can be beneficial moving forward. For example, it is known that antibodies can induce cell internalization of their targeted receptor upon binding.¹⁷⁵ Upon FZD7 antibody binding, FZD7 receptors in particular have been shown to be internalized by cells and

then recycled back to the cell membrane.¹⁵⁴ Thus, antibody-receptor interactions can influence the endocytosis pathway by which NPs can enter cells to avoid entrapment within intracellular compartments such as endosomes, which often hinders the ability for gene regulatory NPs to be active inside cells. By studying and understanding the mechanism of uptake of FZD7-NS, we anticipate that our platform can be used to enable the uptake of gene regulatory agents that require cytosolic delivery, such as siRNA. In this way, we could develop a multifaceted approach to regulate cell signaling by enabling both upstream (through antibody-receptor interactions) and downstream impacts (through direct gene regulation by RNAi). This strategy could also be useful to manipulate either one or several oncogenic signaling pathways simultaneously.

Finally, the results acquired from the pilot *in vivo* study conducted here provide several opportunities for future work to more thoroughly examine the clinical potential and translatability of FZD7-NS. First, a study with larger sample sizes should be performed to enable statistical analysis of IVIS and biodistribution data to confirm the therapeutic impacts and tumor penetration of FZD7-NS. Further, although the work presented here shows that FZD7-NS can actively target TNBC tumors in the lungs to inhibit tumor growth, future work should investigate the direct impact of FZD7-NS on Wnt signaling within these lung tumors, to validate their mechanism of action. These future studies should also compare FZD7-NS to free FZD7 antibodies to confirm the benefits observed *in vitro* as presented in this Chapter. As previously mentioned, the timing and dosing of treatment with FZD7-NS is also of the utmost importance for future study, as well as analysis of the particles' ability to penetrate

large tumor nodules. Overall, these proposed follow-up studies would provide valuable insight towards clinical translation.

5.6 Conclusions

In this work, we developed NSs coated with FZD7 antibodies and mPEG-SH to study the effects of nanoparticle multivalency on signal cascade interference to antagonize the Wnt signaling pathway. We show that FZD7-NS bind TNBC cells sufficiently to reduce β -catenin and Axin2 expression, as evidenced by immunofluorescence staining, Western blotting, and qRT-PCR. More specifically, cells treated with FZD7-NS in the presence of 125 ng/mL Wnt3a experienced ~60% decrease in Axin2 expression relative to untreated cells, indicating significant inhibition of the Wnt signaling pathway. This inhibited Wnt signaling resulted in ~25% decrease in cell viability only 16 hr post treatment with FZD7-NS. Excitingly, the Wnt inhibitory effects of FZD7-NS were much greater than those observed when cells were treated with 50-fold more free FZD7 antibodies. We attribute the enhanced Wnt inhibitory effects of FZD7-NS relative to free FZD7 antibodies to their multivalency, as we found that FZD7-NS bind TNBC cells with effective binding avidities two orders of magnitude higher than free FZD7 antibodies. Together, these results indicate that binding strength correlates to enhanced signaling inhibition and therapeutic effects, and that antibody-NP conjugates may overcome the dose limitations of free antibody therapeutics. To investigate the therapeutic potential of FZD7-NS, we conducted a pilot *in vivo* study to evaluate tumor growth and biodistribution in an experimental murine model of lung metastatic murine TNBC model. We found that FZD7-NS can accumulate in small lung tumors and slow tumor progression. Future *in vivo* studies with more complex tumor models will need to be

performed to validate the therapeutic implications of multivalent binding compared to free FZD7 antibodies. Additional studies that investigate the role of nanoparticle size on the ability to suppress oncogenic signaling with antibody-NP conjugates would provide important insight to structure/function relationships of these nanomaterials. As our studies demonstrate that antibody-NP conjugates offer substantial benefits over freely delivered antibodies, this work supports further development of functionalized NPs to actively target diseased cells and to control aberrant signaling pathways implicated in disease progression.

Chapter 6

CONCLUSIONS

In this chapter, we summarize the importance of the findings presented throughout this dissertation and we discuss the opportunities and challenges faced by cancer nanomedicine moving forward. Some text in this chapter has been adapted from my co-authored articles:

- (1) Riley RS, Day ES. Gold Nanoparticle-Mediated Photothermal Therapy: Applications and Opportunities for Multimodal Cancer Treatment. *WIREs Nanomed Nanobiotechnol* 2016, e1449.
- (2) Valcourt DM, Harris J, Riley RS, Dang M, Wang J, Day ES. Advances in Targeted Nanotherapeutics: From Bioconjugation to Biomimicry. *Nano Research* 2018, 3, 1-18.

6.1 Nanoshells as Comprehensive Platforms for Cancer Therapy

Standard cancer treatment options, including surgery, radiation, and chemotherapy, have remained relatively unchanged over the past several decades. Although these regimens are effective for certain cancers, their use is associated with significant adverse effects and inconsistent success. This is because these standards-of-care procedures are not targeted, so they impact both diseased and healthy tissues. Targeted therapies, such as monoclonal antibodies, have emerged as promising alternatives to non-targeted therapies, but their clinical utility is still limited by dose-limiting toxicities and high production costs. Towards our overarching goal of

developing novel therapies for aggressive cancers, we evaluated silica core/gold shell NSs as alternatives to currently used cancer therapies in three independent treatment strategies to mediate phototherapies and/or gene regulation.

In Chapter 3, we showed that our novel photosensitizer, Pd[DMBi1]-PEG₇₅₀, is substantially safer and more efficacious than commercially available photosensitizers for mediating PDT. Further, we investigated a new therapeutic approach combining PEG-NS and Pd[DMBi1]-PEG₇₅₀ for PTT and PDT, respectively, with the anticipation that dual therapy would overcome the limitations of each individual option. For example, PDT is ineffective in hypoxic regions of tumors, and photosensitizers are typically activated by low wavelengths of light that cannot penetrate tissue. Alternatively, PTT is effective throughout the entirety of the tumor and uses NIR light, but it is typically used to induce necrotic, rather than apoptotic, cell death. We showed that dual therapy is 22% more effective at inducing apoptotic cell death than either therapy alone with a high level of synergy between the two therapies. Moving forward, this strategy should be evaluated *in vivo* to establish the relationship between the two therapies in solid tumors and to prove clinical translatability.

Chapter 4 investigates siRNA-NS conjugates for on-demand gene regulation upon exposure to pulsed NIR laser light. In this work, we thoroughly characterized the siRNA released from NSs and we showed that pulsed laser irradiation primarily releases duplexes of siRNA that retain their functionality. We also demonstrated that cells treated with GFP-NSs and irradiated with low pulsed laser powers experience a 35% reduction in GFP expression compared to control cells. In these experiments, we delivered on average only 15 nM siRNA on NSs, which is ~6.6X less siRNA

compared to transfections using commercial reagents. These results prove that siRNA-NS conjugates serve as potent siRNA delivery systems to enhance gene regulation only in diseased cells, while leaving healthy cells unharmed. On a broader scale, this technology can be easily adapted to silence oncogenic cell signaling by changing the conjugated siRNA to silence overactive genes important for disease progression.

In Chapter 5, NSs are coated with FZD7 antibodies for active targeting, increased binding affinity, and Wnt signaling interference. We show that FZD7-NS conjugates have 100-fold higher binding affinity compared to free antibodies, and this correlates to a 60% reduction in Axin2 compared to untreated cells. Further, our pilot *in vivo* data show that actively targeted NSs can accumulate within small metastatic lung tumors in mice. Interestingly, mice treated with FZD7-NSs experienced substantially decreased disease progression compared to mice treated with saline. Together, the results presented in Chapter 5 show that the high binding affinity afforded by antibody-NP conjugates is correlated with enhanced signaling cascade interference compared to free antibodies, and our actively targeted platform can inhibit tumor growth. This indicates that NPs can enable lower treatment dosages to be administered to patients, thus lowering the associated costs and adverse side effects.

This dissertation shows several ways in which gold-based NPs can be used for cancer therapy. Moving forward, it is critical to address several key challenges that arise with the use of gold NPs and explore unique opportunities that are afforded by these NPs. Below, we discuss how this research advances several challenges and opportunities of gold NPs for cancer therapy.

6.2 Opportunities and Challenges for Gold Nanoparticles for Cancer Therapy

There are several challenges and opportunities that should be addressed as NSs, and other gold-based NPs, continue to develop as tools for cancer management and as they advance into clinical translation. One challenge that limits the success of phototherapies mediated through gold NSs, such as PTT, is that it is difficult to ensure complete ablation of all tumor cells, and PTT is not feasible as a treatment for metastatic disease. Further, most studies have used high laser powers that cause necrotic cell death that leads to inflammation and higher metastatic rates. Lastly, laser exposure will not be the same throughout the entirety of the tumor depending on NS accumulation, tumor size, and tumor location. However, there are increasing opportunities to use phototherapies in combination with other phototherapies, such as PTT and PDT as shown in Chapter 3, to overcome the limitations of individual strategies. Additionally, interesting opportunities to exploit the unique optical properties of gold NPs enable their use in combination with secondary therapies such as chemotherapy,³⁴ immunotherapy, and gene regulation, the latter of which is investigated in Chapter 4.

In addition to their use as photothermal transducers, another major opportunity for gold NPs is their ability to act as delivery systems for targeting and gene regulatory agents, as evaluated in Chapters 4 and 5. As discussed earlier, the clinical use of these agents are challenged by instability, successful intracellular delivery, and substantial adverse side effects, all of which are improved using NPs as carriers. However, there are several key challenges to the clinical translatability of functionalized NPs. First, actively targeted NPs changes the the pharmacokinetics of the targeting agents and any additional agents loaded onto the NPs.³⁷ This requires researchers to thoroughly characterize and evaluate the biodistribution, release kinetics, and therapeutic efficacy

of every NP formulation in addition to only the free therapeutic entity.⁴¹ Second, solid tumors contain a very heterogeneous population of cells that express a wide variety of cell surface receptors that each influence tumor growth. Thus, the anticancer effects of NPs that target one surface receptor or signaling pathway is limited by molecular heterogeneity. Gold NPs present great opportunities to combat this challenge because they can be surface-coated with several therapeutic moieties within a single platform. In this approach, gold NPs can inhibit several signaling pathways simultaneously for a more comprehensive strategy to inhibit oncogenic signaling.

A final consideration for the clinical impact of gold NPs coated with therapeutic agents is that the cost of production is often higher than non-targeted NPs or free ligands due to losses during NP synthesis and purification.³⁷ However, this issue is counterbalanced by the fact that NPs loaded with targeting agents typically require lower treatment doses than their unconjugated constituents, as investigated in Chapters 4 and 5. This enhancement in efficacy can ultimately save costs for both pharmaceutical companies and patients while decreasing any treatment-related adverse effects.

6.3 Concluding Remarks

There are three common themes presented in this work. The first theme arises from Chapters 3 and 4, which each use NSs for two distinct types of phototherapies for heat generated cell death or to for on-demand gene regulation. This shows that NSs can be used under several irradiation modalities depending on the desired output. Second, our results presented in Chapters 4 and 5 show that using NSs to deliver siRNA or antibodies, respectively, is more effective for inhibiting oncogenic cell signaling than the free molecules. We anticipate that this effect would enable the use

of lower treatment dosages administered to patients. Finally, Chapter 5 presents NSs as translatable tools for metastatic cancer, as NSs were able to accumulate within small tumors in the lungs to inhibit tumor growth. All together, we have shown that NSs are comprehensive and adaptable platforms for both phototherapy and gene regulation applications, and thus they are promising tools to advance cancer therapy.

REFERENCES

- (1) Hanahan, D.; Weinberg, R. a. Hallmarks of Cancer: The next Generation. *Cell* **2011**, *144* (5), 646–674.
- (2) Hadjihannas, M. V; Brückner, M.; Jerchow, B.; Birchmeier, W.; Dietmaier, W.; Behrens, J. Aberrant Wnt/beta-Catenin Signaling Can Induce Chromosomal Instability in Colon Cancer. *Proc. Natl. Acad. Sci. U. S. A.* **2006**, *103* (28), 10747–10752.
- (3) Zhan, T.; Rindtorff, N.; Boutros, M. Wnt Signaling in Cancer. *Oncogene* **2017**, *36* (11), 1461–1473.
- (4) Arnold, K. M.; Pohlig, R. T.; Sims-Mourtada, J. Co-Activation of Hedgehog and Wnt Signaling Pathways Is Associated with Poor Outcomes in Triple Negative Breast Cancer. *Oncol. Lett.* **2017**, *14* (5), 5285–5292.
- (5) Elmore, S. Apoptosis: A Review of Programmed Cell Death. *Toxicol. Pathol.* **2007**, *35* (4), 495–516.
- (6) Fernald, K.; Kurokawa, M. Evading Apoptosis in Cancer. *Trends Cell Biol* **2013**, *23* (12), 620–633.
- (7) Feitelson, M. A.; Arzumanyan, A.; Kulathinal, R. J.; Blain, S. W.; Holcombe, R. F.; Mahajna, J.; Marino, M.; Martinez-Chantar, M. L.; Nawroth, R.; Sanchez-Garcia, I.; et al. Sustained Proliferation in Cancer: Mechanisms and Novel Therapeutic Targets. *Semin. Cancer Biol.* **2015**, *35*, S25–S54.
- (8) Talmadge, J.; Fidler, I. AACR Centennial Series: The Biology of Cancer Metastasis: Historical Perspective. *Cancer Res.* **2010**, *70* (14), 5649–5669.
- (9) Giancotti, F. G. Deregulation of Cell Signaling in Cancer. *FEBS Lett.* **2014**, *588* (16), 2558–2570.
- (10) Dey, N.; Barwick, B. G.; Moreno, C. S.; Ordanic-Kodani, M.; Chen, Z.; Oprea-Ilies, G.; Tang, W.; Catzavelos, C.; Kerstann, K. F.; Sledge, G. W.; et al. Wnt Signaling in Triple Negative Breast Cancer Is Associated with Metastasis. *BMC Cancer* **2013**, *13* (1), 537.

- (11) Hortobagyi, G. N. The Curability of Breast Cancer: Present and Future. *Eur. J. Cancer, Suppl.* **2003**, *1* (1), 24–34.
- (12) Tringale, K. R.; Pang, J.; Nguyen, Q. T. Image-Guided Surgery in Cancer: A Strategy to Reduce Incidence of Positive Surgical Margins. *Wiley Interdiscip. Rev. Syst. Biol. Med.* **2018**, No. October 2017, 1–18.
- (13) Rashid, O. M.; Takabe, K. Does Removal of the Primary Tumor in Metastatic Breast Cancer Improve Survival? *J. Women's Heal.* **2014**, *23* (2), 184–188.
- (14) Cady, B.; Nathan, N. R.; Michaelson, J. S.; Golshan, M.; Smith, B. L. Matched Pair Analyses of Stage IV Breast Cancer with or without Resection of Primary Breast Site. *Ann. Surg. Oncol.* **2008**, *15* (12), 3384–3395.
- (15) Ismael, G. F. V.; Rosa, D. D.; Mano, M. S.; Awada, A. Novel Cytotoxic Drugs: Old Challenges, New Solutions. *Cancer Treat. Rev.* **2008**, *34* (1), 81–91.
- (16) Shapiro, G. I.; Harper, J. W. Anticancer Drug Targets: Cell Cycle and Checkpoint Control. *J. Clin. Invest.* **1999**, *104* (12), 1645–1653.
- (17) Lameire, N. Nephrotoxicity of Recent Anti-Cancer Agents. *Clin. Kidney J.* **2014**, *7* (1), 11–22.
- (18) Suter, T. M.; Ewer, M. S. Cancer Drugs and the Heart: Importance and Management. *Eur. Heart J.* **2013**, *34* (15), 1102–1111.
- (19) Baskar, R.; Dai, J.; Wenlong, N.; Yeo, R.; Yeoh, K.-W. Biological Response of Cancer Cells to Radiation Treatment. *Front. Mol. Biosci.* **2014**, *1* (November), 1–9.
- (20) Blyth, B. J.; Cole, A. J.; MacManus, M. P.; Martin, O. A. Radiation Therapy-Induced Metastasis: Radiobiology and Clinical Implications. *Clin. Exp. Metastasis* **2017**, *0* (0), 1–14.
- (21) Brown, C. Targeted Therapy: An Elusive Cancer Target. *Nature* **2016**, *537* (7620), S106–S108.
- (22) Crafton, S. M.; Salani, R. Beyond Chemotherapy: An Overview and Review of Targeted Therapy in Cervical Cancer. *Clin. Ther.* **2016**, *38* (3), 449–458.
- (23) Widakowich, C.; de Castro, G.; de Azambuja, E.; Dinh, P.; Awada, A. Review: Side Effects of Approved Molecular Targeted Therapies in Solid Cancers. *Oncologist* **2007**, *12* (12), 1443–1455.
- (24) Scott, A. M.; Allison, J. P.; Wolchok, J. D. Monoclonal Antibodies in Cancer

- Therapy. *Cancer Immun.* **2012**, *12* (14), 1–8.
- (25) Mahamodhossen, Y. A.; Liu, W.; Rong-Rong, Z. Triple-Negative Breast Cancer: New Perspectives for Novel Therapies. *Med. Oncol.* **2013**, *30* (3), 653.
- (26) Liedtke, C.; Mazouni, C.; Hess, K. R.; André, F.; Tordai, A.; Mejia, J. A.; Symmans, W. F.; Gonzalez-Angulo, A. M.; Hennessy, B.; Green, M.; et al. Response to Neoadjuvant Therapy and Long-Term Survival in Patients with Triple-Negative Breast Cancer. *J. Clin. Oncol.* **2008**, *26* (8), 1275–1281.
- (27) O, B.; W, W.; L, X.; Henk, H. J. Retrospective Study of Patients with Metastatic Triple-Negative Breast Cancer: Survival, Health Care Utilization, and Cost. *Community Oncol.* **2012**, *9* (1), 8–14.
- (28) Pogoda, K.; Niwińska, A.; Murawska, M.; Pieńkowski, T. Analysis of Pattern, Time and Risk Factors Influencing Recurrence in Triple-Negative Breast Cancer Patients. *Med. Oncol.* **2013**, *30* (1).
- (29) Griffiths, C. L.; Olin, J. L. Triple Negative Breast Cancer: A Brief Review of Its Characteristics and Treatment Options. *J. Pharm. Pract.* **2012**, *25* (3), 319–323.
- (30) Yang, L.; Wu, X.; Wang, Y.; Zhang, K.; Wu, J.; Yuan, Y.-C.; Deng, X.; Chen, L.; Kim, C. C. H.; Lau, S.; et al. FZD7 Has a Critical Role in Cell Proliferation in Triple Negative Breast Cancer. *Oncogene* **2011**, *30* (43), 4437–4446.
- (31) A Study of Vantictumab (OMP-18R5) in Combination With Nab-Paclitaxel and Gemcitabine in Previously Untreated Stage IV Pancreatic Cancer <https://clinicaltrials.gov/ct2/show/NCT02005315?term=NCT02005315&rank=1> (accessed Mar 24, 2017).
- (32) Jimeno, A.; Gordon, M.; Chugh, R.; Messersmith, W.; Mendelson, D.; Dupont, J.; Stagg, R.; Kapoun, A. M.; Xu, L.; Uttamsingh, S.; et al. A First-in-Human Phase I Study of the Anticancer Stem Cell Agent Ipafricept (OMP-54F28), a Decoy Receptor for Wnt Ligands, in Patients with Advanced Solid Tumors. *Clin. Cancer Res.* **2017**, *23* (24), 7490–7497.
- (33) Gurney, A.; Axelrod, F.; Bond, C. J.; Cain, J.; Chartier, C.; Donigan, L.; Fischer, M.; Chaudhari, A.; Ji, M.; Kapoun, A. M.; et al. Wnt Pathway Inhibition via the Targeting of Frizzled Receptors Results in Decreased Growth and Tumorigenicity of Human Tumors. *Proc. Natl. Acad. Sci. U. S. A.* **2012**, *109* (29), 11717–11722.
- (34) Riley, R. S.; Day, E. S. Gold Nanoparticle-Mediated Photothermal Therapy:

Applications and Opportunities for Multimodal Cancer Treatment. *Wiley Interdiscip. Rev. Nanomedicine Nanobiotechnology* **2017**, *9* (4).

- (35) Matsumura, Y.; Maeda, H. A New Concept for Macromolecular Therapeutics in Cancer Chemotherapy: Mechanism of Tumor-tropic Accumulation of Proteins and the Antitumor Agent Smancs. **1986**, *46* (December), 6387–6392.
- (36) Maeda, H. The Enhanced Permeability and Retention (EPR) Effect in Tumor Vasculature: The Key Role of Tumor-Selective Macromolecular Drug Targeting. *Adv. Enzyme Regul.* **2001**, *41* (1), 189–207.
- (37) Valcourt, D. M.; Harris, J.; Riley, R. S.; Dang, M.; Wang, J.; Day, E. S. Advances in Targeted Nanotherapeutics : From Bioconjugation to Biomimicry. **2018**, *3*, 1–18.
- (38) Adams, S.; Marsh, E.; Elmasri, W.; Halberstadt, S.; VanDecker, S.; Sammel, M.; Bradbury, A.; Daly, M.; Karlan, B.; Rubin, S. A High Response Rate to Liposomal Doxorubicin Is Seen among Women with BRCA Mutations Treated for Recurrent Epithelial Ovarian Cancer. *Gynecol Oncol* **2011**, *123* (3), 486–491.
- (39) Anselmo, A. C.; Mitragotri, S. Nanoparticles in the Clinic. *Bioeng. Transl. Med.* **2016**, *1* (1), 10–29.
- (40) Sharma, A.; Madhunapantula, S. V.; Robertson, G. P. Toxicological Considerations When Creating Nanoparticle Based Drugs and Drug Delivery Systems? *Expert Opin Drug Metab Toxicol* **2012**, *8* (1), 47–69.
- (41) Kennedy, P. J.; Oliveira, C.; Granja, P. L.; Sarmiento, B. Antibodies and Associates: Partners in Targeted Drug Delivery. *Pharmacol. Ther.* **2017**, *177*, 129–145.
- (42) Sanna, V.; Pala, N.; Sechi, M. Targeted Therapy Using Nanotechnology: Focus on Cancer. *Int. J. Nanomedicine* **2014**, *9* (1), 467–483.
- (43) Kennedy, L. C.; Bickford, L. R.; Lewinski, N. A.; Coughlin, A. J.; Hu, Y.; Day, E. S.; West, J. L.; Drezek, R. A. A New Era for Cancer Treatment: Gold-Nanoparticle-Mediated Thermal Therapies. *Small* **2011**, *7* (2), 169–183.
- (44) Blaney, S. M. Vascular-Targeted Photothermal Therapy of an Orthotopic Murine Glioma Model. **2011**.
- (45) Inc., N. B. Pilot Study of AuroLase(tm) Therapy in Refractory and/or Recurrent Tumors of the Head and Neck.

<https://clinicaltrials.gov/ct2/show/NCT00848042?term=auroshell&rank=2>
(accessed May 23, 2016).

- (46) Nanospectra Biosciences Inc. Efficacy Study of AuroLase Therapy in Subjects with Primary and/or Metastatic Lung Tumors.
<https://clinicaltrials.gov/ct2/show/NCT01679470?term=auroshell&rank=3>
(accessed May 23, 2016).
- (47) Nanospectra Biosciences Inc. MRI/US Fusion Imaging and Biopsy in Combination With Nanoparticle Directed Focal Therapy for Ablation of Prostate Tissue
<https://clinicaltrials.gov/ct2/show/NCT02680535?term=auroshell&rank=1>
(accessed Sep 28, 2016).
- (48) Stern, J. M.; Solomonov, V. V. K.; Sazykina, E.; Schwartz, J. A.; Gad, S. C.; Goodrich, G. P. Initial Evaluation of the Safety of Nanoshell-Directed Photothermal Therapy in the Treatment of Prostate Disease. *Int. J. Toxicol.* **2015**, *35* (1), 38–46.
- (49) Guo, L.; Yan, D.; Yang, D.; Li, Y.; Wang, X.; Zalewski, O. Combinatorial Photothermal and Immuno Cancer Therapy Using Chitosan-Coated Hollow Copper Sulfide Nanoparticles. *ACS Nano* **2015**, *8* (6), 5670–5681.
- (50) Hashida, Y.; Tanaka, H.; Zhou, S.; Kawakami, S.; Yamashita, F.; Murakami, T.; Umeyama, T.; Imahori, H.; Hashida, M. Photothermal Ablation of Tumor Cells Using a Single-Walled Carbon Nanotube-Peptide Composite. *J. Control. Release* **2014**, *173* (1), 58–66.
- (51) Li, M.; Teh, C.; Ang, C. Y.; Tan, S. Y.; Luo, Z.; Qu, Q.; Zhang, Y.; Korzh, V.; Zhao, Y. Near-Infrared Light-Absorptive Stealth Liposomes for Localized Photothermal Ablation of Tumors Combined with Chemotherapy. *Adv. Funct. Mater.* **2015**, *25* (35), 5602–5610.
- (52) Zhao, P.; Zheng, M.; Yue, C.; Luo, Z.; Gong, P.; Gao, G.; Sheng, Z.; Zheng, C.; Cai, L. Improving Drug Accumulation and Photothermal Efficacy in Tumor Depending on Size of ICG Loaded Lipid-Polymer Nanoparticles. *Biomaterials* **2014**, *35* (23), 6037–6046.
- (53) Lu, W.; Zhang, G.; Zhang, R.; Li, L. G. F.; Huang, Q.; Gelovani, J. G.; Li, C. Tumor Site – Specific Silencing of NF- κ B p65 by Targeted Hollow Gold Nanosphere – Mediated Photothermal Transfection. *Cancer Res.* **2010**, *70*, 3177–3189.
- (54) Cole, J. R.; Mirin, N. A.; Knight, M. W.; Goodrich, G. P.; Halas, N. J.

Photothermal Efficiencies of Nanoshells and Nanorods for Clinical Therapeutic Applications. *J. Phys. Chem. C* **2009**, *113* (28), 12090–12094.

- (55) Wang, Y.; Black, K.; Leuhmann, H.; Li, W.; Zhang, Y.; Cai, X.; Wan, D.; Liu, S.-Y.; Li, M.; Kim, P.; et al. A Comparison Study of Gold Nanohexapods, Nanorods, and Nanocages for Photothermal Cancer Treatment. *ACS Nano* **2013**, *7* (3), 2068–2077.
- (56) Abadeer, N. S.; Murphy, C. J. Recent Progress in Cancer Thermal Therapy Using Gold Nanoparticles. *J. Phys. Chem. C* **2016**, *120* (9), 4691–4716.
- (57) Huang, X.; El-Sayed, I. H.; Qian, W.; El-Sayed, M. A. Cancer Cell Imaging and Photothermal Therapy in the near-Infrared Region by Using Gold Nanorods. *J. Am. Chem. Soc.* **2006**, *128* (6), 2115–2120.
- (58) Mackey, M. A.; Ali, M. R. K.; Austin, L. A.; Near, R. D.; El-sayed, M. A. The Most Effective Gold Nanorod Size for Plasmonic Photothermal Therapy: Theory and In Vitro Experiments. *J. Phys. Chem. B* **2014**, *118*, 1319–1326.
- (59) Stone, J.; Jackson, S.; Wright, D. Biological Applications of Gold Nanorods. *Wiley Interdiscip. Rev. Nanomedicine Nanobiotechnology* **2011**, *3* (1), 100–109.
- (60) Goodman, A. M.; Hogan, N. J.; Gottheim, S.; Li, C.; Clare, S. E.; Halas, N. J. Understanding Resonant Light-Triggered DNA Release from Plasmonic Nanoparticles. *ACS Nano* **2017**, *11* (1), 171–179.
- (61) Jain, P. K.; Qian, W.; El-Sayed, M. A. Ultrafast Cooling of Photoexcited Electrons in Gold Nanoparticle-Thiolated DNA Conjugates Involves the Dissociation of the Gold-Thiol Bond. *J. Am. Chem. Soc.* **2006**, *128* (7), 2426–2433.
- (62) Eloy, J. O.; Petrilli, R.; Lopez, R. F. V; Lee, R. J. Stimuli-Responsive Nanoparticles for siRNA Delivery. **2015**, 4131–4144.
- (63) Hannon, G. J. RNA Interference. *Nature* **2002**, *418* (6894), 244–251.
- (64) Kim, H. J.; Kim, A.; Miyata, K.; Kataoka, K. Recent Progress in Development of siRNA Delivery Vehicles for Cancer Therapy. *Adv. Drug Deliv. Rev.* **2016**, *104*, 61–77.
- (65) Crooke, S. T. Progress in Antisense Technology. *Annu. Rev. Med.* **2004**, *55*, 61–95.
- (66) Jensen, S. A.; Day, E. S.; Ko, C. H.; Hurley, L. a; Luciano, J. P.; Kouri, F. M.;

- Merkel, T. J.; Luthi, A. J.; Patel, P. C.; Cutler, J. I.; et al. Spherical Nucleic Acid Nanoparticle Conjugates as an RNAi-Based Therapy for Glioblastoma. *Sci. Transl. Med.* **2013**, *5* (209), 209ra152.
- (67) Zheng, D.; Giljohann, D. a; Chen, D. L.; Massich, M. D.; Wang, X.-Q.; Jordanov, H.; Mirkin, C. a; Paller, A. S. Topical Delivery of siRNA-Based Spherical Nucleic Acid Nanoparticle Conjugates for Gene Regulation. *Proc. Natl. Acad. Sci. U. S. A.* **2012**, *109* (30), 11975–11980.
- (68) Giljohann, D. A.; Seferos, D. S.; Prigodich, A. E.; Patel, P. C.; Mirkin, C. A. Gene Regulation with Polyvalent siRNA - Nanoparticle Conjugates. *JACS Commun.* **2009**, *131*, 2072–2073.
- (69) Kouri, F. M.; Hurley, L. A.; Daniel, W. L.; Day, E. S.; Hua, Y.; Hao, L.; Peng, C. Y.; Merkel, T. J.; Queisser, M. A.; Ritner, C.; et al. MiR-182 Integrates Apoptosis, Growth, and Differentiation Programs in Glioblastoma. *Genes Dev.* **2015**, *29* (7), 732–745.
- (70) Wu, X. A.; Choi, C. H. J.; Zhang, C.; Hao, L.; Mirkin, C. A. Intracellular Fate of Spherical Nucleic Acid Nanoparticle Conjugates. **2014**.
- (71) Rosi, N. L.; Giljohann, D. a; Thaxton, C. S.; Lytton-Jean, A. K. R.; Han, M. S.; Mirkin, C. a. Oligonucleotide-Modified Gold Nanoparticles for Intracellular Gene Regulation. *Science* **2006**, *312* (5776), 1027–1030.
- (72) Choi, C. H. J.; Hao, L.; Narayan, S. P.; Auyeung, E.; Mirkin, C. a. Mechanism for the Endocytosis of Spherical Nucleic Acid Nanoparticle Conjugates. *Proc. Natl. Acad. Sci. U. S. A.* **2013**, *110* (19), 7625–7630.
- (73) Braun, G. B.; Pallaoro, A.; Wu, G.; Missirlis, D.; Zasadzinski, J. a; Tirrell, M.; Reich, N. O. Laser-Activated Gene Silencing via Gold Nanoshell-siRNA Conjugates. *ACS Nano* **2009**, *3* (7), 2007–2015.
- (74) Yuan, H.; Fales, A. M.; Vo-Dinh, T. TAT Peptide-Functionalized Gold Nanostars: Enhanced Intracellular Delivery and Efficient NIR Photothermal Therapy Using Ultralow Irradiance. *J. Am. Chem. Soc.* **2012**, *134* (28), 11358–11361.
- (75) Scott, A. M.; Wolchok, J. D.; Old, L. J. Antibody Therapy of Cancer. *Nat Rev Cancer* **2012**, *12* (4), 278–287.
- (76) Samaranayake, H.; Wirth, T.; Schenkwein, D.; Raty, J. K.; Yla-Herttuala, S. Challenges in Monoclonal Antibody-Based Therapies. *Ann. Med.* **2009**, *41* (5), 322–331.

- (77) Neyt, M. Cost Considerations for Monoclonal Antibody-Targeted Therapy in Cancer: Focus on Trastuzumab. *Am. J. Cancer* **2006**, 5 (1), 19–16.
- (78) Jiang, W.; Kim, B. Y. S.; Rutka, J. T.; Chan, W. C. W. Nanoparticle-Mediated Cellular Response Is Size-Dependent. *Nat. Nanotechnol.* **2008**, 3, 145–150.
- (79) Xu, S.; Olenyuk, B. Z.; Okamoto, C. T.; Hamm-alvarez, S. F. Targeting Receptor-Mediated Endocytotic Pathways with Nanoparticles : Rationale and Advances ☆. *Adv. Drug Deliv. Rev.* **2013**, 65 (1), 121–138.
- (80) Weissleder, R.; Kelly, K.; Sun, E. Y.; Shtatland, T.; Josephson, L. Cell-Specific Targeting of Nanoparticles by Multivalent Attachment of Small Molecules. *Nat. Biotechnol.* **2005**, 23 (11), 1418–1423.
- (81) Loo, C.; Lowery, A.; Halas, N.; West, J.; Drezek, R. Immunotargeted Nanoshells for Integrated Cancer Imaging and Therapy. *Nano Lett.* **2005**, 5 (4), 709–711.
- (82) Oldenburg, S. .; Averitt, R. .; Westcott, S. .; Halas, N. . Nanoengineering of Optical Resonances. *Chem. Phys. Lett.* **1998**, 288 (2-4), 243–247.
- (83) Gobin, A. M.; Lee, M. H.; Halas, N. J.; James, W. D.; Drezek, R. A.; West, J. L. Near-Infrared Resonant Nanoshells for Combined Optical Imaging and Photothermal Cancer Therapy. *Nano Lett.* **2007**, 7 (7), 1929–1934.
- (84) Riley, R. S.; Day, E. S. Frizzled7 Antibody-Functionalized Nanoshells Enable Multivalent Binding for Wnt Signaling Inhibition in Triple Negative Breast Cancer Cells. *Small* **2017**, 13 (26), 1–10.
- (85) Duff, D. G.; Baiker, A.; Edwards, P. P. A New Hydrosol of Gold Clusters. *ACS Langmuir* **1993**, 272 (16), 2301–2309.
- (86) Day, E. S.; Zhang, L.; Thompson, P. A.; Zawaski, J. A.; Kaffes, C. C.; Gaber, M. W.; Blaney, S. M.; West, J. L. Vascular-Targeted Photothermal Therapy of an Orthotopic Murine Glioma Model. *Nanomedicine (Lond)*. **2012**, 7 (8), 1133–1148.
- (87) Melamed, J. R.; Riley, R. S.; Valcourt, D.; Billingsley, M.; Kreuzberger, N.; Day, E. S. *Quantification of siRNA Duplexes Bound to Gold Nanoparticle Surfaces*, 2nd ed.; Springer, 2016.
- (88) Day, E. S.; Morton, J. G.; West, J. L. Nanoparticles for Thermal Cancer Therapy. *J. Biomech. Eng.* **2009**, 131 (7), 074001.

- (89) Allison, R. R.; Moghissi, K. Oncologic Photodynamic Therapy: Clinical Strategies That Modulate Mechanisms of Action. *Photodiagnosis Photodyn. Ther.* **2013**, *10* (4), 331–341.
- (90) Lucky, S. S.; Soo, K. C.; Zhang, Y. Nanoparticles in Photodynamic Therapy. *Chem. Rev.* **2015**, *115* (4), 1990–2042.
- (91) Agostinis, P.; Berg, K.; Cengel, K. .; Foster, T. .; Girotti, A. .; Gollnick, S. .; Hahn, S. .; Hamblin, M. .; Juzeniene, A.; Kessel, D.; et al. Photodynamic Terapy of Cancer: An Update. *CA Cancer J Clin.* **2011**, *61* (4), 250–281.
- (92) Ozog, D. M.; Rkein, A. M.; Fabi, S. G.; Gold, M. H.; Goldman, M. P.; Lowe, N. J.; Martin, G. M.; Munavalli, G. S. Photodynamic Therapy: A Clinical Consensus Guide. *Dermatologic Surg.* **2016**, *42* (7), 804–827.
- (93) Wang, H.; Xu, Y.; Shi, J.; Gao, X.; Geng, L. Photodynamic Therapy in the Treatment of Basal Cell Carcinoma: A Systematic Review and Meta-Analysis. *Photodermatol. Photoimmunol. Photomed.* **2015**, *31* (1), 44–53.
- (94) Triesscheijn, M.; Baas, P.; Schellens, J. H. M.; Stewart, F. A. Photodynamic Therapy in Oncology. *Oncologist* **2006**, *11* (9), 1034–1044.
- (95) Nowis, D.; Stokłosa, T.; Legat, M.; Issat, T.; Jakóbiśiak, M.; Gołąb, J. The Influence of Photodynamic Therapy on the Immune Response. *Photodiagnosis Photodyn. Ther.* **2005**, *2* (4), 283–298.
- (96) Castano, A. P.; Mroz, P.; Hamblin, M. Photodynamic Therapy and Anti-Tumor Immunity. *Nat. Rev. Cancer* **2006**, *6* (7), 535–545.
- (97) Benov, L. Photodynamic Therapy: Current Status and Future Directions. *Med. Princ. Pract.* **2015**, *24* (suppl 1), 14–28.
- (98) O’Connor, A. E.; Gallagher, W. M.; Byrne, A. T. Porphyrin and Nonporphyrin Photosensitizers in Oncology: Preclinical and Clinical Advances in Photodynamic Therapy. *Photochem. Photobiol.* **2009**, *85* (5), 1053–1074.
- (99) Potocny, A. M.; Pistner, A. J.; Yap, G. P. A.; Rosenthal, J. Electrochemical, Spectroscopic, and $^{1}O_2$ Sensitization Characteristics of Synthetically Accessible Linear Tetrapyrrole Complexes of Palladium and Platinum. *Inorg. Chem.* **2017**, *56* (21), 12703–12711.
- (100) Greenwald, R. B.; Choe, Y. H.; McGuire, J.; Conover, C. D. Effective Drug Delivery by PEGylated Drug Conjugates. *Adv. Drug Deliv. Rev.* **2003**, *55* (2), 217–250.

- (101) Working, P.; Newman, M.; Johnson, J.; Cornacoff, J. Safety of Poly(ethylene Glycol) and Poly(ethylene Glycol) Derivatives. In *Poly(ethylene glycol)*; 1997; pp 45–57.
- (102) Lal, S.; Clare, S. E.; Halas, N. J. Nanoshell-Enabled Photothermal Cancer Therapy: Impending Clinical Impact. *Acc. Chem. Res.* **2008**, *41* (12), 1842–1851.
- (103) Gad, S. C.; Sharp, K. L.; Montgomery, C.; Payne, J. D.; Goodrich, G. P. Evaluation of the Toxicity of Intravenous Delivery of Auroshell Particles (gold-Silica Nanoshells). *Int. J. Toxicol.* **2012**, *31* (6), 584–594.
- (104) Melamed, J. R.; Edelstein, R. S.; Day, E. S. Elucidating the Fundamental Mechanisms of Cell Death Triggered by Photothermal Therapy. *ACS Nano* **2015**, *9* (1), 6–11.
- (105) Pérez-Hernández, M.; Del Pino, P.; Mitchell, S. G.; Moros, M.; Stepien, G.; Pelaz, B.; Parak, W. J.; Gálvez, E. M.; Pardo, J.; De La Fuente, J. M. Dissecting the Molecular Mechanism of Apoptosis during Photothermal Therapy Using Gold Nanoprisms. *ACS Nano* **2015**, *9* (1), 52–61.
- (106) Martin, S. J.; Henry, C. M.; Cullen, S. P. A Perspective on Mammalian Caspases as Positive and Negative Regulators of Inflammation. *Mol. Cell* **2012**, *46* (4), 387–397.
- (107) Dolmans, D.; Fukumura, D.; Jain, R. Photodynamic Therapy for Cancer. *Nat. Rev. Cancer* **2003**, *3* (5), 380–387.
- (108) Oh, J.; Yoon, H.; Park, J. H. Nanoparticle Platforms for Combined Photothermal and Photodynamic Therapy. *Biomed. Eng. Lett.* **2013**, *3* (2), 67–73.
- (109) Wang, L.; Meng, D.; Hao, Y.; Zhao, Y.; Li, D.; Zhang, B.; Zhang, Y.; Zhang, Z. Gold Nanostars Mediated Combined Photothermal and Photodynamic Therapy and X-Ray Imaging for Cancer Theranostic Applications. *J. Biomater. Appl.* **2015**, *30* (5), 547–557.
- (110) Zhao, Z.; Shi, S.; Huang, Y.; Tang, S.; Chen, X. Simultaneous Photodynamic and Photothermal Therapy Using Photosensitizer-Functionalized Pd Nanosheets by Single Continuous Wave Laser. *ACS Appl. Mater. Interfaces* **2014**, *6* (11), 8878–8885.
- (111) Tan, X.; Pang, X.; Lei, M.; Ma, M.; Guo, F.; Wang, J.; Yu, M.; Tan, F.; Li, N. An Efficient Dual-Loaded Multifunctional Nanocarrier for Combined

Photothermal and Photodynamic Therapy Based on Copper Sulfide and Chlorin e6. *Int. J. Pharm.* **2016**, *503* (1-2), 220–228.

- (112) Pistner, A. J.; Yap, G. P. A.; Rosenthal, J. A. Tetrapyrrole Macrocyclic Displaying a Multielectron Redox Chemistry and Tunable Absorbance Profile. *J. Phys. Chem. C* **2012**, *116* (32), 16918–16924.
- (113) Pistner, A. J.; Pupillo, R. C.; Yap, G. P. A.; Lutterman, D. A.; Ma, Y. Z.; Rosenthal, J. Electrochemical, Spectroscopic, and $^{1}O_2$ Sensitization Characteristics of 10,10-Dimethylbiladiene Complexes of Zinc and Copper. *J. Phys. Chem. A* **2014**, *118* (45), 10639–10648.
- (114) Gottlieb, H. E.; Kotlyar, V.; Nudelman, A. NMR Chemical Shifts of Common Laboratory Solvents as Trace Impurities. *J. Org. Chem.* **1997**, *62* (21), 7512–7515.
- (115) Filipovich, G.; Tiers, G. V. D. Fluorine N.s.r. Spectroscopy. I. Reliable Shielding Values, σ , by Use of CCl_3F as Solvent and Internal Reference. *J. Phys. Chem.* **1959**, *63* (5), 761–763.
- (116) Nemoto, M.; Kokubun, H.; Koizumi, M. Determination of S^{*}-T Transition Probabilities of Some Xanthene and Thiazine Dyes on the Basis of T-Energy Transfer. II. Results in the Aqueous Solution. *Bull. Chem. Soc. Jpn.* **1969**, *42* (9), 2464–2470.
- (117) Ragàs, X.; Jiménez-Banzo, A.; Sánchez-García, D.; Batllori, X.; Nonell, S. Singlet Oxygen Photosensitisation by the Fluorescent Probe Singlet Oxygen Sensor Green®. *Chem. Commun.* **2009**, No. 20, 2920.
- (118) Mroz, P.; Yaroslavsky, A.; Kharkwal, G. B.; Hamblin, M. R. Cell Death Pathways in Photodynamic Therapy of Cancer. *Cancers (Basel)*. **2011**, *3* (2), 2516–2539.
- (119) Mocan, T.; Matea, C. T.; Cojocaru, I.; Ilie, I.; Tabaran, F. A.; Zaharie, F.; Iancu, C.; Bartos, D.; Mocan, L. Photothermal Treatment of Human Pancreatic Cancer Using PEGylated Multi-Walled Carbon Nanotubes Induces Apoptosis by Triggering Mitochondrial Membrane Depolarization Mechanism. *J. Cancer* **2014**, *5* (8), 679–688.
- (120) Tong, L.; Cheng, J.-X. Gold Nanorod-Mediated Photothermolysis Induces Apoptosis of Macrophages via Damage of Mitochondria. *Nanomedicine* **2009**, *4* (2).
- (121) Bertrand, J. R.; Pottier, M.; Vekris, A.; Opolon, P.; Maksimenko, A.; Malvy, C.

- Comparison of Antisense Oligonucleotides and siRNAs in Cell Culture and in Vivo. *Biochem. Biophys. Res. Commun.* **2002**, 296 (4), 1000–1004.
- (122) Watts, J.; Corey, D. Gene Silencing by siRNAs and Antisense Oligonucleotides in the Laboratory and the Clinic. *J. Pathol.* **2012**, 226 (2), 365–379.
- (123) Wang, T.; Shigdar, S.; Shamaileh, H. Al; Gantier, M. P.; Yin, W.; Xiang, D.; Wang, L.; Zhou, S. F.; Hou, Y.; Wang, P.; et al. Challenges and Opportunities for siRNA-Based Cancer Treatment. *Cancer Lett.* **2017**, 387, 77–83.
- (124) Riley, R. S.; Day, E. S. Frizzled7 Antibody-Functionalized Nanoshells Enable Multivalent Binding for Wnt Signaling Inhibition in Triple Negative Breast Cancer Cells. *Small* **2017**, 13 (26), 1700544.
- (125) Huang, X.; Lai, Y.; Braun, G. B.; Reich, N. O. Modularized Gold Nanocarriers for TAT-Mediated Delivery of siRNA. *Small* **2017**, 13 (8), 1–8.
- (126) Weissleder, R. A Clearer Vision for in Vivo Imaging. *Nat. Biotechnol.* **2001**, 19, 316–317.
- (127) Riley, R. S.; Day, E. S. Gold Nanoparticle-Mediated Photothermal Therapy: Applications and Opportunities for Multimodal Cancer Treatment. *Wiley Interdiscip. Rev. Nanomedicine Nanobiotechnology* **2017**, 9 (4).
- (128) Krpetić, Ž.; Nativo, P.; Sée, V.; Prior, I. A.; Brust, M.; Volk, M. Inflicting Controlled Nonthermal Damage to Subcellular Structures by Laser-Activated Gold Nanoparticles. *Nano Lett.* **2010**, 10 (11), 4549–4554.
- (129) Kim, J.; Kim, J.; Jeong, C.; Kim, W. J. Synergistic Nanomedicine by Combined Gene and Photothermal Therapy. *Adv. Drug Deliv. Rev.* **2016**, 98, 99–112.
- (130) Huschka, R.; Barhoumi, A.; Liu, Q.; Roth, J. a; Ji, L.; Halas, N. J. Gene Silencing by Gold Nanoshell-Mediated Delivery and Laser-Triggered Release of Antisense Oligonucleotide and siRNA. *ACS Nano* **2012**, 6 (9), 7681–7691.
- (131) Jones, M. R.; Millstone, J. E.; Giljohann, D. a; Seferos, D. S.; Young, K. L.; Mirkin, C. a. Plasmonically Controlled Nucleic Acid Dehybridization with Gold Nanoprisms. *Chemphyschem* **2009**, 10 (9-10), 1461–1465.
- (132) Wijaya, A.; Schaffer, S. B.; Pallares, I. G.; Hamad-Schifferli, K. Selective Release of Multiple DNA Oligonucleotides from Gold Nanorods. *ACS Nano* **2009**, 3 (1), 80–86.
- (133) Huschka, R.; Zuloaga, J.; Knight, M. W.; Brown, L. V; Nordlander, P.; Halas,

- N. J. Light-Induced Release of DNA from Gold Nanoparticles: Nanoshells and Nanorods. *J. Am. Chem. Soc.* **2011**, *133* (31), 12247–12255.
- (134) Barhoumi, A.; Huschka, R.; Bardhan, R.; Knight, M. W.; Halas, N. J. Light-Induced Release of DNA from Plasmon-Resonant Nanoparticles : Towards Light-Controlled Gene Therapy. *Chem. Phys. Lett.* **2009**, *482* (4-6), 171–179.
- (135) Day, E. S.; Thompson, P. A.; Zhang, L.; Lewinski, N. A.; Ahmed, N.; Drezek, R. A.; Blaney, S. M.; West, J. L. Nanoshell-Mediated Photothermal Therapy Improves Survival in a Murine Glioma Model. *J. Neurooncol.* **2011**, *104* (1), 55–63.
- (136) Meister, G.; Tuschli, T. Mechanisms of Gene Silencing by Double-Stranded RNA. *Nature* **2004**, *431*, 343–349.
- (137) Hildebrandt, B.; Wust, P.; Ahlers, O.; Dieing, A.; Sreenivasa, G.; Kerner, T.; Felix, R.; Riess, H. The Cellular and Molecular Basis of Hyperthermia. *Crit. Rev. Oncol. Hematol.* **2002**, *43* (1), 33–56.
- (138) Lee, S. E.; Liu, G. L.; Kim, F.; Lee, L. P. Remote Optical Switch for Localized and Selective Control of Gene Interference. *Nano Lett.* **2009**, *9*, 562–570.
- (139) Poon, L.; Zandberg, W.; Hsiao, D.; Erno, Z.; Sen, D.; Gates, B. D.; Branda, N. R. Photothermal Release of Single-Stranded DNA from the Surface of Gold Nanoparticles Through Controlled Denaturing and Au-S Bond Breaking. *ACS Nano* **2010**, *4* (11), 6395–6403.
- (140) Takahashi, H.; Niidome, Y.; Yamada, S. Controlled Release of Plasmid DNA from Gold Nanorods Induced by Pulsed near-Infrared Light. *ChemComm* **2005**, 2247–2249.
- (141) Sliwkowski, M. X.; Mellman, I. Antibody Therapeutics in Cancer. *Science* **2013**, *341* (6151), 1192–1198.
- (142) Willems, A.; Gauger, K.; Henrichs, C.; Harbeck, N. Antibody Therapy for Breast Cancer. *Anticancer Res.* **2005**, *25* (3 A), 1483–1489.
- (143) Pohl, S.-G.; Brook, N.; Agostino, M.; Arfuso, F.; Kumar, A. P.; Dharmarajan, A. Wnt Signaling in Triple-Negative Breast Cancer. *Oncogenesis* **2017**, *6* (4), e310.
- (144) Clevers, H.; Nusse, R. Wnt/ β -Catenin Signaling and Disease. *Cell* **2012**, *149* (6), 1192–1205.

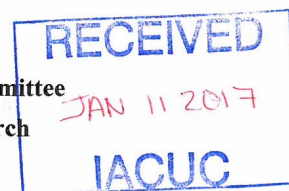
- (145) King, T. D.; Suto, M. J.; Li, Y. The Wnt/ β -Catenin Signaling Pathway: A Potential Therapeutic Target in the Treatment of Triple Negative Breast Cancer. *J. Cell. Biochem.* **2012**, *113* (1), 13–18.
- (146) Angers, S.; Moon, R. T. Proximal Events in Wnt Signal Transduction. *Nat. Rev. Mol. Cell Biol.* **2009**, *10* (7), 468–477.
- (147) Anastas, J. N.; Moon, R. T. WNT Signalling Pathways as Therapeutic Targets in Cancer. *Nat. Rev. Cancer* **2013**, *13* (1), 11–26.
- (148) Reya, T.; Clevers, H. Wnt Signalling in Stem Cells and Cancer. *Nature* **2005**, *434*, 843–850.
- (149) Lustig, B.; Jerchow, B.; Sachs, M.; Weiler, S.; Pietsch, T.; Karsten, U.; van De Wetering, M.; Clevers, H.; Schlag, P. M.; Birchmeier, W.; et al. Negative Feedback Loop of Wnt Signaling through Upregulation of conductin/axin2 in Colorectal and Liver Tumors. *Mol. Cell. Biol.* **2002**, *22* (4), 1184–1193.
- (150) Jho, E.; Zhang, T.; Domon, C.; Joo, C.-K.; Freund, J.-N.; Costantini, F. Wnt/beta-catenin/Tcf Signaling Induces the Transcription of Axin2, a Negative Regulator of the Signaling Pathway. *Mol. Cell. Biol.* **2002**, *22* (4), 1172–1183.
- (151) Wu, Z.-Q.; Brabletz, T.; Fearon, E.; Willis, A. L.; Hu, C. Y.; Li, X.-Y.; Weiss, S. J. Canonical Wnt Suppressor, Axin2, Promotes Colon Carcinoma Oncogenic Activity. *Proc. Natl. Acad. Sci. U. S. A.* **2012**, *109* (28), 11312–11317.
- (152) Segditsas, S.; Tomlinson, I. Colorectal Cancer and Genetic Alterations in the Wnt Pathway. *Oncogene* **2006**, *25* (57), 7531–7537.
- (153) King, T. D.; Zhang, W.; Suto, M. J.; Li, Y. Frizzled7 as an Emerging Target for Cancer Therapy. *Cell. Signal.* **2012**, *24* (4), 846–851.
- (154) Pode-Shakked, N.; Harari-Steinberg, O.; Haberman-Ziv, Y.; Rom-Gross, E.; Bahar, S.; Omer, D.; Metsuyanin, S.; Buzhor, E.; Jacob-Hirsch, J.; Goldstein, R.; et al. Resistance or Sensitivity of Wilms' Tumor to Anti-FZD7 Antibody Highlights the Wnt Pathway as a Possible Therapeutic Target. *Oncogene* **2011**, *30*, 1664–1680.
- (155) Prabhakar, U.; Maeda, H.; K. Jain, R.; Sevick-Muraca, E. M.; Zamboni, W.; Farokhzad, O. C.; Barry, S. T.; Gabizon, A.; Grodzinski, P.; Blakey, D. C. Challenges and Key Considerations of the Enhanced Permeability and Retention Effect for Nanomedicine Drug Delivery in Oncology. *Cancer Res.* **2013**, *73* (8), 2412–2417.

- (156) Brannon-Peppas, L.; Blanchette, J. O. Nanoparticle and Targeted Systems for Cancer Therapy. *Adv. Drug Deliv. Rev.* **2012**, *64* (SUPPL.), 206–212.
- (157) Byrne, J. D.; Betancourt, T.; Brannon-Peppas, L. Active Targeting Schemes for Nanoparticle Systems in Cancer Therapeutics. *Adv. Drug Deliv. Rev.* **2008**, *60* (15), 1615–1626.
- (158) Allen, T. M. Ligand-Targeted Therapeutics in Anticancer Therapy. *Nat. Rev. Cancer* **2002**, *2* (10), 750–763.
- (159) De Puig, H.; Bosch, I.; Carre, M.; Hamad-schi, K. Effect of the Protein Corona on Antibody – Antigen Binding in Nanoparticle Sandwich Immunoassays. *Bioconjug. Chem.* **2017**, *28*, 230–238.
- (160) Oldenburg, S. J.; Averitt, R. D.; Westcott, S. L.; Halas, N. J. Nanoengineering of Optical Resonances. *Chem. Phys. Lett.* **1998**, *288*, 243–247.
- (161) Bickford, L.; Sun, J.; Fu, K.; Lewinski, N.; Nammalvar, V.; Chang, J.; Drezek, R. Enhanced Multi-Spectral Imaging of Live Breast Cancer Cells Using Immunotargeted Gold Nanoshells and Two-Photon Excitation Microscopy. *Nanotechnology* **2008**, *19* (31), 315102.
- (162) Rauch, J.; Kolch, W.; Laurent, S.; Mahmoudi, M. Big Signals from Small Particles: Regulation of Cell Signaling Pathways by Nanoparticles. *Chem. Rev.* **2013**, *113* (5), 3391–3406.
- (163) Marano, F.; Hussain, S.; Rodrigues-Lima, F.; Baeza-Squiban, A.; Boland, S. Nanoparticles: Molecular Targets and Cell Signalling. *Arch. Toxicol.* **2011**, *85* (7), 733–741.
- (164) Maubant, S.; Tesson, B.; Maire, V.; Ye, M.; Rigai, G.; Gentien, D.; Cruzalegui, F.; Tucker, G. C.; Roman-Roman, S.; Dubois, T. Transcriptome Analysis of wnt3a-Treated Triple-Negative Breast Cancer Cells. *PLoS One* **2015**, *10* (4), 1–26.
- (165) Pannerec-Varna, M.; Ratajczak, P.; Bousquet, G.; Ferreira, I.; Leboeuf, C.; Boisgard, R.; Gapihan, G.; Verine, J.; Palpant, B.; Bossy, E.; et al. In Vivo Uptake and Cellular Distribution of Gold Nanoshells in a Preclinical Model of Xenografted Human Renal Cancer. *Gold Bull.* **2013**, *46* (4), 257–265.
- (166) Carpin, L. B.; Bickford, L. R.; Agollah, G.; Yu, T.-K.; Schiff, R.; Li, Y.; Drezek, R. A. Immunoconjugated Gold Nanoshell-Mediated Photothermal Ablation of Trastuzumab-Resistant Breast Cancer Cells. *Breast Cancer Res. Treat.* **2011**, *125* (1), 27–34.

- (167) Lowery, A. R.; Gobin, A. M.; Day, E. S.; Halas, N. J.; West, J. L. Immunonanoshells for Targeted Photothermal Ablation of Tumor Cells. *Int. J. Nanomedicine* **2006**, *1* (2), 149–154.
- (168) Guo, P.; You, J.; Yang, J.; Jia, D.; Moses, M. A.; Auguste, D. T. Inhibiting Metastatic Breast Cancer Cell Migration via the Synergy of Targeted, pH-Triggered siRNA Delivery and Chemokine Axis Blockade. *Mol. Pharm.* **2014**, *11*, 755–765.
- (169) Lee, H.; Dam, D.; Ha, J.; Yue, J.; Odom, T. Enhanced Human Epidermal Growth Factor Receptor 2 Degradation in Breast Cancer Cells by Lysosome-Targeting. *ACS Nano* **2015**, *9* (10), 9859–9867.
- (170) Kim, S. K.; Huang, L. Nanoparticle Delivery of a Peptide Targeting EGFR Signaling. *J. Control. Release* **2012**, *157*, 279–286.
- (171) Ahmad, I.; Allen, T. M. Antibody-Mediated Specific Binding and Cytotoxicity of Liposome-Entrapped Doxorubicin to Lung Cancer Cells in Vitro. *Cancer Res.* **1992**, *52*, 4817–4820.
- (172) Park, J. W.; Hong, K.; Kirpotin, D. B.; Colbern, G.; Shalaby, R.; Baselga, J.; Shao, Y.; Nielsen, U. B.; Marks, J. D.; Moore, D.; et al. Anti-HER2 Immunoliposomes: Enhanced Anticancer Efficacy due to Targeted Delivery. *Clin. Cancer. Res.* **2002**, *8*, 1172–1181.
- (173) Dreaden, E. C.; Mwakwari, S. C.; Sodji, Q. H.; Oyelere, A. K.; El-sayed, M. A. Tamoxifen-Poly(ethylene Glycol)-Thiol Gold Nanoparticle Conjugates: Enhanced Potency and Selective Delivery for Breast Cancer Treatment. *Bioconjug. Chem.* **2009**, *20*, 2247–2253.
- (174) Karra, N.; Benita, S. The Ligand Nanoparticle Conjugation Approach for Targeted Cancer Therapy. *Curr. Drug Metab.* **2012**, *13* (1), 22–41.
- (175) Carter, P. J. Potent Antibody Therapeutics by Design. *Nat. Rev. Immunol.* **2006**, *6* (5), 343–357.

Appendix A
INSTITUTIONAL ANIMAL CARE AND USE
COMMITTEE (IACUC) APPROVAL

University of Delaware
 Institutional Animal Care and Use Committee
 Application to Use Animals in Research
 (New and 3-Yr submission)



Title of Protocol: Biodistribution of Functionalized Silica/Gold Nanoshells in Mice	
AUP Number: 1318-2017-0	← (4 digits only — if new, leave blank)
Principal Investigator: Dr. Emily S. Day	
Common Name (Strain/Breed if Appropriate): nu/nu mice	
Genus Species: Mouse	
Date of Submission: January 6, 2017	

Official Use Only
IACUC Approval Signature: <u>James Talbot, DVM</u>
Date of Approval: <u>3/16/2017</u>

Appendix B

PERMISSIONS TO USE SELF-AUTHORED PAPERS

**SPRINGER NATURE LICENSE
TERMS AND CONDITIONS**

May 21, 2018

This Agreement between University of Delaware -- Rachel Riley ("You") and Springer Nature ("Springer Nature") consists of your license details and the terms and conditions provided by Springer Nature and Copyright Clearance Center.

License Number	4353771481822
License date	May 21, 2018
Licensed Content Publisher	Springer Nature
Licensed Content Publication	Nano Research
Licensed Content Title	Advances in targeted nanotherapeutics: From bioconjugation to biomimicry
Licensed Content Author	Danielle M. Valcourt, Jenna Harris, Rachel S. Riley et al
Licensed Content Date	Jan 1, 2018
Type of Use	Thesis/Dissertation
Requestor type	academic/university or research institute
Format	print and electronic
Portion	full article/chapter
Will you be translating?	no
Circulation/distribution	<501
Author of this Springer Nature content	yes
Title	NANOSHELL PLATFORMS FOR TARGETED GENE REGULATION AND LIGHT-TRIGGERED CANCER THERAPY
Instructor name	Emily Day
Institution name	University of Delaware
Expected presentation date	Jun 2018
Requestor Location	University of Delaware 5 Innovation Way, Suite 200 NEWARK, DE 19711 United States Attn: Rachel S Riley
Billing Type	Invoice
Billing Address	University of Delaware 5 Innovation Way, Suite 200 Newark, DE 19711 United States Attn: Rachel S Riley
Total	0.00 USD
Terms and Conditions	

Springer Nature Terms and Conditions for RightsLink Permissions

<https://s100.copyright.com/AppDispatchServlet>

1/3



RightsLink®

[Home](#)
[Create Account](#)
[Help](#)


ACS Publications
Most Trusted. Most Cited. Most Read.

Title: Evaluating the Mechanisms of Light-Triggered siRNA Release from Nanoshells for Temporal Control Over Gene Regulation

Author: Rachel S. Riley, Megan N. Dang, Margaret M. Billingsley, et al

Publication: Nano Letters

Publisher: American Chemical Society

Date: Jun 1, 2018

Copyright © 2018, American Chemical Society

LOGIN

If you're a **copyright.com** user, you can login to RightsLink using your copyright.com credentials. Already a **RightsLink** user or want to [learn more?](#)

Quick Price Estimate

Permission for this particular request is granted for print and electronic formats, and translations, at no charge. Figures and tables may be modified. Appropriate credit should be given. Please print this page for your records and provide a copy to your publisher. Requests for up to 4 figures require only this record. Five or more figures will generate a printout of additional terms and conditions. Appropriate credit should read: "Reprinted with permission from {COMPLETE REFERENCE CITATION}. Copyright {YEAR} American Chemical Society." Insert appropriate information in place of the capitalized words.

I would like to... [?](#)

Requestor Type [?](#)

Portion [?](#)

Format [?](#)

Select your currency

Quick Price

Click Quick Price

This service provides permission for reuse only. If you do not have a copy of the article you are using, you may copy and paste the content and reuse according to the terms of your agreement. Please be advised that obtaining the content you license is a separate transaction not involving Rightslink.

To request permission for a type of use not listed, please contact [the publisher](#) directly.

Copyright © 2018 [Copyright Clearance Center, Inc.](#) All Rights Reserved. [Privacy statement](#). [Terms and Conditions](#). Comments? We would like to hear from you. E-mail us at customercare@copyright.com



RightsLink®

[Home](#)
[Account Info](#)
[Help](#)


Title: Frizzled7 Antibody-Functionalized Nanoshells Enable Multivalent Binding for Wnt Signaling Inhibition in Triple Negative Breast Cancer Cells

Author: Rachel S. Riley, Emily S. Day

Publication: Small

Publisher: John Wiley and Sons

Date: May 22, 2017

Copyright © 2017, John Wiley and Sons

Logged in as:
Rachel Riley
University of Delaware
Account #:
3001029029

[LOGOUT](#)

Order Completed

Thank you for your order.

This Agreement between University of Delaware -- Rachel Riley ("You") and John Wiley and Sons ("John Wiley and Sons") consists of your license details and the terms and conditions provided by John Wiley and Sons and Copyright Clearance Center.

Your confirmation email will contain your order number for future reference.

[printable details](#)

License Number	4384971365749
License date	Jul 09, 2018
Licensed Content Publisher	John Wiley and Sons
Licensed Content Publication	Small
Licensed Content Title	Frizzled7 Antibody-Functionalized Nanoshells Enable Multivalent Binding for Wnt Signaling Inhibition in Triple Negative Breast Cancer Cells
Licensed Content Author	Rachel S. Riley, Emily S. Day
Licensed Content Date	May 22, 2017
Licensed Content Volume	13
Licensed Content Issue	26
Licensed Content Pages	10
Type of use	Dissertation/Thesis
Requestor type	Author of this Wiley article
Format	Print and electronic
Portion	Full article
Will you be translating?	No
Title of your thesis / dissertation	NANOSHELL PLATFORMS FOR TARGETED GENE REGULATION AND LIGHT-TRIGGERED CANCER THERAPY
Expected completion date	Jun 2018
Expected size (number of pages)	1
Requestor Location	University of Delaware 5 Innovation Way, Suite 200 NEWARK, DE 19711 United States Attn: Rachel S Riley